Università degli Studi di Ferrara

DOTTORATO DI RICERCA IN FISICA

CICLO XXXVI

COORDINATRICE
Prof.ssa Eleonora Luppi

Strange Quark Matter in Astrophysics and Cosmology

Settore Scientifico Disciplinare FIS/02

Dottorando
Dott. Di Clemente Francesco

_____

Tutore
Prof. Drago Alessandro

_____

Co-tutore
Prof. Pagliara Giuseppe

_____

Anni 2020/2023

Abstract

The Bodmer-Witten hypothesis suggests that strange quark matter is the true ground state of matter. This hypothesis has significant implications for astrophysics and cosmology. In cosmology, lumps of absolutely stable strange quark matter can constitute dark matter. In astrophysics, it implies the existence of strange stars in coexistence with hadronic stars in the so-called two-families scenario.

First, we propose a way to test this scenario through the observation of the kilonovae produced in mergers between compact stars and black holes. We study the impact of the nuclear matter equation of state on the ejected material in those events, and therefore, on the possible observed kilonova signals. In particular, we predict the statistical suppression of those events in the two-families scenario as compared with the standard scenario.

In a second investigation, we explore the cosmological implications of strangelets as dark matter candidates. This involves assessing the size and mass distribution of strangelets, ensuring their agreement with the existing constraints on macroscopic dark matter.

Therefore, we examine the astrophysical consequences of this cosmological scenario, particularly focusing on how the presence of strangelets might affect the stellar evolution. We focus on two cases: we investigate how strangelets, when captured by white dwarfs, impact the stability of these stars which become strange dwarfs; we suggest that the presence of strangelets in the core of stars which undergoes electron-capture supernova can result in the formation of subsolar mass strange stars, which might have been already observed, as in the case of HESS J1731-347 and SAX J1808.4-3658.

Contents

Acronyms

2SC	Two-flavor Superconductor
AIC	Accretion-Induced Collapse
BCS	Bardeen-Cooper-Schrieffer
BE	Binding Energy
BH	Black Hole
BPS	Baym-Pethick-Sutherland
CCDM	Chiral Chromo-Dielectric Model
CCS	Crystalline Color Superconductor
CDM	Chromo-Dielectric Model
CFL	Color-Flavor-Locked
EM	electromagnetic
EoS	Equation of State
GW	Gravitational Wave
HIC	Heavy-Ion Collisions
HS	Hadronic Star
HyS	Hybrid Star
KN	Kilonova
LOFF	Larkin-Ovchinnikov-Fulde-Ferrell
MR	mass-radius
NFW	Navarro-Frenk-White
NJL	Nambu-Jona-Lasinio
NS	Neutron Star
PTA	Pulsar Timing Array

QCD	Quantum Chromodynamics
QED	Quantum Electrodynamics
QFT	Quantum Field Theory
QGP	Quark-Gluon Plasma
QM	Quark Matter
SD	Strange Dwarf
sGRB	short Gamma-Ray burst
SGWB	Stochastic Gravitational-Wave Background
SN	Supernova
SQM	Strange Quark Matter
SQS	Strange Quark Star
TOV	Tolman-Oppenheimer-Volkoff
WD	White Dwarf
WIMP	Weakly-Interacting Massive Particle

List of Figures

List of Tables

Introduction

A Neutron Star (NS), is the remnant of massive stars after a Supernova (SN) explosion. NSs are among the most extreme objects known to physics. The study of their properties serves in probing the fundamental laws governing extreme dense matter and energy in the universe.

Formed through the gravitational collapse of massive stars, NSs represent the endpoint of stellar evolution. The core collapse process is a culmination of a delicate interplay between the tremendous gravitational forces and the opposing pressures exerted by neutron degeneracy, the strong nuclear force, and the repulsive force of nucleon interactions.

One of the defining features of NSs is their remarkable size-to-mass ratio. With typical masses around 1.4 $M_{\odot}$ and radii on the order of 10-15 km. NSs are incredibly dense, and their core can reach density greater than 10^{15} g/cm^3. The equation of state, which describes the relationship between pressure, density, and energy in such extreme environments, remains a central focus in NS research. Recent advancements in theoretical models and observations have provided crucial constraints on the equation of state, offering insights into the nature of ultra-dense matter. Nevertheless, certain tensions have emerged between data and theoretical predictions, particularly in light of recent observations involving Gravitational Wave (GW)s and precise radius measurements by instruments like *NICER* [4, 26, 3].

General relativistic corrections significantly influence their properties, affecting the observed pulsar signals, space-time curvature, and gravitational redshift. GWs astronomy has emerged as a powerful tool for probing these relativistic effects, providing a window into the behavior of matter under the most extreme conditions.

NSs are also known for their intense magnetic fields. Magnetars, a subset of NSs with incredibly strong magnetic fields ($\sim 10^{15}$ G), have been observed emitting intense bursts of X-rays and gamma-rays [27]. The origin of these magnetic fields remains an active area of research, with potential connections to processes like magnetic field amplification during the star's formation or subsequent evolution.

Advancements in numerical simulations and computational capabilities have allowed to delve into the complexities of NS mergers. Such mergers are the progenitors of Kilonovae (KNe), intense bursts of electromagnetic radiation that accompany the coalescence of two NSs or eventually a NS and a Black Hole (BH). These events are of particular interest due to their potential role in heavy element nucleosynthesis and their connection to the observed short gamma-ray bursts [28, 29, 30].

Nevertheless, this is not all the story. Our understanding of NSs, as mentioned before, is far from being complete. While we can make educated predictions about the composition of these stars up to a certain density, our knowledge becomes less certain at densities greater than that of atomic nuclei. In the central regions of NSs, new particles, including hyperons and delta resonances, can form just because they become energetically favorable.

The presence of these particles affects the NS's properties. They cause the star to be more compressible, leading to potentially smaller sizes and lower maximum masses. However, this idea is in conflict with some observations of NS compactness. As a result, the behavior and composition of NSs at ultra-high densities remain areas of active research and discussion.

From here, the necessity of considering new astrophysical scenario for compact star arises. In this thesis, we will adopt the two-families scenario proposed by Drago et al. [31]. This approach envisions the coexistence of two distinct branches of compact stars: the hadronic star branch and the Strange Quark Star (SQS) branch.

The hadronic star branch comprises NSs which are quite compact, primarily due to a soft equation of state. This softness arises from the emergence of delta resonances and hyperons. On the other hand, the SQS branch includes stars that are less compact (beyond a certain central energy density) but showcase unique behaviors linked from the physics of deconfined Strange Quark Matter (SQM). This type of matter can exhibit exotic features, including color superconductivity.

In this work, we'll explore methods to study the two-families scenario using current advances in multi-messenger astronomy. KNe play an important role in helping us understand the equation of state for nuclear matter. To this end, we've looked at mergers of BHs and NSs. Our goal is to highlight the differences between the two-families scenario and a model where only one type of compact star exists.

Most importantly, the existence of SQSs is intrinsically linked to the Bodmer-Witten hypothesis. These stars are self-bound, and some might have ties to the early universe. Expanding on Witten [32] paper, if SQM indeed represents the true ground state of matter, it might partially or entirely constitute dark matter, as originally proposed by Witten.

Within this thesis, we will further explore the potential astrophysical implications of this cosmological perspective. The presence of SQM nuggets (or strangelets) in the universe can deeply affect the evolutionary path of ordinary star that in principle don't contain strange particles.

We will investigate the stability of white dwarfs that have accumulated a core of SQM over the course of their existence through the accretion of strangelets. Our objective is to provide a deeper understanding of how their evolutionary path may diverge from the conventional one, especially when these white dwarfs, now strange dwarfs, are part of a binary system. The key question we aim to address is whether the acquisition of a sufficient number of strangelets can significantly alter their dynamic stability, ultimately leading to a distinct evolutionary outcome.

Our study brings us to consider the interplay between the presence of strangelets

and some extreme astrophysical phenomena such as some kind of SNe and to explain the possible presence of subsolar mass km-sized objects, namely compact stars with less than one solar mass that currently have no other theories explaining the astrophysical path that could lead to their formation.

Thesis Structure

This thesis is structured in 4 chapters:

- **Chapter 1** reviews the existing literature to trace the historical development of strange quark matter. The objective is to provide the reader with a comprehensive understanding of the origins and theoretical underpinnings of strange quark matter research.
- **Chapter 2** is based on the papers Di Clemente et al. [33] and the forthcoming Mathias et al. [11]. This chapter explores the kilonova signals within the context of the two-families scenario. It aims to elucidate the observational signatures and theoretical interpretations of kilonovae in light of this scenario.
- **Chapter 3** addresses ongoing research into strangelets, with a specific focus on observational constraints and their possible size and mass distributions. It aims to present the current state of study in this field, including a proposed phenomenological model that describes the primordial evaporation of strangelets, considered as a form of dark matter, into hadrons.
- **Chapter 4** is about the findings presented in Di Clemente et al. [34]. This part focuses on the stability of White Dwarfs that possess a core composed of strange quark matter. It delves into the implications of having such a core and on the conditions that could lead to a different evolutionary path with respect to a common White Dwarf.

Chapter 1

Strange matter - history and astrophysics

1.1 Theorizing Strange Quark Matter

In our day-to-day lives, the matter we see is made up of electrons, protons, and neutrons. This is typical because there is no strange quark in regular matter. But in high-energy lab experiments, we create something called hypernuclei, containing the strange quark [35]. These eventually break down into regular particles. When we look at places with extreme pressure and density, like inside compact stars, the situation is different. Here, due to the high energy, strange quarks can form and remain stable.

In 1971 Bodmer [36] discussed for the first time the possibility that ordinary matter is just a metastable state of matter and that for a sufficiently large baryon number A there exists a "collapsed nucleus" which would be more stable and more compact than the normal nucleus. This would be ten times denser than regular matter. If this exists, it could be the true ground state of matter. Bodmer used qualitative arguments to explain why we might only see regular matter, even if this denser form exists, as long as the regular matter is sufficiently long-lived.

Among the models discussed by Bodmer, two of them were considering states composed by ordinary and hyperonic matter having an exceptionally large binding energy. However, the approach to these models was largely qualitative. This makes sense when considering that the MIT bag model would only be introduced three years after Bodmer's discussions.

In 1979, Chin and Kerman [37] looked into the idea of quark-nuclei that could last for a long time. They pointed out the necessity of the presence of s quarks to keep these special nuclei stable enough. Indeed they showed the stability with respect to strong interactions of those *uds* quark-nuclei. On the other hand, in contrast with the hypothesis of the absolutely stable QM, these quark *droplets* were considered metastable and eventually they would have converted in ordinary nuclei via weak leptonic processes.

Then, in 1984, the seminal paper bt Witten [32] on SQM was published. He proposed a cosmological scenario in which stable *uds* quark nuggets (*strangelets*), formed in the early Universe during the hadronization (roughly 10^{-6} s after the Big Bang), would be a component of the dark matter in today's Universe.

The Witten's conjecture states that while two-flavors QM has an higher energy per baryon with respect to iron ($(E/A)_{^{56}\mathrm{Fe}} = 930$ MeV), three-flavor QM has a lower one. For small values of A this statement is false. Indeed, for $A = 1$ (Λ^0 baryon) the mass is $\sim 1115 MeV$ [38, 39]. Therefore, the reason why for heavier nuclei, ordinary hadronic matter does not decay into SQM is because one must transform simultaneously u or d quark into s quark. This process is clearly and A^{th} order weak one and because of this regular nuclei can last a long time (exceeding the age of the Universe) without turning into SQM.

Witten [32] postulates that during the cosmic phase transition, bubbles of low-temperature phase grew within a high-temperature phase. These bubbles could form lumps of hot SQM, potentially stable under zero temperature and pressure. Contrary to traditional views, which hold that nuclei are most stable, Witten suggests that SQM might be energetically favorable, leading to the formation of quark lumps that could survive to the present day. These lumps would be essentially invisible to normal baryonic processes and might be a significant component of dark matter. Indeed, the paper's strength lies in its novel approach to the dark matter problem, providing a plausible explanation based on Quantum Chromodynamics (QCD).

After Witten also Farhi and Jaffe [40] published a paper in which they delved into the properties of SQM using the MIT Bag Model. They showed that there exists a region in the parameter space of the model in which SQM would be the real ground state of matter. They classify their discussions into bulk matter and strangelets (to distinguish SQM with relatively low baryon number).

They use a Fermi-gas model with corrections for surface tension and Coulomb forces to assess the problem of the stability of the strangelet. They consider the energy per baryon E/A and the baryon number A, accounting on how surface effects may cause strangelets to fission or remain stable.

For bulk SQM, the energy per baryon approaches a limit from below due to symmetry energy, driven by the constraint that the charge-to-baryon ratio Z/A tends to zero. Surface effects, both intrinsic and dynamical, play a significant role in the stability. The intrinsic surface tension (σ_I) could be related to the phase boundary separating true vacuum from the perturbative vacuum inside hadrons, while dynamical surface tension (σ_D) arises from corrections to the Fermi gas approximation.

Furthermore, the authors discuss the potential for SQM to be charged (positively or negatively) and the implications of its interaction with ordinary matter.

Notably, Farhi and Jaffe [40] discuss the potential stability of SQM over a wide range of baryon numbers and the associated phenomenological implications. The authors propose that if SQM is stable in bulk, it may be stable down to a certain minimum baryon number A_{min}, which varies based on different model parameters. The authors define a practical lower limit of stability based on the separation energy

required to remove a baryon from a strangelet. Below this limit, strangelets would decay through a series of emissions, driven out of flavor equilibrium until weak interactions reestablish it, a process similar to radioactive decay in heavy nuclei.

For bulk matter, the interaction with ordinary matter and the potential for absorption of nucleons through exothermic reactions is considered. The authors highlight the role of Coulomb barriers in preventing the absorption of nuclei and rendering SQM inert in contact with ordinary matter. They also consider the scenario where bulk SQM has a negative hadronic electric charge, which could have drastic consequences if it comes into contact with ordinary matter.

The authors also discuss potential signatures of SQM, such as its low charge-to-baryon-number ratio, which could manifest as new superheavy elements. The paper concludes with the authors noting the importance of understanding if stable SQM exists or can be created, as it could have implications for energy production and other practical concerns.

The values of the bag constant B are crucial in considering the stability of SQM. Farhi and Jaffe reference values of B obtained from fits to the spectra of light hadrons within the bag model framework (section A.6), which are critical in the examination of SQM's bulk properties.

1.2 Strangeness in heavy ion collisions

Later in the '80s Greiner et al. [41, 42] started considering the possible production of stable SQM in Heavy-Ion Collisions (HIC). The enhancement in strangeness production in HIC was alreadt theorized by Rafelski and Muller [43]. The paper is a foundational work in high-energy nuclear physics. It calculates the rates of strangeness production processes in a highly excited Quark-Gluon Plasma (QGP). The paper finds that for temperatures above approximately 160 MeV, the abundance of strangeness in the plasma saturates within its lifetime, which is relevant for plasmas created in high-energy nuclear collisions.

The study uses the MIT bag model to assume values for the strange quark mass and the effective QCD coupling constant. The paper illustrates that the chemical equilibration time for gluons and light quarks is less than 10^{-23} s, suggesting that the QGP reaches chemical equilibrium rapidly during its lifetime. The numerical results show that strangeness production by gluons is the dominant process and that the strangeness abundance will be chemically saturated at temperatures above 160 MeV. Therefore, enhanced abundances of strange hadrons, such as the Λ particle, can be utilized as indicators for the formation of QGP in nuclear collisions.

In Greiner et al. [41] the strangelets instead were thought to be the transient signature for the existence of the QGP. The authors describe two potential outcomes for the state of matter after a heavy-ion collision. One outcome involves the formation of a strangelet, seen as a metastable droplet of SQM. The other involves the creation of multistrange hadrons during the last stage of the transition. These strangelets, if formed, may serve as evidence for the transient existence of a

quark-gluon plasma.

During the phase coexistence, the quark phase becomes charged with strangeness due to the emission of mesons like kaons, which carry away entropy, and antistrangeness from the system. This leads to an increase in the strangeness abundance in the quark phase. The hadron phase, on the other hand, becomes diluted and absorbs the remaining entropy.

A key point is that as the system cools, the resulting strangelets are hypothesized to have a distinct charge-to-mass ratio, which could provide a unique signature of their existence. The cooling process of the QGP following a heavy-ion collision is crucial to the potential formation of strangelets. As the QGP, an extremely hot and dense state of matter, expands, it begins to cool down and transition into hadronic matter—a state consisting of particles such as protons, neutrons, and mesons.

This cooling is not merely a reduction in temperature due to expansion. It is significantly influenced by thermal evaporation, where particles with sufficient kinetic energy, particularly mesons like pions and kaons, escape from the plasma's surface. These particles carry away not only energy but also entropy and antistrangeness. The emission of kaons is especially critical as it involves strange quarks, leading to an increase in the strangeness within the remaining quark phase.

The process of meson radiation thus serves a dual purpose. It cools the system by removing high-energy particles and alters the composition of the quark phase, enriching it in strangeness. This enrichment is essential as it may lead to the formation of strangelets once the system has cooled sufficiently.

Moreover, the cooling of the QGP also occurs through isentropic expansion, where the plasma expands, its volume increases, and its temperature decreases while maintaining constant entropy. However, the addition of meson radiation introduces a non-isentropic dimension to the cooling, as entropy is actively reduced by the escaping mesons, signifying a move toward a more ordered state.

As the QGP cools and loses entropy, it is hypothesized that the quark phase could become super-saturated with strange quarks, possibly leading to the formation of strangelets. These strangelets, if formed, could be stable or metastable at the lower temperatures achieved after the plasma has cooled. They are of particular interest because their detection would provide a unique signature of the prior existence of the QGP and contribute to our understanding of the strong force and the behavior of matter under extreme conditions.

In a similar fashion, in the second paper [42] they show that in heavy-ion collisions (the initial net strangeness of the QGP is zero) during the phase transition, there can be a significant accumulation of antistrangeness in the hadronic matter and a corresponding enrichment of net strangeness in the quark-gluon plasma. A first-order deconfinement phase transition is assumed, with conditions of Gibbs phase equilibrium dictating that temperature and chemical potentials are continuous across the phase boundary while the corresponding densities are not.

It concludes by emphasizing the potential for the proposed strangeness separation mechanism to lead to a tremendous enrichment of strange quarks in the QGP

during the late stage of the phase transition. This could result in the formation of strangelets, which authors claim to be metastable only for small value of A and stable for $A > 10$. Moreover, the authors study the impact of the bag choice in the original MIT bag model and they found that $B^{1/4} < 160$ MeV, similar to Farhi and Jaffe [40].

1.3 Modelling SQM: confinement models VS chiral models

In the '90s people start talking about confinement [44] and mass dependence on density [45]. Moreover they start to study multi-strange objects in HIC, namely production and possible stability of hyperonic matter and strange clusters [46, 47].

The Witten's hypothesis remains a significant question in nuclear and particle physics, with profound implications in astrophysics and possibly cosmology. In the context of confinement models, such as the MIT bag model [48], there is considerable flexibility in parameter choices that can accommodate the existence of stable SQM. The hypothesis is particularly satisfied when considering smaller values of the strange quark current mass [49].

Chiral models, however, seem to present challenges for the Bodmer-Witten hypothesis. For instance, models like the Nambu-Jona-Lasinio (NJL) model [50], which emphasizes chiral symmetry, appear to not satisfy this hypothesis [51, 52]. A crucial factor in these models is the density dependence of the strange quark mass, which is determined by quark-meson couplings. The hypothesis could be fulfilled if there is a significant interplay between confinement and spontaneous chiral symmetry breaking.

The Chiral Chromo-Dielectric Model (CCDM) [53, 54, 55], which incorporates elements of both chiral models and confinement, is noteworthy. This model is an extension of the Chromo-Dielectric Model (CDM) model, which simulates quark confinement through the action of the color dielectric field, effectively making quark masses diverge in vacuum.

The CDM lagrangian reads [53, 56]:

$$\mathcal{L} = \bar{\psi} i \gamma^{\mu} \partial_{\mu} \psi - \frac{g}{\chi} \bar{\psi} \psi + \frac{1}{2} (\partial_{\mu} \chi)^2 - U(\chi) \tag{1.1}$$

In this formulation, $U(\chi)$ represents a potential with a definite minimum when $\chi = 0$. Some variants of the model also feature a local minimum for $\chi = \chi_v \neq 0$. Crucially, the scalar field χ correlates with quark density, tending towards zero as the chiral condensate $\bar{\psi}\psi$ approaches zero. This results in the quark mass $m_q = g/\chi$ becoming infinite at low quark densities. This divergence in quark mass at lower densities effectively confines quarks within areas of finite density, preventing their spread into regions of zero density. While it successfully models confinement in a manner consistent with a potential between quark pairs that linearly increases with

their separation at greater distances, neither lattice QCD calculations nor analytical studies of QCD in the infrared regime suggest a diverging quark mass. Thus, this behavior within the model should be considered more as a phenomenological approach to describe confinement rather than a direct derivation from QCD principles.

Alberico et al. [57] studied indeed the case in which the potential $U(\chi)$ has a double minimum, checking how different it behaves with respect to the MIT bag model. The study compares the energy per baryon with the masses of hyperons having equivalent strangeness fractions, also incorporating the perturbative exchange of gluons. The MIT bag model and the double minimum version of the CDM support the possibility of strangelets, as these models propose a two-phase picture of hadrons with a false vacuum. They indicate that the minimum energy per baryon number versus the strangeness fraction R_s is lower than the hyperon masses with the same R_s, suggesting the metastability of strangelets with a potential mass gap up to 300 MeV. On the other hand, the single minimum version of the CDM does not support the existence of strangelets, except potentially at $R_s = \frac{2}{3}$, taking into account surface energy contributions. Alberico et al. [57] emphasizes that the stability of strangelets, potentially formed from the quark-gluon plasma phase in relativistic heavy ion collisions, is significantly influenced by the model employed, with the CDM supporting the stability of strangelets only in its double minimum version, thereby posing challenges to their detection as a signature of the QGP phase.

On the other hand CCDM, with its ability to dynamically confine quarks while being chiral invariant, provides a framework where the Bodmer-Witten hypothesis can be realized, blending the features of chiral symmetry and confinement.

The chiral version of the model has been studied in Broniowski et al. [58], Barone et al. [59] and Drago et al. [55]. The lagrangian in this case incorporates more elements and reads:

$$\begin{aligned}\mathcal{L} = & i\bar{\psi}\gamma^{\mu}\partial_{\mu}\psi + \frac{g}{\chi}\bar{\psi}\left(\sigma + i\gamma_5\vec{\tau}\cdot\vec{\pi}\right)\psi \\ & + \frac{1}{2}\left(\partial_{\mu}\chi\right)^2 - U(\chi) + \frac{1}{2}\left(\partial_{\mu}\sigma\right)^2 + \frac{1}{2}\left(\partial_{\mu}\vec{\pi}\right)^2 - U(\sigma,\vec{\pi}).\end{aligned} \tag{1.2}$$

In particular Drago et al. [55] found that the deconfinement phase transition and the restoration of chiral symmetry are observed to occur at substantially different densities. Additionally, QM when the potential has only one minimum version becomes unstable at low densities, in according with Alberico et al. [57]. This instability is evidenced both through the study of compressibility and the analysis of collective states at zero energy transfer, with both methods identifying the same critical density (chiral restoration).

1.4 Color superconductivity in the Equation of State

The idea of color superconductivity in QM comes from the Bardeen-Cooper-Schrieffer (BCS) theory of superconductivity in solid state physics.

When we consider superconductivity in metals, we associate the BCS mechanism with the creation of Cooper pairs of electrons, resulting from an attractive interaction among fermions at a Fermi surface (mediated by quasi-particles named phonons). Analogously, quarks at high densities and relatively low temperatures form Cooper pairs, which condense to create a color superconducting phase. When we delve into QCD we have to consider that the Cooper pairs' formation is even more robust than in metals. This is attributed to the strength of color interaction between quarks, since the attractive interaction is mediated by gluons. The Cooper pairs behave like bosonic particles, settling in the state with the lowest energy. Given that the BCS mechanism is a collective process, and its strength increases with the number of participating fermions, it becomes particularly relevant in compact stars where dense QM can be present.

Formally, we take into account the appearance of color superconductivity by introducing in the lagrangian diquark terms in NJL-like models, namely quark-quark interactions. The diquark interaction lagrangian reads:

$$\mathcal{L}_{qq} = \sum_D G_D(\bar{\psi}\hat{\Gamma}^{(D)}C\bar{\psi}^T)(\psi^T C\hat{\Gamma}^{(D)}\psi) \tag{1.3}$$

where C is the charge conjugation operator defined as $C = i\gamma^2\gamma^0$, D are the various diquark channels, G_D the coupling constant and $\hat{\Gamma}^D$ the diquark operator.

When we study the thermodynamic potential, we transform the interactions into a bilinear form of quark fields using mean-field approximation. Following the ideas of BCS theory, we expect that a color superconductor's ground state would possess a nonzero expectation value, namely a diquark condensate.

When we account for color superconductivity in our models, we have additional contributions in our Equation of State (EoS) that are functions of the color superconductive gap Δ. What has been done for many years is to write phenomenological models which are similar to the MIT bag model but that include parameters to account QCD perturbative corrections.

The form of the most generic phenomenological thermodynamic potential reads [60]:

$$\Omega = -\frac{3}{4\pi^2}a_4\mu^4 + \frac{3}{4\pi^2}a_2\mu^2 + B_{eff}. \tag{1.4}$$

In the simpler version of the equation a_4, a_2 and B_{eff} do not depend on the quark chemical potential μ, usually taken as and averaged chemical potential when, for example, considering Color-Flavor-Locked (CFL) matter (in general B_{eff} is not a constant as in section A.6).

The quartic coefficient $a_4 \equiv 1 - c$ accounts for QCD corrections to the pressure of the free-quark Fermi sea. When $c = 0$, then $a_4 = 1$, it corresponds to consider non interacting free quarks. In general QCD corrections are not negligible and the contribution of a_4 is of the order of 0.3. The quadratic coefficient a_2 appears when accounting for strange quark mass m_s or for color superconductivity. For CFL matter $a_2 = m_s^2 - 4\Delta^2$ from which it is clear the effect of the strange mass in increasing the free energy and the effect of gaps formation in reducing it. This is not the only way to consider an EoS for color superconductive QM. The potential in Eq. 1.4 is inspired to MIT bag model but one can derive the thermodynamic potential also from the Lagrangian of the 3 flavours NJL model as Eq. A.20, adding the diquark condensate term (Eq. 1.3). Even though the calculation is possible, the EoS obtained by doing this will not respect the Bodmer-Witten hypothesis on the absolute stability of SQM [51, 52].

Diquark Condensation Patterns

Since the color superconductivity in strange quark matte descends from a breaking of the $SU(3)$ group, several condensation patterns are possible because of the 8 generators of the group itself. Therefore, different phases of dense QM are characterized by distinct diquark condensation patterns. Below are the condensation patterns for some of the most studied phases:

1. **Two-Flavor Color Superconductor:** The Two-flavor Superconductor (2SC) phase is one of the first color superconductive condensation pattern ever studied. In the 2SC phase, two out of three color charges are involved in the Cooper pairing, leaving one color unpaired, conventionally the blue one. The diquark condensate Δ is defined as:

$$-G_D \langle \psi^T C i\gamma_5 \sigma_2 \lambda_2 \psi \rangle \tag{1.5}$$

   where the Pauli matrices σ_2 and λ_2 specify the up-down flavor pairing and red-green color pairing, respectively.

   In 2SC thermal conductivity can be significantly affected by the presence of the superconductive gap. The unpaired quarks, which do not have a gap, can contribute more effectively to thermal transport, while the paired quarks will have suppressed contributions [61]. Moreover, the 2SC phase can exhibit gapless modes when decreasing the density of the system. For example when in the ds sector the ratio between the squared constituent mass of the strange quark and the chemical potential becomes

$$\frac{M_s^2}{\mu} = 2\Delta_{ds}\,,$$

   where Δ_{ds} is the d and s quarks pairing gap, Cooper pairs start to "unpair" and gapless modes appear [62]. The problem of the gapless phase is that is

magnetically unstable: gluons acquire an imaginary Meissner mass, therefore one has to think about other possible phases at low densities [63, 64].

2. **Crystalline Color Superconducting Phase:** The Crystalline Color Superconductor (CCS) phase seems to emerge at intermediate densities, lower indeed than 2SC. This phase arises due to non-uniform pairing of quarks, specifically when there is a mismatch between the Fermi surfaces of the quarks involved in the pairing, often resulting from differing quark chemical potentials or in the presence of an external magnetic field.

   In a conventional color superconductor like 2SC or CFL, quarks pair uniformly across the Fermi surface. However, when there's a significant mismatch between Fermi surfaces, uniform pairing becomes energetically unfavorable. To minimize the free energy in such situations, the system can adopt a non-uniform pairing pattern, forming a spatially modulated diquark condensate. This is analogous to the Larkin-Ovchinnikov-Fulde-Ferrell (LOFF) phase in condensed matter systems.

   The diquark condensate in the CCS phase can be represented as:

$$\langle \psi_i^a C\gamma_5 \psi_j^b \rangle \propto \Delta(\mathbf{r}) \cos(\mathbf{q} \cdot \mathbf{r}) \tag{1.6}$$

   where $\Delta(\mathbf{r})$ is the position-dependent diquark condensate, and $\mathbf{q}$ characterizes the modulation wave vector. The spatial modulation leads to a crystalline structure in the condensate, hence the name.

   This phase is intriguing not only from a theoretical perspective but also because it can have implications for the physics of compact stars. Distinct crystalline patterns could result in different transport properties and specific heat capacities, potentially influencing the observational signatures of compact stars. Moreover, it has been argued that CCS phase could be the ground state of SQM, even more energetically favourable than the unpaired one [63].

3. **Color-Flavor Locked:** For three flavors of QM at high density (asymptotically high), the most prominent color superconducting phase is the CFL phase, which could be the absolute ground state of matter at very large densities [65]. In this phase, quarks of different colors and flavors form Cooper pairs, resulting in the simultaneous breaking of chiral and color symmetries. The pairing occurs in such a way that the color and flavor indices of the quarks are locked together, leading to the name "Color-Flavor Locked". This locking ensures that all nine combinations of color and flavor for the quarks have similar Fermi surfaces, promoting an equal participation of all quarks in the pairing.

   For this phase, the diquark condensate reads:

$$-G_D \langle \psi^T C i\gamma_5 \tau_k \lambda_k \psi \rangle \tag{1.7}$$

where τ and λ are Gell-Mann matrices that specify the flavor and color pairing, respectively. The index k can only assume values 2, 5, 7. The condensate completely breaks the color symmetry, causing all gluons to gain a Meissner mass. The disruption of flavor symmetries introduces eight Goldstone bosons, with the only massless Goldstone boson being linked to the breaking of $U(1)_B$.

The CFL phase is characterized by several intriguing properties. It exhibits an exact chiral symmetry restoration, which means that the quark masses effectively vanish in this phase. Furthermore, the presence of a superconductive gap for all quark quasiparticles implies that many typical scattering processes are suppressed, leading to potentially high thermal conductivities. The locked nature of color and flavor in this phase also means that conventional weak interaction processes, which would typically scatter quarks, are strongly suppressed. As a result, neutrino emission rates might be significantly modified in the CFL phase, directly influencing the cooling of compact stars.

As as been said in the previous section, even though chiral models like NJL allow us to consider phase transitions in a very formal way, we cannot satisfy Witten's hypothesis because of the lack of a confinement mechanism.

Nevertheless, pedagogically, it is actually possible to build an EoS within the NJL framework respecting Witten by totally neglecting the quark masses. This procedure is followed in Paulucci et al. [66] and Ferrer et al. [17]. Here, the authors, willing to study the asymptotic CFL state, set all the quark masses equal to zero. This is a strong assumption for the range of chemical potential of SQSs since in the NJL model the strange quark mass is far from being null. Nevertheless, what they obtain is a potential that reads:

$$\begin{aligned}\Omega_{CFL} = \quad & -\tfrac{1}{4\pi^2}\int_0^\infty dp\, p^2 e^{-p^2/\Lambda^2}(16|\varepsilon| + 16|\bar{\varepsilon}|) \\ & -\tfrac{1}{4\pi^2}\int_0^\infty dp\, p^2 e^{-p^2/\Lambda^2}(2|\varepsilon'| + 2|\bar{\varepsilon}'|) + \tfrac{3\Delta^2}{G}\end{aligned} \tag{1.8}$$

where ε, $\bar{\varepsilon}$, ε', $\bar{\varepsilon}'$ are the dispersion relations of the quasiparticles which, as assumed, don't depend on the quark masses but only on the CFL superconductive gap Δ, on the momentum p and on the chemical potential μ. Of course, the advantage of the NJL framework is the possibility of calculating a dynamical gap that is density dependent since we can rely on the gap equation

$$\frac{\partial \Omega_{CFL}}{\partial \Delta} = 0\,. \tag{1.9}$$

Dynamical quantities are crucial when studying phase transitions and to determine which phase of QM is the ground state at a fixed chemical potential and temperature.

It is important to notice that even though the NJL model does not permit to obtain absolute stability of SQM, then it should not be used to model the EoS of SQSs, it can indeed be used to describe the core of a Hybrid Star (HyS), namely

stars having deconfined quarks sitting at their center, stabilized by the large pressure given by the rest of the nuclear matter composing the star.

1.5 Impact in astrophysics

Over the past decade, the topic of color superconductivity and dense QM in the astrophysics of compact objects has been extensively studied [51]. However, we are yet to fully grasp it. QM in a color superconducting phase is characterized by the formation of a diquark condensate. Thanks to the color, flavor, and spin attributes of quarks, various color superconducting phases are possible. At extremely high densities, as mentioned before, QCD predictions suggest that the CFL is the most likely. On the other hand, for lower densities, standard methods don't work, requiring us to rely on effective models. These models must align with experimental findings.

Indeed, at intermediate densities, like the ones which are most relevant in compact stars, perturbation theory isn't applicable. Anyway various researchers tried to explore how color superconducting matter can affect a compact star, trying to hypothesize the existence of a whole star made by just one phase of QM.

Since it is hypothesized that CFL might be intrinsically stable, it has been proposed that SQS entirely made by CFL matter can possibly exist. However, its superfluid characteristics could restrict its rotation speeds due to inefficient damping of r-modes oscillations. These r-modes oscillations, non-radial star oscillations which, when linked with gravitational radiation, result in the star's spin-down, ensure that CFL stars can't rotate at speeds exceeding 1 Hz [67].

In reality, the structure of SQSs can be more complex. Given that low energy calculations rely on effective theories, it is plausible to immagine stars where CFL matter is present only at their very core, without influencing the star rotation speed as if it was entirely composed of this phase of SQM. Indeed, condensation pattern at lower densities are expected to be, for example: 2SC, CCS, CFL-K^0, CFL-K^+, CFL-π^0 etc. [1, 63]. Moreover, a SQS can be bare or non-bare, namely it could have a thin nuclear crust on its surface or not. A bare SQS is fundamentally different from a NS in terms of its surface density and thickness. The surface density of a NS range from about 0.1 to 1 g/cm^3, whereas the thickness of the SQS surface is just around 1 fm, which is the length scale of the strong interaction. Even though the crust is this thin, it can strongly affect the cooling of the star leading to an interesting phenomenology [68].

1.5.1 Observable - glitches

It is important to investigate SQS's possible structure since it can be connected to a series of astrophysical phenomena having great importance such as glitches. Glitches are sudden increase of the rotational speed of pulsars, namely highly magnetized, rotating NSs that emit beams of electromagnetic radiation. When these beams are

aligned with the Earth, they can be detected, making these rotating stars similar to cosmic lighthouses.

A large number of pulsars we have identified exhibit these glitches, or sudden increases in their spin rate. Such an event is quantified by the relative change in spin frequency ($\Delta\Omega/\Omega$ where Ω is the rotational frequency) that occurs during the glitch itself.

Although the exact cause behind glitches remains a topic of debate and investigation, one of the prominent explanations is the starquake model. Proposed by Baym et al. [69], this model draws an analogy with earthquakes. Just as energy is stored and suddenly released in tectonic plates, causing earthquakes, energy accumulated in the crust of the pulsar can be suddenly released, leading to these starquakes or glitches.

According to the starquake model, the magnitude or size of the glitch is directly related to the amount of energy released. In simpler terms, a smaller release of energy would result in a minor glitch, while a more substantial energy release would produce a more pronounced glitch. This theory thus offers a quantitative framework to understand the relationship between the energy dynamics within a pulsar and the observable glitches we detect.

When considering the architecture of a SQS one can conceptualize a multi-layered structure of SQM due to the occurrence of phase transitions between color superconducting states.

In a very naive picture we can imagine, following the idea of Mannarelli et al. [70], two main layers constituting the SQS:

- The outermost layer that can be imagined as a crust of the star with a great rigidity. This outer crust, if it exists in the color superconductive crystalline phase (already mentioned as CCS), could play a crucial role in some of the observable glitches in the cosmos.

- An inner layer that is less rigid that can be for example CFL or even unpaired SQM.

But what makes this crust so special in the context of glitches? Its pronounced rigidity allows it to store immense amounts of energy. When the crust reaches a certain threshold, it can release this quantity of energy rapidly, resulting in substantial and sudden changes in the star's spin rate, or glitches. Of course, other possible explanation of the glitches phenomenon have been proposed during the years. Indeed, glitches can possibly have different origins, in the sense that multiple glitches mechanisms can exist, depending on the compact star characteristics.

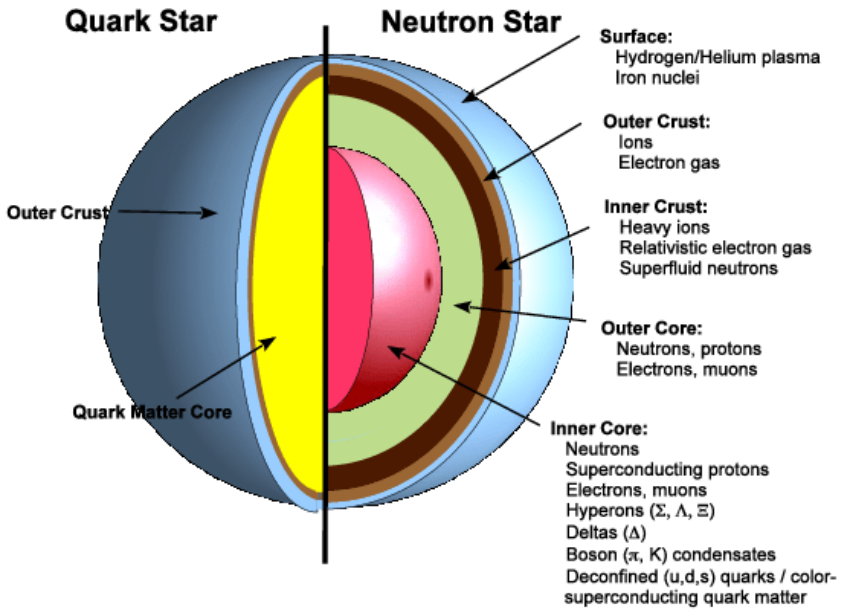

Figure 1.1: Schematic structure of a NS and of a simplified SQS from Weber et al. [1]

1.6 Compact Stars

1.6.1 Neutron stars

NSs are the remnants of massive stars that have undergone a SN explosion at the end of their lives. The formation of these exotic and dense objects is a process that involves the interplay of various physical phenomena.

The formation of a NS begins with the end of life cycle of a massive star, typically having a mass between 8 $M_\odot$ and 20 $M_\odot$. These stars undergo nuclear fusion in their cores, converting hydrogen into helium through a series of nuclear reactions. The energy generated by these reactions counteracts the gravitational force trying to collapse the star.

As the star exhausts the hydrogen, the core contracts, causing an increase in temperature and pressure. This initiates the fusion of heavier elements like helium, carbon, and oxygen. The star then undergoes a series of nuclear burning stages, forming progressively heavier elements in its core.

Eventually, the nuclear burning stages lead to the formation of an iron core. Since the iron cannot burn into heavier and more stable elements, the core cannot generate enough energy to counteract the force of gravity, leading to the core's collapse.

The core implosion happens rapidly, with the inner core reaching a density of approximately 10^{14} g/cm^3. The core's collapse proceeds until the electron degeneracy

pressure can no longer support it against further compression. Indeed, during the collapse, electrons are forced to combine with protons through inverse beta decay:

$$e^- + p^+ \rightarrow n + \nu_e. \tag{1.10}$$

This process converts protons into neutrons, releasing electron neutrinos (ν_e). As a result, the core is transformed into a dense soup of neutrons and a small fraction of protons and electrons.

As the core reaches densities akin to those in atomic nuclei, it experiences a powerful rebound in the form of a SN explosion. This explosion releases an enormous amount of energy. The expelled outer layers of the star disperse into space, enriching the surrounding cosmic environment with heavy elements produced within the star.

After the big explosion of a SN, what's left becomes a NS. These objects have radii of the order of 10-15 km and a typical weight of about 1.4.

1.6.2 Observations and constraints

The study of NSs is an intriguing pursuit that blends astrophysical observations with theoretical predictions, revealing the complex nature of these astrophysical objects. NSs serve as cosmic laboratories, providing a unique window into fundamental physics, such as the EoS for dense matter, and the extreme dynamics dictated by gravity.

NSs are brought to light through various phenomena, including pulsars, X-ray binaries, and GW signals. Pulsars, rapidly rotating NSs emitting beams of radiation, provide exquisitely accurate timing signals that facilitate measurements of crucial stellar properties, such as mass and radius. X-ray binaries, binary star systems with a NS accreting matter from a companion star, offer vital insights into NS accretion processes. The spectral features and variability of X-ray emissions help determine the mass and radius of the NS.

Recent advancements include the NICER mission [71, 4, 72], which enhances our understanding of NS compactness. By analyzing X-ray emissions from NSs, NICER offers precise measurements of NS radii, providing direct insights into their structure and EoS.

GW signals measured from the Ligo-Virgo collaboration, such as those emitted during NS mergers, furnish invaluable information about the compactness of NSs. The chirp mass and tidal deformability inferred from these signals offer essential data for understanding the EoS under extreme densities.

On the theoretical front, predictions and constraints contribute complementary insights. The EoS, capturing the intricate interplay between pressure and density in NS matter, takes center stage. Constraints on it come from nuclear physics experiments, laboratory measurements, and astrophysical observations.

The precise measurements of mass and radius obtained from pulsars, coupled with theoretical EoS models, effectively pinpoint the nature of dense matter. Observations of massive NSs challenge certain softer EoS models, prompting the need

for more stiff equations of state. In turn, theoretical models furnish predictions that guide interpretations of observations, offering detailed expectations for NS structure and behavior under extreme conditions.

1.6.3 Hyperon Puzzle

As NSs evolve, they reach a point where matter density surpasses that of atomic nuclei. At these densities, it is postulated that hyperons could become energetically favorable and appear as constituents of the dense matter within NSs [73]. The presence of hyperons softens the EoS by contributing additional pressure to counteract gravity, leading to tension between hyperonic EoSs and recent radii measurements.

One possible resolution to the hyperon puzzle involves the presence of more complicated physic. For example, hyperons might form exotic condensed phases, such as hyperon-nucleon clusters or QM, which alter the cooling dynamics [74].

Another avenue of exploration invokes repulsive hyperon-hyperon interactions [75, 76, 77], which could mitigate the presence of hyperons in the dense core of NSs. Such interactions could effectively halt the appearance of hyperons, reconciling theoretical predictions with observational data. Nevertheless, spectroscopic and lattice studies [78, 79] suggest that the channel of interaction is attractive, thus falsifying such theoretical predictions. Moreover, the speed of sound of nucleonic EoSs often violates the causal limit.

1.6.4 Hybrid Stars

The quest to unravel the hyperon puzzle has led to the exploration of HyS, a proposal that holds the potential to address the conflicting aspects of NS cooling rates while exploiting the unique properties of both hadronic and QM.

In the context of HyS, the core of a NS is envisaged as transitioning from traditional hadronic matter to (ud or uds) QM. As density rises, quarks might deconfine forming a "quark core" within the star's interior. This transition can enhance the stiffness of the EoS, counteracting the softening introduced by hyperons.

Moreover, an ingenious addition to this model is the incorporation of vectorial repulsion within QM. This repulsion, arising from vector interactions among quarks, effectively stiffens the EoS. By tuning the strength of this repulsion, the EoS can be adjusted to match both the constraints set by hyperons and the demands of cooling rate observations.

The interplay between deconfined QM and vectorial repulsion offers a promising resolution to the hyperon puzzle. The transition to QM not only provides a stiffer EoS but also introduces a diverse spectrum of possible states, including QM in CFL phase. These phases confer additional stability and robustness to the equation of state.

By incorporating deconfined QM and leveraging the effects of vectorial repulsion, this model bridges the gap between theoretical predictions and observed cooling

rates, shedding light on the complex interplay between hadronic and quark phases within NSs.

Several HyS model have been proposed in the last years but recently it has been suggested in Ivanytskyi et al. [80] that an early deconfinement is need in order to satisfy the most recent observational constraints. In the latest paper QM is treated with a chiral model which includes confinement in a similar fashion to CCDM (section 1.3).

1.6.5 Strange Stars and the two-families scenario

A fascinating astrophysical scenario for compact stars, based on the Bodmer-Witen hypothesis, the one taken into account in this thesis, is the so-called two-families scenario, described in Drago et al. [81]. The two-families scenario is a theoretical framework that suggests the coexistence of two types of compact stars: HSs and SQSs. HSs are composed of nuclear matter, including delta resonances and hyperons, while SQSs are made up of QM. This scenario allows for the possibility of different types of compact stars to exist in the universe. Moreover, it represents a natural solution to the hyperon puzzle (subsection 1.6.3).

The EoS for hadronic matter is softer, because of the presence of hyperons and delta resonances at densities more than about twice the nuclear saturation density. This allows for HSs with smaller radii and masses not exceeding $\sim$ 1.6 M$\odot$. In contrast, the EoS for QM can be stiff, leading to the SQS branch being populated by large and heavy compact stars, with possible masses up to 2.6 M$\odot$, as noted in Bombaci et al. [2].

One of the key implications of the two-families scenario is its impact on the merger of compact stars. Numerical simulations have shown that in the case of the merger of two HSs, there can be a rapid collapse to a BH, even for masses smaller than those associated with the GW170817 event. Additionally, the post-merger remnant in the two-families scenario exhibits oscillations at higher frequencies compared to the one-family scenario, namely the scenario where only one branch of compact stars exists. The merger also results in a larger mass dynamically ejected and a smaller mass of the disk surrounding the post-merger object, particularly for low total mass binaries.

This scenario suggests that the merger of a HS and a SQS is very likely, and GW170817 has a possible interpretation within this category of mergers.

Observations and estimates of various properties of compact stars, such as masses, radii, tidal deformabilities, and moments of inertia, are consistent with the predictions of the two-families scenario. In particular, objects with large radii in the universe can be interpreted as potential candidates for SQSs within this framework.

Population synthesis analysis suggests that the merger of a HS and a SQS is highly likely, especially for unequal mass systems and intermediate values of the total mass. On the other hand, mergers between two SQSs are strongly suppressed.

Moreover, this scenario has important implications also for what concerns the

merger between a BH and a NS. In the case of the two-families scenario no KN signal (or a very weak one) is expected. This is in direct contrast with the one-family scenario in which the expected KN signal can be rather strong, depending on the EoS: the stiffer the EoS, the stronger the KN signal.

It should be noticed that not all compact stars are SQSs, mainly because we have observed events compatible with the existence of NSs (SN1987a).

Combustion of an HS to SQS

If the Bodmer-Witten hypothesis holds, it should be possible to convert an HS into a SQS. This can possibly happen when the strange content of the HS is enough to trigger the nucleation of QM. Within this hypothesis hadronic matter becomes metastable and can "decay" into SQM under specific conditions. These conditions are primarily determined by the strangeness content present in hadronic matter [82, 81].

The transformation of a NS into a SQS is an intricate process that has been extensively examined in the field of astrophysics. Several studies have delved into the potential methods and mechanisms underlying this transformation.

One study conducted by Olesen and Madsen [83] explored various possibilities for the conversion of NSs into SQSs. These included scenarios like pressure-induced conversion and collisions with energetic neutrinos or smaller clumps of SQM. However, this study did not offer a specific conversion rate, leaving open questions regarding how common or rare such conversions might be.

Another investigation led by Tokareva and Nusser [84] demonstrated the feasibility of neutron-to-SQM conversion within NSs through a combustion process with a well-defined front. This study discussed the conditions for different combustion modes, such as deflagration, detonation, or fast combustion, based on the equations of state governing neutron and SQM.

Weber et al. [85] explored the potential formation of QM in the cores of NSs. They pointed out that the cores could reach densities significantly higher than the nuclear saturation density, allowing for the disintegration of neutrons and protons into their quark constituents. Furthermore, they suggested that if QM does exist within these cores, it would likely consist of the three lightest quark flavors.

In De Pietri et al. [86], it was estimated that the nucleation of the quark phase, leading to the production of SQM, becomes feasible only when the hyperon fraction exceeds approximately 0.1. This transition typically occurs at densities a few times greater than the nuclear saturation density. As a result, HSs characterized by a central density below this critical threshold are considered stable. On the other hand, only HSs with higher central densities have the potential to convert into SQSs. In this scenario, HSs and SQSs coexist, representing distinct branches of compact stars.

One distinctive aspect of the two-families scenario is the possibility of forming a SQS with a larger radius compared to an HS of the same baryonic mass (see

Fig
bec

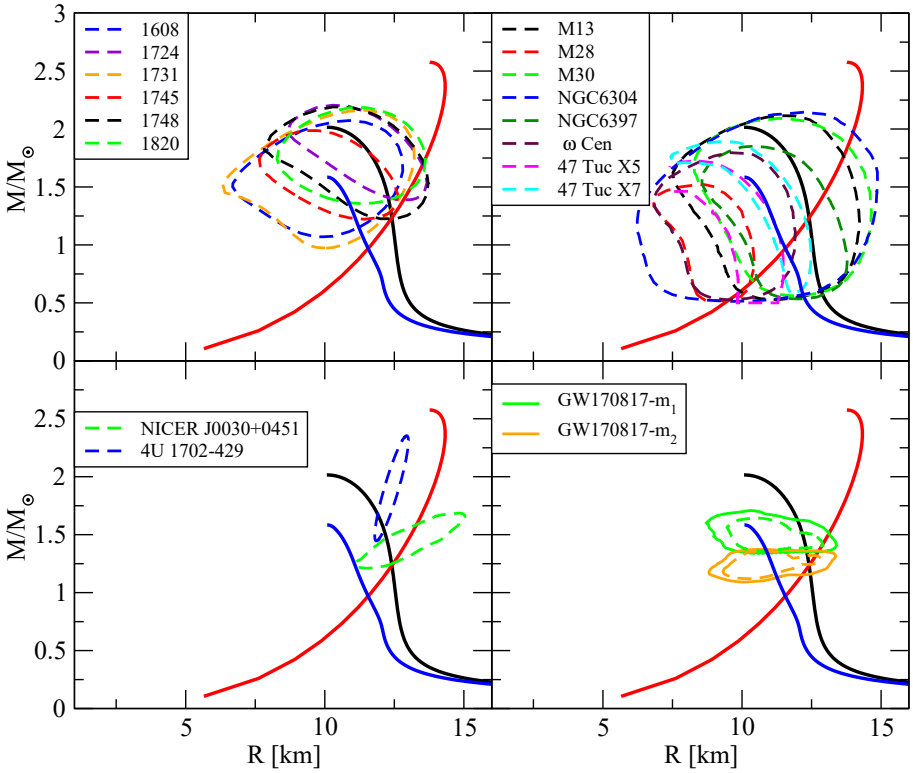

Figure 1.2: Possible MR diagram in the two-families scenario taken from Bombaci et al. [2], showing the compatibility of SQSs of the scenario with the event GW190814.

The implications of converting HSs into SQSs has been studied in several works [2, 88]. The most important feature of the conversion is that the newborn SQS has a lower gravitational mass than the original HS despite having the same baryonic content. This is a direct consequence of the Bodmer-Witten hypothesis.

In light of this scenario, it is important to take a fresh look at GW events and reinterpret them within the context of these insights. For instance, let us consider the event GW190814, where the less massive celestial object involved was not a NS, as commonly assumed, but rather a SQS.

QSs have a unique characteristic that sets them apart: they can attain masses that are comparable to those indicated by GW190814 without necessitating sound velocities violating the conformal limit ($c_s = \frac{1}{3}$ in c units) [2]. This property can be attributed to the large adiabatic index value. This means that SQSs can achieve significant mass without undergoing extreme physical conditions.

However, it is important to consider that the hypothesis of all compact stars being SQSs is unlikely. There are several reasons to support this. For instance, magnetar oscillations, as extensively studied, present challenges to the concept of

SQSs [89]. Additionally, the analysis of the energy released during the SN1987A supernova event suggests a binding energy that aligns well with that of a NS rather than a SQS [90].

Chapter 2

BHNS in the two-families scenario

2.1 Introduction

Mergers between BHs and NSs are very interesting astrophysical events. They produce GW emissions and can also manifest as strong electromagnetic (EM) counterparts, specifically, short Gamma-Ray burst (sGRB) and KN emission [91]. The disintegration of the NS results in the dynamic expulsion of material and the creation of a heated disc around the BH. These processes potentially contribute to the generation of sGRB and KN radiations. KNe are energetic events that can be a thousand times brighter than a SN, characterized by the emission of large amounts of heavy elements, created through rapid neutron capture (the r-process). The ability to generate these EM signals depends mainly on the BH mass: a very massive BH prevents the possibility of forming an accretion disc and expelling material because tidal forces that drive NS disruption are greater for smaller BHs. For BHs with masses $\lesssim 10\,\mathrm{M}_\odot$, if the dimensionless spin parameter of the system (χ) is high enough and the EoS for the compact star is not too soft, a mass around $0.01\,\mathrm{M}\odot$ can be expelled. Moreover, a larger mass, close to $0.1\,\mathrm{M}\odot$, might form an accretion disk, which could later be reduced by neutrinos, leading to more mass being ejected.

Indeed, during a merger, the ejection of matter is related to the tidal disruption of the NS. This disruption begins when the separation between the binary components (d_{tidal}) reaches a critical point where tidal forces exert enough influence to disintegrate the star. Precisely, tidal disruption occurs when d_{tidal} is greater than the innermost stable circular orbit of the BH ($R_{\mathrm{I}SCO}$), expressed as $d_{tidal} > R_{\mathrm{I}SCO}$. The approximation for d_{tidal} is given by the formula:

$$d_{tidal} \approxeq R_{\mathrm{NS}} \left(\frac{3M_{\mathrm{BH}}}{M_{\mathrm{NS}}} \right)^{1/3} \tag{2.1}$$

Here, M_{NS} denotes the NS mass, M_{BH} stands for BH mass, R_{NS} represents the NS radius, while $R_{\mathrm{I}SCO}$ is exclusively a function of the spin of the black hole (χ_{BH})[92] as it will be defined below.

In situations where this critical condition is satisfied, the ejection of material

stemming from BH-NS binary mergers can be broadly classified into two components: dynamical ejecta and matter expelled from the bound disk [93]. The subsequent calculation of crucial properties associated with these components lead to the correct calculation of the luminosity of the resulting KN, and we delve into these calculations in the following sections.

Data from NICER's study of PSR J0740+6620 indicate that the EoS for NS matter is quite rigid, especially for the heaviest compact stars [26, 3, 94]. If there is only one type of compact star, we therefore might expect a strong KN signal for many BH-NS mergers.

On the other hand, in the two-family scenario, the dynamics of BH-NS mergers show a different behavior. As described in subsection 1.6.5, in this scenario HSs and SQS s coexist. The concept of the two-families scenario was developed to address the potential existence of extremely compact stars, characterized by a radius of approximately less than 11.5 km when having a mass of around 1.4 to 1.5 $M_\odot$.

Given the inherent challenges associated with directly measuring star radii, which are susceptible to substantial systematic errors, it becomes fundamental to explore alternative methods for verifying the existence of those very compact stars characterized by exceedingly small radii. The work presented in Di Clemente et al. [33] underscores that stars featuring those radii would exhibit a very suppressed KN signal when in a BH-NS merger, offering a distinctive signature for their identification.

2.2 The ejecta mass

To obtain an approximation of the ejected mass, we employ semi-analytical models developed by Foucart et al. [95] and Kawaguchi et al. [9]. These models are constructed based on data obtained from simulations of BH-NS mergers and offer a fitting approach to estimate two crucial quantities: the mass of the accretion disk ($M_{\rm disk}$) and the mass of dynamically ejected material ($M_{\rm dyn}$). These estimates rely on five key parameters: the mass, compactness, and tidal deformability of the NS denoted as ($M_{\rm NS}$, $C_{\rm NS}$, and $\Lambda_{\rm NS}$), as well as the mass and the parallel spin component of the black hole ($M_{\rm BH}$ and $\chi_{\rm BH,||}$). Once we have estimates for $M_{\rm disk}$ and $M_{\rm dyn}$, it becomes possible to predict the intensity of the KN signal [96].

The mass of the matter that doesn't get promptly accreted by the BH, denoted as $M_{\rm out}$, comprises two distinct components. Firstly, there is $M_{\rm disk}$, which signifies the material that remains gravitationally bound to the BH. Secondly, there is $M_{\rm dyn}$, representing the portion of matter that becomes unbound. The determination of $M_{\rm out}$ is based on an interpolation formula, as described by Foucart et al. [95]:

$$M_{\rm out} = M_{\rm NS}^{\rm b} \left[\max\left(\alpha \frac{1-2\rho}{\eta^{1/3}} - \beta \tilde{R}_{\rm ISCO}(\chi_{\rm BH,||}) \frac{\rho}{\eta} + \gamma, 0 \right) \right]^{\delta} \tag{2.2}$$

where α, β, γ, δ are fitting parameters. The parameter $\chi_{\rm BH,||}$ corresponds to the parallel component of the BH spin, which depends on the dimensionless spin parameter

$\chi_{\rm BH}$ and the angle $\iota_{\rm tilt}$ representing the inclination between the BH spin axis and the total angular momentum axis. In the analyses conducted by Foucart et al. [95], they employ a crucial parameter known as the symmetric mass ratio. This choice ensures that their parametrization maintains the fit stability even when dealing with BH and NS masses that are of a comparable magnitude. It is worth highlighting that in our analyses we utilize mass ratios that are within the established range of applicability outlined in Foucart et al. [95].

In the aforementioned formula, $\rho = (15\Lambda_{\rm NS})^{-1/5}$ denotes a function associated with the tidal deformability parameter $\Lambda_{\rm NS}$. This parameter reflects the NS's response to tidal forces. Furthermore, η assumes the role of the symmetric mass ratio, and it is mathematically defined as:

$$\eta = q/(1+q)^2\,, \tag{2.3}$$

In the given equation, the parameter q is expressed as the mass ratio, specifically defined as the ratio of the NS mass ($M_{\rm NS}$) to that of the BH ($M_{\rm BH}$). $\tilde{R}_{\rm ISCO}$ corresponds to the dimensionless ISCO, which is $R_{\rm ISCO}$ rescaled by $c^2/GM_{\rm BH}$. The concept of ISCO is originally defined by Bardeen et al. [97] and plays a crucial role in the dynamics of compact object binary systems.

$$\begin{aligned}\tilde{R}_{\rm ISCO}(\chi) = 3 + Z_2(\chi) + \\ - \,{\rm sgn}(\chi)\sqrt{(3-Z_1(\chi))(3+Z_1(\chi)+2Z_2(\chi))}\end{aligned} \tag{2.4}$$

where

$$Z_1(\chi) = 1 + (1-\chi^2)^{1/3}[(1+\chi)^{1/3} + (1-\chi)^{1/3}] \tag{2.5}$$

and

$$Z_2(\chi) = (3\chi^2 + Z_1(\chi)^2)^{1/2}\,. \tag{2.6}$$

In Eq. 2.2, it is important to note that the parameters are constants which do not exhibit any dependence on the NS mass. This characteristic is due to the fact that the impact of the NS mass is encoded within the variables ρ and η. Additionally, the term $R_{\rm ISCO}$ is the BH ISCO, as the original derivation for the behavior of unbound material is done assuming the limit $M_{\rm BH}/M_{\rm NS} \to \infty$.

The estimation for the dynamical ejecta mass is provided as follows [9]:

$$\begin{aligned}M_{\rm dyn} = M_{\rm NS}^{\rm b}\Big\{\max\big[a_1 q^{-n_1}(1-2C_{\rm NS})/C_{\rm NS} + \\ - \,a_2 q^{-n_2}\tilde{R}_{\rm ISCO}(\chi_{\rm BH,||}) + \\ + \,a_3(1 - M_{\rm NS}/M_{\rm NS}^{\rm b}) + a_4, 0\big]\Big\}\end{aligned} \tag{2.7}$$

where a_1, a_2, a_3, a_4, n_1, n_2 are the fitting parameters. It is worth noting that in order to maximize the value of $M_{\rm dyn}$, the orbit should be in a prograde direction with respect to the BH spin. Consequently, in our calculations, we consider prograde orbits for this scenario and the ones that follow, i.e. $\chi_{\rm BH,||} \geq 0$.

We can proceed to estimate the mass of the accretion disk as follows:

$$M_{\rm disk} = \max\left[M_{\rm out} - M_{\rm dyn}, 0\right] \tag{2.8}$$

i.e. the bound material refers to the entirety of material located outside the BH, excluding the portion that is gravitationally unbound (ejecta).

Following Barbieri et al. [96] we set the limit for the dynamical ejecta mass as

$$M_{\rm dyn,max} = f\, M_{\rm out}\,, \tag{2.9}$$

where f is the maximum ratio between the dynamical ejecta mass and the total mass outside the BH. We set $f = 0.3$ following their estimates. It is worth to be noticed that this ratio must be $f \leq 0.5$.

Therefore, once a specific EoS for NS matter has been chosen, it becomes possible to calculate both $M_{\rm disk}$ and $M_{\rm dyn}$ as mathematical functions that depend on parameters such as $M_{\rm NS}$, $M_{\rm BH}$, and $\chi_{\rm eff}$. These parameters allow us to determine the properties of the accretion disk and the dynamical ejecta, offering an estimate of the possible KN signal.

2.3 EoSs

The recent findings from NICER have provided insights into the radii of NSs in the mass range of approximately $1.4, \mathrm{M}\odot$ up to $\sim 2, \mathrm{M}\odot$. In the left panel of Fig. 2.1, several recent constraints on NS masses and radii are displayed, including data from NICER. Notably, EoSs which are moderately soft like SFHo are only marginally consistent with this data. Instead, the observations suggest the presence of either a stiffer nucleonic EoS or a pure quark matter EoS [18].

In our analysis we employ, referring to the scenario in which only one family of compact stars exists: DD2 [98], AP3 [99] and MPA1 [100]. Additionally, two EoSs, namely 2B and SFHo+HΔ, are presented in Fig. 2.1, both of which are not in agreement with the observations. SFHo+HΔ represents a hadronic EoS that incorporates Δ-resonances and hyperons, characterizing the hadronic branch of the two-families scenario.

Compact objects associated with this branch exhibit small radii, consistent with what some authors suggest [101, 102]. On the other hand, 2B is a piece-wise polytropic EoS [103], which has been used by Barbieri et al. [96] as a reference to show that a soft EoS does not yield a strong KN signal. Notably, 2B is only slightly softer than SFHo+HΔ. Indeed in our analysis we employ just SFHo+HΔ.

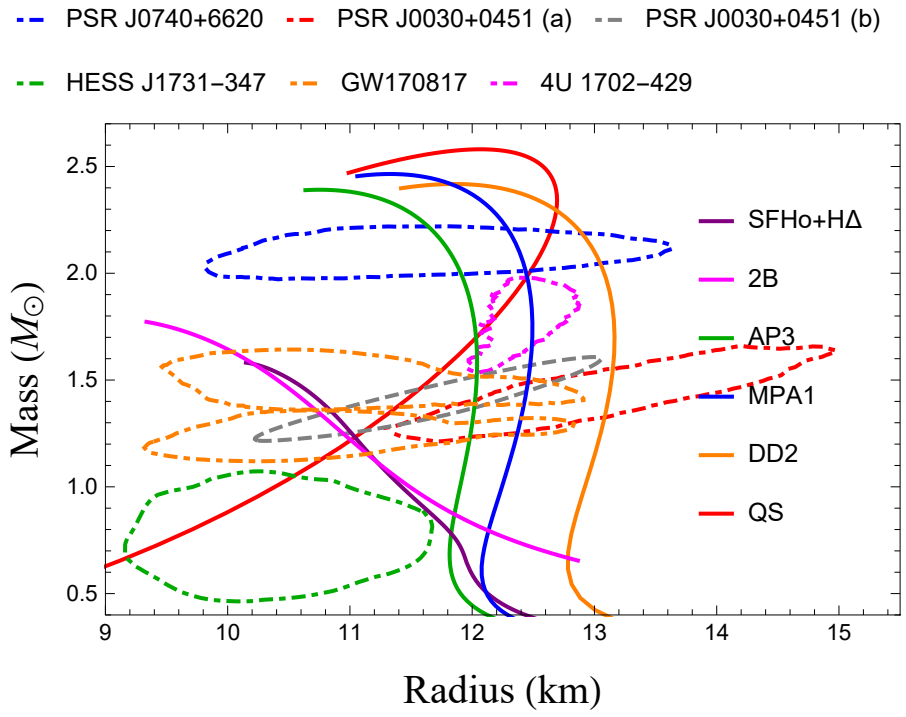

Figure 2.1: MR relation from a selected EoSs. Observational constraints at 68% confidence level (dot-dashed) for PSR J0740+6620 [3], PSR J0030+0451 (analysis *a*) [4], PSR J0030+0451 (analysis *b*) [5], HESS J1731-347 [6], GW170817 [7], 4U 1702-429 [8].

In Fig. 2.1, the constraints obtained by M. C. Miller et al. [71] are compared with results from three purely nucleonic EoSs, which represent a range of radii values consistent with observations, assuming the existence of only one family of compact stars. These EoSs include MPA1 and DD2, previously discussed in Barbieri et al. [96], as well as AP3, which is close to the lower limit indicated by M. C. Miller et al. [71].

It is worth noting that when considering a single family of compact stars, there exists a precise linear relation between the radius and tidal deformability of NSs with masses around $1.5M_\odot$ [104]. Consequently, the limits on radii directly translate into limits on the tidal deformability.

2.3.1 Ejecta and disk estimate

A strong KN signal can be generated when the EoS is stiff [91, 96]. Here we show values for both $M_{\rm disk}$ and $M_{\rm dyn}$ in the case in which only one family of compact stars exists. In this case the EoS that must adhere to constraints discussed in M. C. Miller et al. [71].

Furthermore, we compare these values with those obtained in the two-families scenario. This comparison allows us to explore the impact of different EoSs and

scenarios on the KN signal generated during such mergers. In particular, we notice that the expected ejecta in the one-family case is larger, in the majority of the cases, with respect to the two-families one.

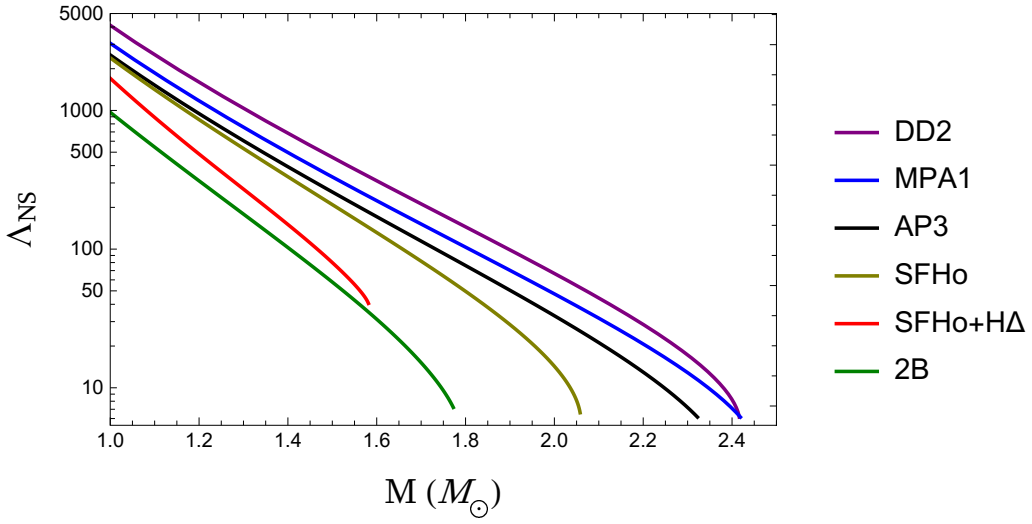

Figure 2.2: Tidal deformabilities for the EoSs considered in our analyses.

As previously discussed, the amount of ejected material during a NS- BH merger is intrinsically connected to the tidal deformability of the system. In essence, a more deformable NS is prone to disruption as it coalesces with a BH. To quantify this, we turn our attention to the tidal deformability values associated with the different EoS under consideration, which are depicted in Fig. 2.2.

The tidal deformability serves as a crucial parameter in understanding the fate of NSs in the context of BH-NS mergers. The varying degrees of deformability directly impact the potential for NS disruption during these events.

Moreover, as observed in the previous section, the dynamical ejecta exhibits a direct proportionality with the BH spin parameter, while it is inversely proportional to both the NS mass and the BH mass. The significant differences between the two scenarios, involving HSs are quite evident in the plots in Fig. 2.3, Fig. 2.4 and Fig. 2.5.

It is important to highlight that SQS s are not considered in our analysis for several crucial reasons:

- The fitting formulas used in our calculations are grounded in simulations involving HSs and BHs. Therefore, they are not applicable to SQS s, and their reliability in such scenarios is questionable.

- SQS s possess significantly higher binding energies than HSs, making them inherently more "sticky." This stickiness implies a reduced likelihood of ejecta, which would consequently lead to a suppression of the KN signal.

- A simulation indicated a suppression of KN in the case of a SQS - BH merger [105]. However, it is important to note that this simulation was performed under the Schwarzschild metric. Since the spin of the BH is a crucial factor in enhancing ejecta, future simulations will need to be conducted, accounting for the effects of BH spin in SQS - BH mergers.

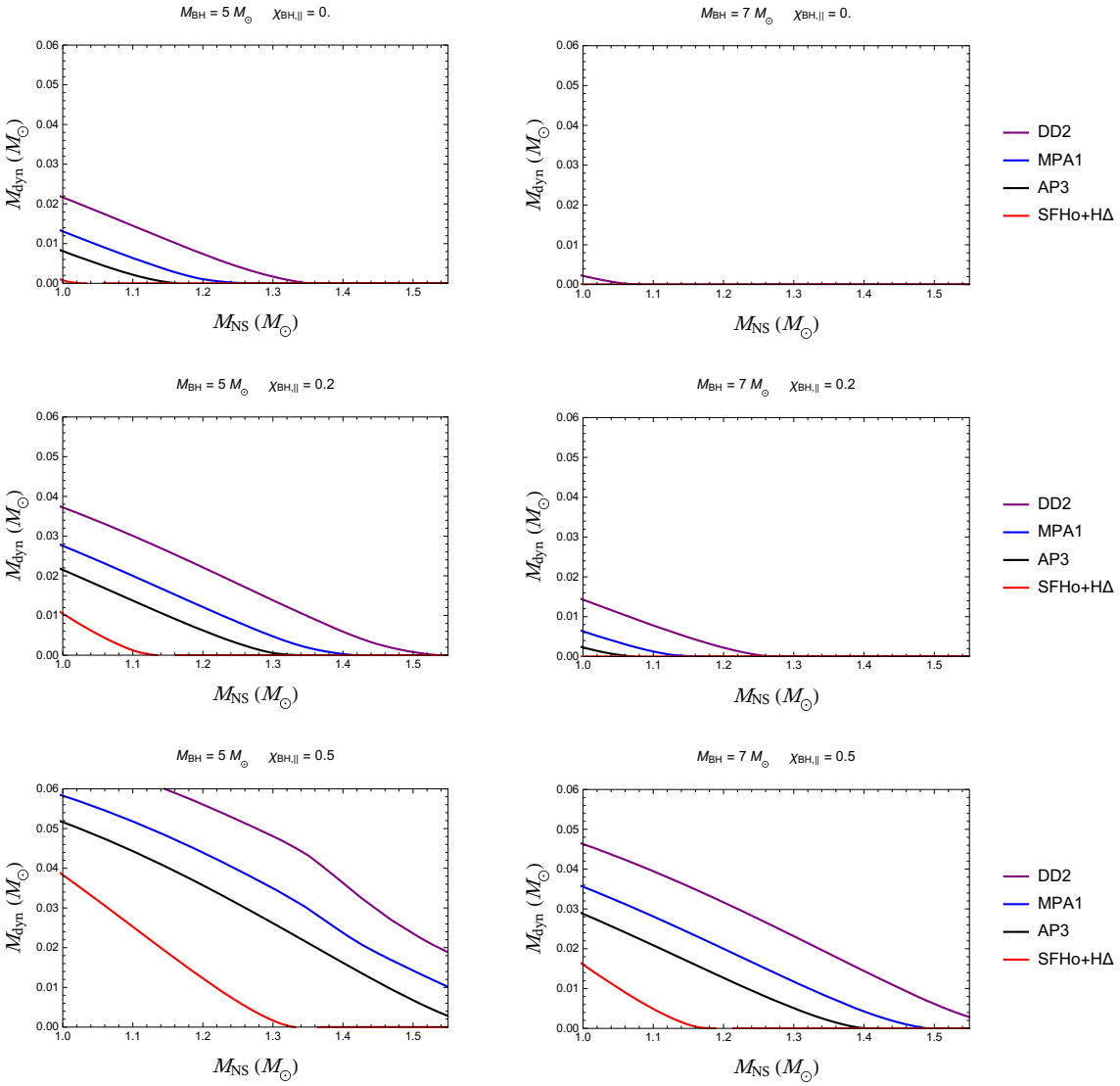

Figure 2.3: Dynamical ejecta for BH of 5 and 7 $M_\odot$ and for values of $\chi_{\mathrm{BH},||}$ of 0, 0.2 and 0.5. The ejecta are shown for the four considered hadronic EoSs and for a range of NS masses.

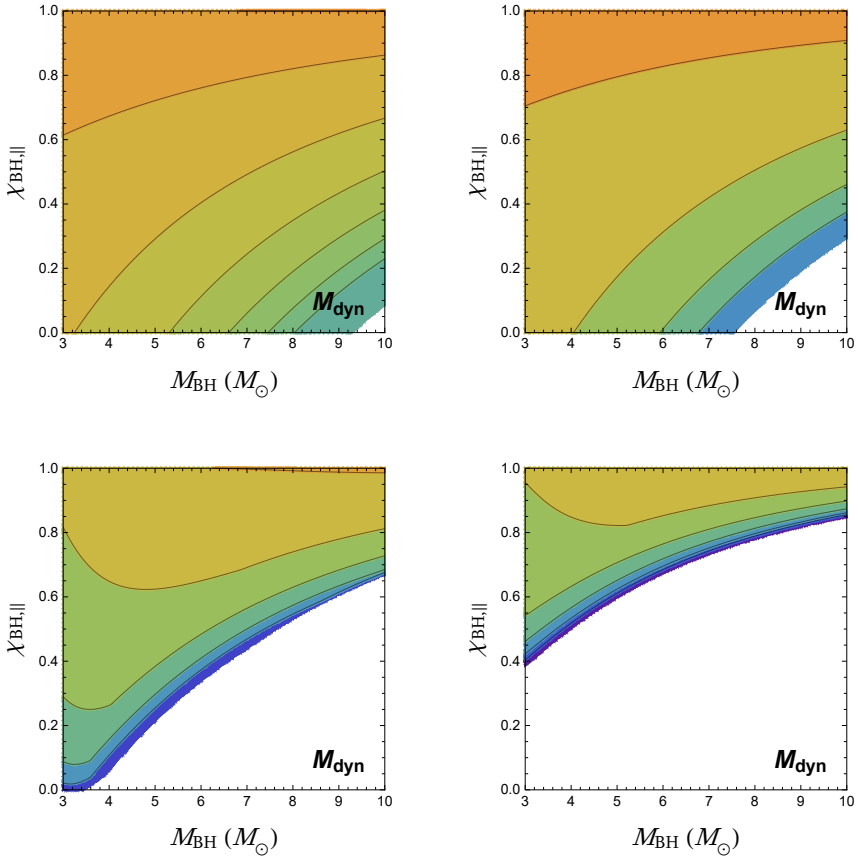

Figure 2.4: Plots of the dynamical ejecta. Left figure top is relative to DD2, right figure top to MPA1, bottom figure left to AP3, bottom figure right to SFHo+HΔ. The considered mass of the star is in all the plots $\sim 1.4\,M_\odot$. Values for tidal deformability for SFHo+HΔ, AP3, MPA1 and DD2 are respectively ,$\Lambda_{\rm NS} \simeq 142$, $\Lambda_{\rm NS} \simeq 401$, $\Lambda_{\rm NS} \simeq 462$ and $\Lambda_{\rm NS} \simeq 571$. Plots are function of the BH mass ($M_{\rm BH}$) and of the parallel component adimensional spin parameter $\chi_{\rm BH,||}$.

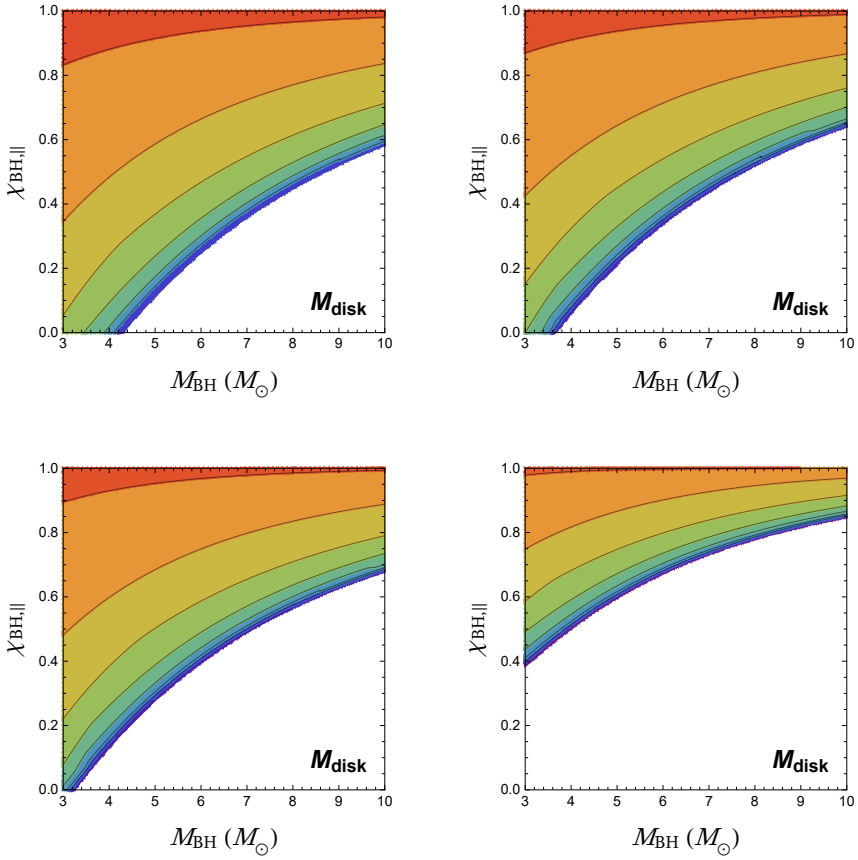

Figure 2.5: Plots of the mass of the disk. Left figure top is relative to DD2, right figure top to MPA1, bottom figure left to AP3, bottom figure right to SFHo+HΔ. The considered mass of the star is in all the plots $\sim 1.4\,M_\odot$. Plots are function of the BH mass ($M_{\rm BH}$) and of the parallel component adimensional spin parameter $\chi_{\rm BH,||}$.

The insights derived from Fig. 2.3 are quite illuminating. It becomes evident that when employing the one family EoSs, a notably broad range of values for $M_{\rm NS}$ leads to substantial values of $M_{\rm dyn}$, resulting in a possibly strong KN signal. In sharp contrast, when utilizing SFHO+HΔ for the same set of parameter there could be also no mass ejection.

Furthermore, as evident from Fig. 2.4 and Fig. 2.5, where the specific case of $M_{\rm NS} \sim 1.4\,M_\odot$ is examined, it becomes apparent that there is a broad range of the parameter space for which the signal associated with the two-families scenario is effectively suppressed. In contrast, in the one-family scenario the expected signal can be quite strong.

2.4 The kilonova model

In our first analysis, we employed a phenomenological KN model by Kawaguchi et al. [9]. This model characterizes the geometry of the ejecta through a representation illustrated in Fig. 2.6. Within this framework, the authors adopt an assumption of homologous expansion, implying that each shell with the same radius possesses a velocity given by $v = r/t$, where t is the time elapsed since the merger event.

After geometric considerations, the model furnishes an expression delineating the mass of the region from which photons escape as a function of time. This relationship is expressed as:

$$\begin{aligned} M_{obs}(t) &= M_{\rm dyn} \\ &- \int_0^{\varphi_{\rm dyn}} d\varphi \int_{-\theta_{obs}(t)}^{\theta_{obs}(t)} sin\theta d\theta \int_{v_{min}}^{v_{max}} dv v^2 t^3 \rho \\ &= M_{\rm dyn} \frac{t}{t_{\rm c}} \quad (t < t_{\rm c}) \,, \end{aligned} \tag{2.10}$$

where t_c, namely the time at which the ejecta becomes visible, is

$$t_{\rm c} = \left[\frac{\theta_{\rm dyn} \kappa M_{\rm dyn}}{2\varphi_{ej}(v_{max} - v_{\rm min})c} \right]^{1/2} . \tag{2.11}$$

The average velocity, and consequently v_{min} and v_{max}, is set by an interpolation formula provided together with the ejecta mass fit and it reads:

2.12)

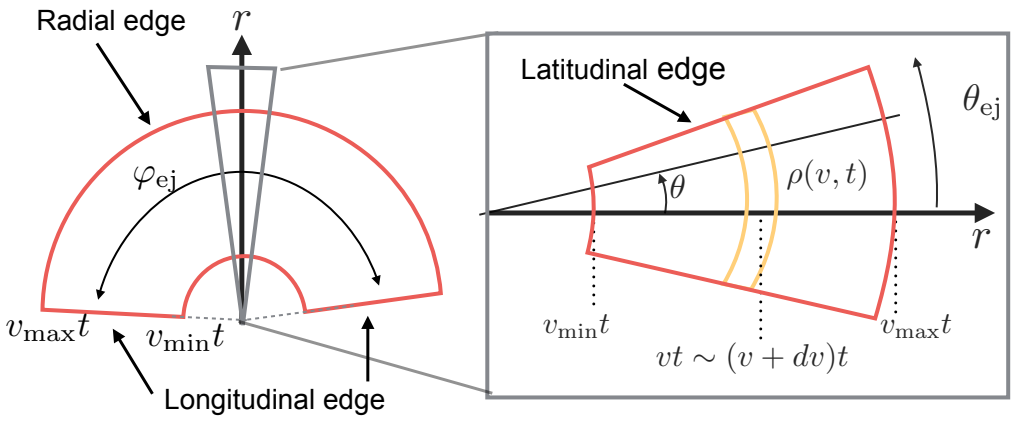

Figure 2.6: Morphology of the ejecta from Kawaguchi et al. [9].

When we consider the heating rate $\dot{\epsilon}(t) \approx \dot{\epsilon}_0 \, (t/day)^{-\alpha}$, as in Wanajo et al. [106], we can derive the bolometric luminosity which reads:

$$
\begin{aligned}
L(t) &= (1+\theta_{\rm dyn})\,\epsilon_{th}\dot{\epsilon}_0 M_{\rm dyn} \\
&\times \begin{cases} \dfrac{t}{t_{\rm c}}\left(\dfrac{t}{{\rm d}ay}\right)^{-\alpha} & t \le t_{\rm c}, \\ \left(\dfrac{t}{{\rm d}ay}\right)^{-\alpha} & t > t_{\rm c}. \end{cases}
\end{aligned}
\tag{2.13}
$$

where ϵ_{th} represents an efficiency factor associated with the thermalization process, introduced in Metzger et al. [107].

Given that the analytical calculation of bolometric corrections to determine the precise spectra of KNe is infeasible, the approach adopted in Kawaguchi et al. [9] remains fundamentally phenomenological. During the time interval in which the luminosity is primarily governed by photospheric emission, the temperature is the predominant parameter. The temperature of the photosphere can be simply estimated employing the Stefan-Boltzmann law:

$$
T_{eff} = \left(\frac{L(t)}{\sigma S(t)}\right)^{1/4}. \tag{2.14}
$$

To determine the visibility of an event with respect to the sensitivity of a telescope in a specific color band, it is necessary to compute the monochromatic magnitude. This magnitude, known as AB magnitude, is derived from the effective temperature ($T_{\rm eff}$) employed in the Boltzmann equation. The effective temperature represents the temperature that a blackbody, radiating with a particular luminosity, would exhibit on a surface denoted as S. This surface, as discussed in Kawaguchi et al. [9] and Barbieri et al. [96], explicitly depends on time.

To compute the AB magnitude, one must calculate the flux density, which is obtained from the Boltzmann equation:

$$
\Phi = \frac{S\,(2h\nu^3)}{c^2 d^2\left(\exp\left(\frac{h\nu}{k_B T_{\rm eff}}\right)-1\right)}. \tag{2.15}
$$

Then the AB magnitude in *cgs* units reads:

$$
m_{\rm AB} = -2.5\log_{10}(\Phi) - 48.6\,. \tag{2.16}
$$

While the bolometric magnitude can be directly derived from the bolometric luminosity, the AB magnitude, which is monochromatic, is derived from the energy density flux, assuming that a blackbody emits a certain bolometric luminosity, thus choosing a frequency within the chosen color band.

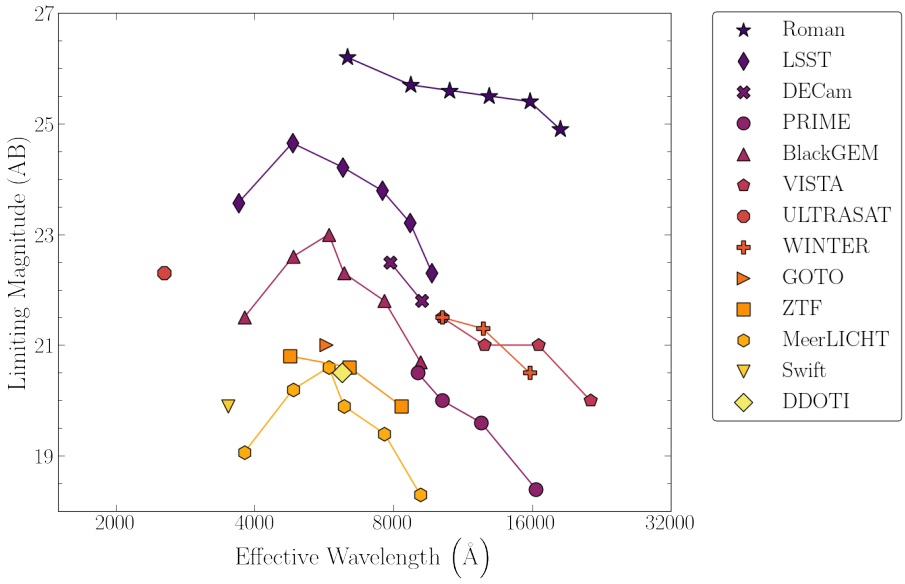

Figure 2.7: Limiting magnitude as a function of the effective wavelength for several telescopes, including *LSST* mentioned in the text, from Chase et al. [10]. It is worth to be noticed that even though Roman is more sensitive in all the wavelength its field of view is just 0.28 deg ^{2}.

Once the bolometric magnitude has been computed, it is possible to compare the expected KN signal in a given band with the sensitivity of a chosen telescope. In particular for the next future, *LSST* (Vera Rubin Observatory)[1] will be a game-changer in multi-messenger astrophysics. With its limiting magnitude (Fig. 2.7) and its field of view (9.6 deg^2) it will be crucial in observing KNe.

2.5 Simulate the observations

When observing a GW event, it is important to acknowledge that the parameters such as the masses and spins of the merging objects are susceptible to errors. These errors can arise from a variety of factors, including the distance at which the event occurs and the number of observatory interferometers in use. Therefore, there is a need for a robust method to account for these uncertainties.

GW observational data obtained from the LIGO-Virgo (LV) collaboration offer a relatively precise measurement of the chirp mass; however, the determination of individual masses and spins of the merging components is notably less accurate. During the process of data analysis, these parameters exhibit strong correlations, complicating their precise determination. To emulate this correlation, we have adopted a simplified model, as detailed in Ng et al. [108], to generate synthetic posterior distributions that mimic the outcome of actual data analysis.

[1] https://www.lsst.org/scientists/keynumbers

This model serves to illustrate how the application of Gaussian and uncorrelated likelihoods to the symmetric mass ratio and the 1.5PN phase term (referred to as ψ below) can lead to a skewed posterior distribution for the effective spin parameter of the binary system similar to the one obtained from LV. The resulting likelihood for the masses and the effective spin parameter can be expressed as follows:

$$\begin{aligned}\mathcal{L}(M_{\rm NS}, M_{\rm BH}, \chi_{\rm eff}) = \mathcal{N}(\psi(M_{\rm NS}, M_{\rm BH}, \chi_{\rm eff}); \psi_0, \sigma_\psi)\times \\ \mathcal{N}(\eta(M_{\rm NS}, M_{\rm BH}); \eta_0, \sigma_\eta)\end{aligned} \tag{2.17}$$

where the effective inspiral spin parameter is

$$\chi_{\rm eff} = \left(\frac{M_{\rm NS}}{M_{\rm NS}+M_{\rm BH}}\vec{\chi}_{\rm NS} + \frac{M_{\rm BH}}{M_{\rm NS}+M_{\rm BH}}\vec{\chi}_{\rm BH}\right)\cdot\hat{L} \tag{2.18}$$

$\hat{L}$ corresponds to the unit vector aligned with the orbital angular momentum, while $\vec{\chi}_{\rm NS}$ and $\vec{\chi}_{\rm BH}$ denote the dimensionless spin vectors of the NS and BH respectively.

Eq. 2.17 features the term $\mathcal{N}(x; x_0, \sigma_x)$, which represents a Gaussian distribution in the variable x centered at x_0 with a standard deviation of σ_x. The variable ψ is explicitly defined as follows:

$$\psi = \eta^{-3/5}\left[\frac{(113-76\eta)\chi_{\rm eff} + 76\,\delta\,\eta\,\chi_a}{128} - \frac{3\pi}{8}\right]. \tag{2.19}$$

In the formula above $\delta = (M_{\rm BH}-M_{\rm NS})/(M_{\rm BH}+M_{\rm NS})$ and $\chi_a = (\chi_{\rm BH,||} - \chi_{\rm NS,||})/2$ where $\chi_{\rm BH,||}$ and $\chi_{\rm NS,||}$ are the parallel component of the spins. The spin of the less massive body is neglected by setting $\chi_{\rm NS,||} = 0$, so that

$$\chi_{\rm eff} = \chi_{\rm BH,||}/(1+q) \tag{2.20}$$

and

$$\chi_a = (1+q)\chi_{\rm eff}/2\,. \tag{2.21}$$

In our analysis, we have incorporated the observational constraint concerning the chirp mass. This incorporation is achieved by introducing an additional multiplicative factor into Eq. 2.17, which can be expressed as follows:

$$\begin{aligned}\mathcal{L}_{\rm total}(M_{\rm NS}, M_{\rm BH}, \chi_{\rm eff}) = \mathcal{L}(M_{\rm NS}, M_{\rm BH}, \chi_{\rm eff})\times \\ \mathcal{N}(M_{\rm chirp}(M_{\rm NS}, M_{\rm BH}); M_{\rm chirp,0}, \sigma_{M_{\rm chirp}})\,.\end{aligned} \tag{2.22}$$

We distinguish each event by selecting specific central values for parameters like $M_{\rm NS,0}$, $M_{\rm BH,0}$, and $\chi_{\rm eff,0}$. This choice allows us to precisely determine the corresponding values of ψ_0, η_0, and $M_{\rm chirp,0}$. To reproduce the observed correlations documented in LV analyses, as illustrated in Fig. 4 and 8 of Abbott et al. [109], we set the standard deviations σ_ψ, σ_η, and $\sigma_{M_{\rm chirp}}$ to values which reproduce those behaviors.

In Fig. 2.8, we present the marginalized distribution functions. These distributions are obtained through a systematic Markov chain Monte Carlo approach that samples the likelihood Eq. 2.22.

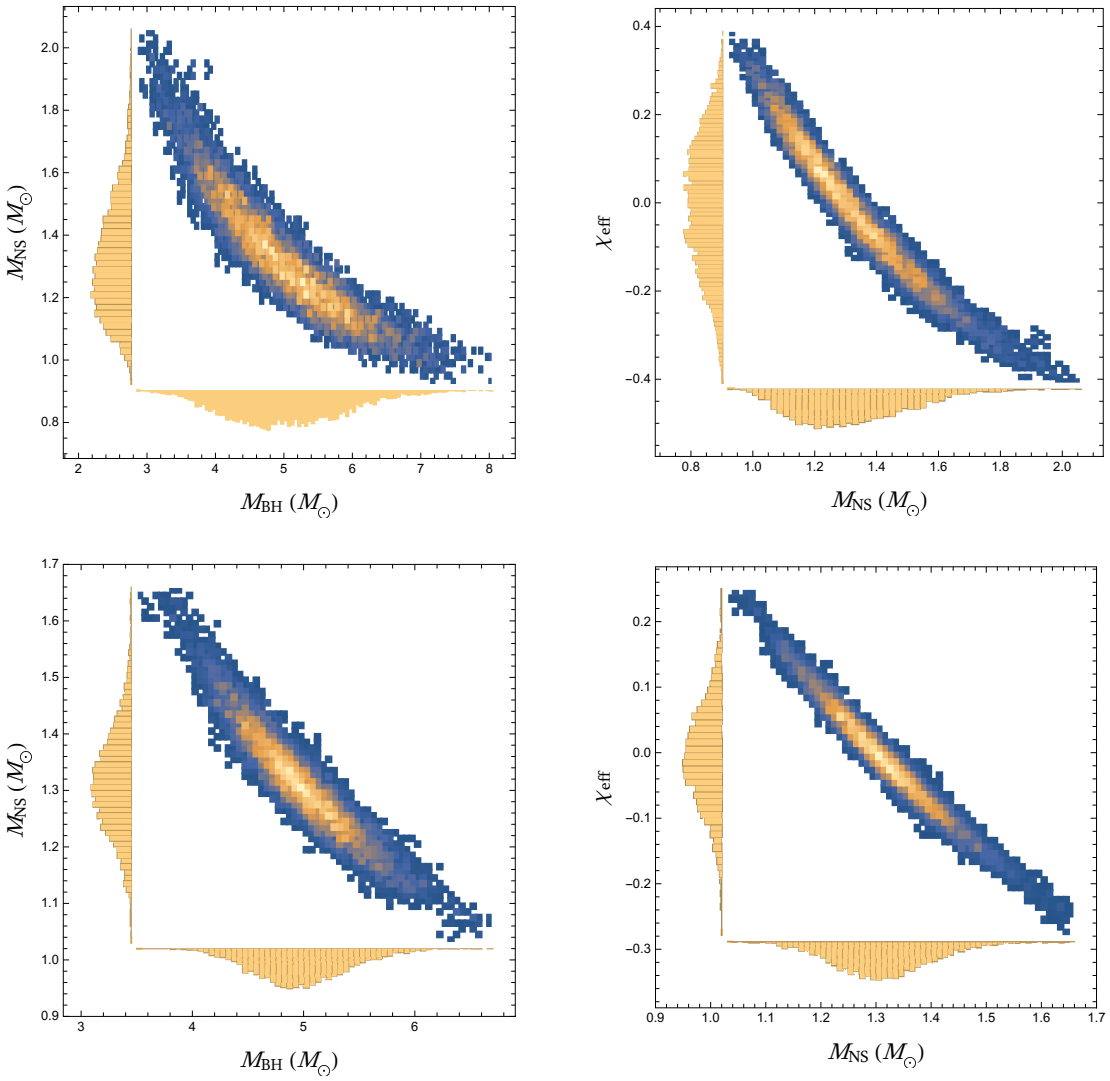

Figure 2.8: Top: example of correlations obtained with the toy-model for an event characterized by the following values: $M_{\rm NS,0} = 1.3\,{\rm M}_\odot$, $M_{\rm BH,0} = 5\,{\rm M}_\odot$, $\chi_{\rm eff,0} = 0$, $\sigma_\psi = 0.01$, $\sigma_\eta = 0.03$ and $\sigma_{M_{\rm chirp}} = 0.05$. Bottom: correlations obtained with the toy-model for the same event, with halved uncertainties. Left: correlation between $M_{\rm NS}$ and $M_{\rm BH}$. Right: correlation between $M_{\rm NS}$ and $\chi_{\rm eff}$.

2.6 Results

To assess the compatibility of an EoS with the potential detection of a KN signal, we followed a stepwise procedure:

- 1. For each hypothetical GW, we generated an ensemble of data points by employing Eq. 2.22. These data points encapsulated the uncertainties associated with the event's parameters.

- 2. Within this ensemble, we computed the mass of dynamical ejecta, denoted as $M_{\rm dyn}$. This calculation was performed using Eq. 2.7 and Eq. 2.9), which take into account the intricate physics involved.

- 3. With the calculated values for $M_{\rm dyn}$, we determine the bolometric luminosities, bolometric magnitudes, and bolometric corrections. Specifically, our focus was on a single band filter, namely the g-band filter (the filter in which *LSST* is more sensitive).

- 4. Finally, our comprehensive analysis allowed us to compute the fraction of our data ensemble that yielded a visible magnitude lower than the limiting magnitude sensitivity of the *LSST* . The results of these calculations were systematically compiled and presented as probabilities in Table 2.1.

By rigorously following these sequential steps, we were able to evaluate the likelihood of various EoSs in the context of potential KN signals.

From the probabilities of detecting a KN signal, summarized in Table 2.1, it becomes evident that the likelihood of observing a KN signal diminishes significantly when the BH spin parameter $\chi_{\rm BH}$ approaches a value of approximately 0.

To illustrate this point, consider the event labeled as *13ns7bh0c_1s*, which shares similarities with the GW200115 event. Our analysis aligns with the findings of other researchers [110, 109], indicating a very low probability of detecting a KN signal associated with this event. This outcome persists even when assuming a stiff EoS for the NS.

However, it is important to note an exception: when the BH mass is exceptionally small (typically $\chi_{\rm BH} \lesssim 5{\rm M}_\odot$) and the EoS characterizing the NS is notably stiff, there remains a possibility of observing a KN signal, even in cases involving non-rotating BHs.

To account for the anticipated enhancement in the sensitivity of future LV detectors, we factored into our analyses the possibility that the current average error, responsible for the observed correlation between estimated masses and spin, might be halved. As outlined in the table, the increased precision marginally facilitates the discrimination among various EoSs, although the overall improvement remains modest.

The principal outcome of our analysis, however, underscores a crucial observation: if BH spins are not consistently null, it becomes feasible to differentiate between distinct EoSs and, with even greater clarity, between the one-family and two-families scenarios.

As detailed in the table (and considering the dependency of $M_{\rm dyn}$ on the NS mass, illustrated in Fig. 2.3, a rather robust KN signal is expected within the one-family scenario, particularly when $M_{\rm NS} \sim (1.2 - 1.3)\,{\rm M}_\odot$ and $M_{\rm BH} \lesssim 5\,{\rm M}_\odot$, given

	SFHO+HD	AP3	MPA1	DD2
13ns5bh0c_1s	0.01	0.13	0.26	0.48
13ns5bh0c_05s	0.00	0.04	0.18	0.52
13ns7bh0c_1s	0.00	0.00	0.00	0.05
13ns7bh0c_05s	0.00	0.00	0.00	0.00
13ns5bh2c_1s	0.10	0.53	0.67	0.83
13ns5bh2c_05s	0.02	0.55	0.79	0.96
13ns7bh2c_1s	0.00	0.08	0.19	0.36
13ns7bh2c_05s	0.00	0.02	0.07	0.36
13ns5bh5c_1s	0.64	0.95	0.97	0.99
13ns5bh5c_05s	0.82	1.00	1.00	1.00
13ns7bh5c_1s	0.23	0.63	0.72	0.81
13ns7bh5c_05s	0.15	0.84	0.97	1.00

Table 2.1: Probability of observing a KN signal in the g-band by LSST after 1 day from the merger event, for four EoSs at a distance of 200 Mpc. The g-band limiting magnitude (AB) has been set at 24.7 with a $\lambda_{\rm eff} = 4830$ Å following Chase et al. [24]. Labels of the event are in the format (*NS mass*$\times 10$)ns(*BH mass*)bh(*effective spin*$\times 10$) c_*X*s where if X is 1 we use the standard deviations inferred from LV analysis, if it is 05 they are halved.

a BH spin parameter $\chi_{\rm BH} \gtrsim 0.2$. Furthermore, for instances where $M_{\rm BH} \lesssim 4\,{\rm M}_\odot$, a substantial KN signal is anticipated in the one-family scenario, even when the BH is non-rotating.

In contrast, the two-families scenario and most of the analyzed cases exhibit minimal mass ejection from the BH. It is important to note that the hadronic EoS employed in our analysis is not the softest possible. Previous research (e.g., Drago et al. [81]) has explored even softer EoSs, capable of accommodating HSs with even smaller radii, similar to those suggested in Özel and Freire [101]. Consequently, a weaker KN signal may be justified within the two-families scenario.

2.7 KN simulations

We later employed a simulation [11] instead of the phenomenological KN model in order to verify our results. The calculated properties of the ejected material, including M_{dyn} (dynamical ejecta mass), M_{wind} (wind ejecta mass), and v_{dyn} (dynamical ejecta velocity), served as critical input parameters for the subsequent phase of the analysis, which involved the utilization of the 3D radiative transfer (RT) code known as `POSSIS` (POlarization Spectral Synthesis In Supernovae, [111, 112]).

`POSSIS` models the electromagnetic radiation through space. It simulates the interactions with matter via mechanisms such as absorption and scattering. In the

context of this study, POSSIS has been used to predict the light curves of KNe arising from BH-NHs mergers instead of using the model of Kawaguchi et al. [9].

The most recent version of POSSIS, as described in Bulla [112], has been employed in this analysis. It operates based on a Monte Carlo approach, employing a 10^6 individual Monte Carlo quanta, with each quanta representing a discrete photon packet. These quanta are guided through space, mirroring the EM radiation generated within the ejecta following a BH-NS merger.

To simulate the aftermath of a BH-NS merger accurately, a grid was meticulously constructed to offer a comprehensive description of the composition and structural properties of the ejecta material. In this grid, a 3D Cartesian framework was adopted, featuring a high resolution of 100 cells per dimension. This resulted in a total grid size of $100 \times 100 \times 100 = 10^6$ individual cells. The morphology of the ejecta was built based on the BH-NS grid derived from Kawaguchi et al. [113]. An example of the obtained spectra is visible in Fig. 2.9

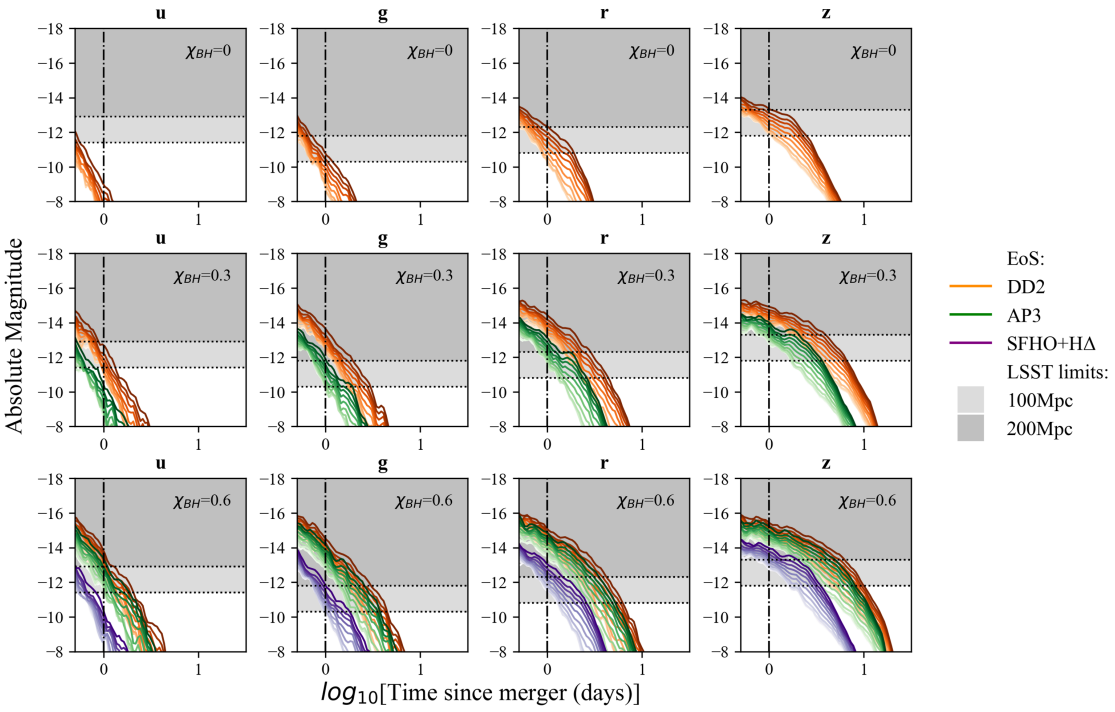

Figure 2.9: Example of the time evolution of the KN spectrum obtained with POSSIS for $M_{\rm NS} = 1.4\,{\rm M}_\odot$ and $M_{\rm BH} \lesssim 4\,{\rm M}_\odot$, varying the BH spin parameter. The plots are taken from Mathias et al. [11]

The comprehensive analysis performed with the POSSIS code confirms and extends the findings of the previous study, Di Clemente et al. [33]. The earlier work had certain limitations, particularly concerning the estimates of the ejected mass and the modeling of the KNe. The latter have been effectively addressed through

the use of this code. Due to the computational demands of the simulation, it is not feasible to run a Monte Carlo simulation that includes a large number of KN events. However, it is noteworthy that the results pertaining to individual events are consistent and align with the previous findings. This underscores the robustness and reliability of the conclusions drawn from the previous work concerning the difference between one-family and two-families scenario.

Chapter 3

Dark Matter Made of Strange Quark Matter

3.1 The beginning of a strange story

Witten [32] explores the potential occurrence of a first-order QCD phase transition in the early universe. This paper's central thesis is that such a transition in the early universe could have implications in the context of dark matter and the universe's thermal history. Witten proposes that as the universe cooled to temperatures around $\Lambda_{\mathrm{QCD}} \approx 150$ MeV, these particles transitioned into a confined state, forming hadrons. This process, known as hadronization, was governed by the principle of color confinement. This transition marked a critical shift in the universe's evolution, setting the stage for the formation of atoms and larger cosmic structures.

As one can imagine, a crucial role is played by the QCD transition temperature. Its value varies based on different approaches, with lattice QCD calculations providing a range from about 154 MeV for three-flavour QCD [114] to 271 MeV for pure gauge theory [115]. The determination of this value influences the timeline of the universe's cooling and subsequent formation of matter structures.

A second parameter which is fundamental is the Hubble time, namely the age that the universe would have had if the expansion had been linear, at the QCD transition. This is approximately 10^{-5} s, which is significantly longer than the strong interaction timescale ($\sim 10^{-23}$ s). This discrepancy indicates that the QCD transition occurred much more slowly than the time scale of strong interactions, suggesting that the transition was close to an equilibrium process [116].

A third important parameter at the time of the QCD transition is the Hubble radius, which is the scale of the observable universe, that was about 10 km. This scale is the crucial as it sets a limit on the size of causally connected regions. The Hubble radius determines the maximum distance over which processes can influence each other at a given time, playing a key role in the formation and distribution of matter during the transition.

The scales associated with the Hubble radius during the QCD transition corre-

spond to about 1 parsec or 3 light-years in today's universe [116]. The equilibrium nature of the QCD transition and its corresponding Hubble scale have implications for the Cosmic Microwave Background (CMB). Variations in the CMB can be traced back to physical processes occurring at the QCD transition, providing insights into the universe's thermal history.

This transition is hypothesized from Witten [32] to be of the first order, characterized by a discontinuous change in the state of matter at a specific temperature, approximately between 100-200 MeV as previously stated. Since the QCD transition influenced the formation and distribution of matter, including dark matter, in the early universe, it might have indeed led to the formation of quark nuggets (strangelets), baryon fluctuations, cosmic magnetic fields, and GWs. The transition could have affected the amplification of inhomogeneities, leading to dark matter clumps and modifying primordial GWs.

These nuggets, if they were to be stable over cosmic timescales, could account for a significant portion of the universe's dark matter. For this hypothesis to hold, the energy per baryon in quark matter must be less than the one of the iron, a crucial condition for the stability and formation of the strangelets.

3.1.1 GW from the QCD Epoch

Witten [32] proposed the idea that GWs might have originated from the QGP phase transition during the early universe's QCD epoch.

This transition likely occurred around 10 microseconds after the Big Bang as the universe cooled down to roughly $T_c \approx 150$ MeV. This cooling phase facilitated the transformation of quarks and gluons into hadrons. Under specific conditions, this transformation might have been a first-order phase transition, leading to the creation of bubbles within the QGP. The collision of these bubbles is hypothesized to have generated GWs.

Presently, these GWs are thought to have stretched into extremely long wavelengths, posing a challenge for direct detection. Yet, indirect detection methods, like Pulsar Timing Array (PTA), present a feasible alternative. PTAs meticulously monitor pulsar signal timings, which GWs could influence.

Given a weak GW passing by, the distance separating the earth from the pulsar depends on time and reads:

$$\tilde{L}(t) = L + \int_0^L dz \cos[k_z z - \omega(t - z)] \tag{3.1}$$

Here, L denotes the unperturbed distance of the earth from the pulsar along the z axis, k_z the wave number, and ω the angular frequency of the GW.

Witten noticed that since an experiment observing GWs for a period τ would be sensitive only to GWs having $\omega \lesssim 2\pi/\tau$, and the smallest detectable amplitude h is $h \sim \Delta t/\tau$, one can measure smaller h increasing the observation time τ. Another critical aspect is the energy density of these gravitational plane waves, represented

by:

$$\rho = \frac{\pi}{2G}\frac{h^2}{P^2} \tag{3.2}$$

In this equation, G is the gravitational constant and P its period. This equation underlines the direct correlation between a wave's energy density and its amplitude, which is crucial for detection and analysis.

Advancements in astronomical observation methods and a deeper grasp of early universe theories are essential for this pursuit. Future developments in PTAs and other GW detectors could unveil new facets of the early universe, enriching our understanding of fundamental physics and cosmology.

As now, NANOGrav collaboration [117, 118, 119] have successfully detected a GWs background studying PTAs. In the work of Agazie [118] the authors present evidence for a Stochastic Gravitational-Wave Background (SGWB) signal, correlated among 67 pulsars. This signal, detected by the North American Nanohertz Observatory for GWs is indicative of a sGWB. Frequentist statistical methods yield a significance of approximately 3.5σ to 4σ for the presence of this SGWB. The authors claim that the amplitude and spectrum of the inferred SGWB are consistent with astrophysical models of supermassive BH binaries, although other cosmological or astrophysical sources cannot be ruled out.

The paper of Gouttenoire [120], focuses on analyzing pulsar timing residuals from the same dataset as in Agazie [118]. It proposes that the detected SGWB aligns with a SGWB produced by bubble dynamics during a cosmological first-order phase transition.

In general, GWs resulting from an electroweak first-order phase transition stand as a viable candidate for detection by next-generation detectors like LISA (Laser Interferometer Space Antenna).

3.2 Observational constraints

Observations across various scales suggest our universe is largely composed of dark matter, which cannot be explained by ordinary baryonic matter or accounted for by the Standard Model of particle physics. The current understanding, supported by general relativity, posits that the energy density of the universe is dominated by a cosmological constant $\Lambda \approx 0.7$ and a non-relativistic matter component $\Omega_m \approx 0.3$, with baryons contributing only about 0.05 to Ω_m.

The nature of dark matter can be hypothesized in two ways [13]: intrinsically weakly interacting, or effectively weakly interacting due to large mass and consequently lower number density. The primary candidates for dark matter have been for a long time Weakly-Interacting Massive Particle (WIMP), but the lack of conclusive evidence from collider experiments and direct detection efforts has left their existence uncertain. Strangelets belong to the second category of dark matter.

In general, interaction rates of dark matter with baryons are a function of the dark matter's number density n_X, interaction cross-section σ_X, and a characteristic

velocity v, leading to the concept of the reduced cross-section σ_X/M_X (σ_X indicates the cross section, M_X the mass). If we consider that local dark matter density is approximately 7×10^{-25} g cm^{-3} and if we hypothesize objects with mass on the order of 10^{18} g would impact Earth roughly once every billion years, hence the low expected flux of macros.

Therefore, the analysis of macro dark matter involves evaluating the expected impact rates of macros on various astronomical bodies like neutron stars, white dwarfs, the Sun, the Earth, and the Moon. This is crucial to impose constraints based on current observations.

Firstly, we want to set a constraint on the maximum size of macro dark matter: the maximum mass of macros formed by post-inflationary causal processes which is constrained by the dark matter within the causal horizon at the time of formation $M_{H_{\rm dark}}$, given by

$$M_{H_{\rm dark}} = \frac{4\pi}{3}\rho_X(T)L_H^3 \sim \frac{10^{35}\ \mathrm{g}}{\left(\frac{T}{10^9\ \mathrm{K}}\right)^3} \tag{3.3}$$

where T is the formation temperature.

Given an isotropic flux of macros on a convex target, the impact rate Γ reads [13]:

$$\Gamma = \frac{1}{4} n_X v_X A_T f_G \tag{3.4}$$

where A_T is the target area, v_X is the average macros velocity, and $f_G = \left(1 + \frac{v_{\rm esc}^2}{v_X^2}\right)$, is the gravitational focusing factor ($v_{\rm esc}$ is the escape velocity). The total impact rate, accounting both for geometrical and gravitational factor, is then calculated as

$$\begin{aligned}\Gamma = 2.7 \times 10^5\,\mathrm{s}^{-1} &\left(\frac{1\mathrm{g}}{M_X}\right)\left(\frac{v_X}{250\ \mathrm{km\ s}^{-1}}\right)\left(\frac{R_T}{R_\odot}\right)^2 \\ &\times \left(1 + 6.2\frac{R_\odot}{R_T}\left(\frac{250\ \mathrm{km\ s}^{-1}}{v_X}\right)^2 \frac{M_T}{M_\odot}\right) f_\rho\,,\end{aligned} \tag{3.5}$$

where $M_{\rm T}$ and $R_{\rm T}$ are the mass and radius of the target, f_ρ si a density enhancement factor that is equal to unity in the solar neighborhood. This formula provides a way to estimate the frequency of macros impacts on various celestial bodies, taking into account their size, mass, and the gravitational focusing effect.

3.2.1 Ancient Mica

In examining the potential impact of macros on ancient mica, the study of Jacobs et al. [13] utilizes existing constraints and the physical properties of mica to assess the possibility of detecting some traces. It emphasizes that the energy loss rate in

the mica must have exceeded a certain threshold for a macro of mass M_X to leave a detectable track.

The constraints obtained based on the absence of traces left on the samples of Price and Salamon [121] (having 500 Myr) read:

$$\frac{\sigma_X}{M_X} > 3.6 \times 10^{-6} \text{ cm}^2 \text{ g}^{-1}$$

$$M_X > 55 \text{ g}.$$

These values set a lower limit on the interaction strength of macros, therefore excluding very low mass macros.

3.2.2 Gravitational lensing

Femtolensing, a phenomenon where the gravitational field of a compact object causes detectable interference in the light from a distant gamma-ray burst, provides stringent limits on the mass of compact objects [12]. Using Fermi satellite data, Barnacka et al. [122] have set a limit of contribution to dark matter mass of 8%, for compact object having masses in the range of $5 \times 10^{17} < M_X < 2 \times 10^{20}$ g.

In Singh Sidhu and Starkman [14] those limits are taking into account the analysis of Katz et al. [123] which revised femtolensing, states that there is no such a limit. It is worth to notice that in the latter cases the macros are assumed to be monochromatic while strangelets in our model are not.

The analysis on microlensing also rules out macros in the range of mass $5 \times 10^{22} < M_X < 4 \times 10^{24}$ g as the dominant component of dark matter. Moreover, macros having $M_X \geq 10^{24}$ g are ruled out too [13].

Moreover, experiments such as EROS and MACHO have notably constrained the mass range of macros. They have effectively ruled out objects with most masses below $10^{-7} M_\odot$ and in the range $4 \times 10^{26} < M_X < 4 \times 10^{33}$ g as the dominant component of galactic dark matter [12].

3.2.3 Seismic events

The impact of massive objects like strangelets on Earth and other planetary bodies, can potentially result in unique phenomena like anomalous meteors or seismic signals. Therefore, there are several constraints on the masses and compositions of these objects [12].

The seismic detection method is based on the hypothesis that when a macroscopic object traverses through a planet, it induces seismic waves due to its interaction with the planet's interior. Theoretical models predict these interactions, and the resulting seismic signatures are used to identify the passing of such objects.

The unique characteristics of the seismic signals produced by these objects, such as their amplitude and frequency spectrum, are key to differentiating them from conventional seismic events. The signal's amplitude is directly related to the mass

of the object, while the frequency spectrum is influenced by its velocity and angle of entry.

Referring to events on the Earth, one can exclude that the dominant component of macroscopic dark matter has mass in the range $10^5 < M_X < 3 \times 10^8$ g. Moreover, from the measurements of the total amount of the seismic energy obtained using the seismic station on the Moon implanted during the Apollo missions, one can states that less than 10% of dark matter density is in the mass range $5 \times 10^4 < M < 10^6$ g [12, 124].

3.2.4 Proto-neutron stars

The idea that all the compact stars could be SQSs faces several empirical challenges. One such challenge is presented by the characteristics of magnetar oscillations. Magnetars, a type of neutron star with extremely strong magnetic fields, exhibit oscillation modes that are not readily reconcilable with the expected behavior of SQSs. These oscillations, or quasiperiodic oscillations, observed in magnetars during giant flares, provide insights into the internal structure of these stars, posing challenges to the existence of SQSs [89].

Further evidence against the universality of SQSs comes from the analysis of supernova SN1987a. The study of the energy released during this supernova, based on the analysis of neutrino emissions and the inferred mass-energy budget of the supernova remnant, suggests compatibility with a neutron star rather than a SQS [90].

Given these considerations, it becomes evident that not all proto-neutron stars could be converted into SQSs. To support this view, the hypothetical flux of strangelets, which could potentially induce such a conversion, must be constrained within certain limits [125].

Madsen [126] investigated the potential impact of strangelets on stellar evolution. In particular, the author posed the question: if the flux of strangelets is sufficiently large, can one be captured by a star, and if so, how would this affect the star's evolutionary path? This question is especially interesting in the context of proto-neutron stars.

Proto-neutron stars represent an early stage in the life of a neutron star, typically characterized by a time span τ_{melt}, which corresponds to the first few months post-formation. During this period, a solid crust has not yet developed, thus providing a window wherein a strangelet could potentially penetrate the star [125]. Such penetration is crucial as, without a solid crust, the strangelets are not impeded by a low-density layer and can thus reach the denser regions of the star. Upon reaching these regions, a strangelet could trigger the deconfinement of the neutron star into a SQS.

For such an event to occur, certain conditions must be met. Notably, only strangelets with a mass number $A > 10^{12}$ can evade being trapped by the expanding supernova shell [127]. Additionally, the flux of strangelets F_{12} (having $A > 10^{12}$)

during τ_{melt} must satisfy the relation $F_{12} \times \tau_{\text{melt}} \ll 1$. This condition ensures that not every proto-neutron star is converted into a SQS, an outcome that would be inconsistent with astronomical observations.

3.3 Evaporation of Strange Matter

The evaporation of SQM, as discussed by Alcock and Farhi [128], is a phenomenon critical to understand the behavior of matter in the early universe. This process is particularly relevant when considering the temperature transitions the universe underwent, specifically the cooling from approximately 100 MeV to 1 MeV. During this phase, the evaporation of SQM played a significant role in determining the survival and stability of strangelets.

The stability of these strangelets is highly dependent on their baryon number. A baryon number less than a critical threshold is likely to evaporate away in the early universe. This threshold is crucial for determining the size and existence of strangelets that could contribute to the universe's matter content.

The mechanism of evaporation primarily involves the emission of nucleons from the strangelet. This process can be described quantitatively by considering the balance of energy and the number of particles involved. The energy of a strangelet, encompassing the mass and binding energies of its constituent quarks, plays a pivotal role in this balance. The evaporation rate is influenced by the temperature of the surrounding environment and the internal properties of the strangelet, including its baryon number and the energy states of its constituent quarks. The detailed calculation of the evaporation rate of a cosmological strangelet, as outlined in Alcock and Farhi [128], involves several critical factors:

- The primary consideration is the energy balance, which includes the cooling effects due to evaporation and neutrino emission, and the reheating effects from incoming neutrinos. The probability of neutrino absorption is contingent on the neutrino's mean free path, the strangelet's size, r_s, and the ambient temperature, T. The absorption probability can be expressed as:

$$p\left(r_s, T\right) = \begin{cases} 1, & r_s > \frac{3}{4} l(T) \\ \frac{4 r_s}{3 l(T)}, & r_s \leq \frac{3}{4} l(T) \end{cases} \tag{3.6}$$

  If the size of the lump exceeds the mean free path of a neutrino, it becomes opaque to neutrinos and will emit them with a thermal spectrum. The energy emission rate of strangelets, determined by its surface temperature T_s is given by

$$L_{\text{th}} = 4\pi r_s^2 (7\pi^2/160) T_s^4 \tag{3.7}$$

  indicating that the lump radiates according to its temperature T_s. On the other hand the absorption rate reads:

$$L_{\rm abs} = 4\pi r_s^2 (7\pi^2/160) T_u^4 \tag{3.8}$$

For a strangelet smaller than the neutrino mean free path, the emission and the absorption rate should be adjusted by incorporating an emission probability factor $p\,(r_s, T)$. This leads to the following total rate expression:

$$L = 4\pi r_s^2 \left(\frac{7\pi^2}{160}\right) \left[T_u^4 p\,(r_s, T_u) - T_s^4 p\,(r_s, T_s)\right] \tag{3.9}$$

- Nucleons diffusion in the dense environment surrounding the strangelets is another critical factor. By integrating the chemical potential equilibration with the binding energy and considering relevant equations, one obtains the neutrons emission rate

$$r_n = \frac{m_n T_s^2}{2\pi^2} e^{-I/T_s} f_n \sigma_0 A^{2/3} \tag{3.10}$$

where f_n is the neutron absorption efficiency and I is the binding energy. The the proton emission rate reads:

$$r_p = \frac{m_n T_s^2}{2\pi^2} e^{-I/T_s} f_p \sigma_0 A^{2/3} \tag{3.11}$$

In the latter, f_p denotes the proton absorption efficiency factor which makes the only difference with respect to Eq. 3.10.

- It's necessary to consider that nucleons close to the surface of strangelets might be reabsorbed. The rates at which neutrons and protons are reabsorbed are, respectively:

$$r_n^{\rm abs} = f_n N_n \sigma_0 A^{2/3} (T_s/2\pi m_n)^{1/2} \tag{3.12}$$

and

$$r_p^{\rm abs} = f_p N_p \sigma_0 A^{2/3} (T_s/2\pi m_n)^{1/2} \tag{3.13}$$

where N_n and N_p are the neutron and proton densities.

- The screening of incoming neutrinos by the baryons surrounding the strangelets is also significant. Assuming pressure equilibrium among electrons, positrons, photons, and nucleons (neutrons and protons), the following relation hold:

$$(N_n + N_p)\, T + \frac{11\pi^2}{180} - T^4 = \frac{11\pi^2}{180} {T_u}^4 \tag{3.14}$$

This equation modifies to include neutrino pressure, accounting for the optically thick nature of the surrounding material to neutrinos, as:

$$(N_n + N_p)\, T + \frac{43\pi^2}{360} T^4 = \frac{43\pi^2}{360} T_u^4 \tag{3.15}$$

Finally, integrating all emission and absorption terms, the net evaporation rate of a cosmological strangelet can be formulated as:

$$L = \frac{dA}{dt}\left(I + 2T_s\right) \tag{3.16}$$

$$\begin{aligned}\frac{dA}{dt} = &\left[\frac{m_n T_s^2}{2\pi^2} e^{-I/T_s} - \frac{43\pi^2}{720 T_s}\left(T_u^4 - T_s^4\right)\left[\frac{T_s}{2\pi m_n}\right]^{1/2}\right] \\ &\times \sigma_0 A^{2/3}\left(f_n + f_p\right)\end{aligned} \tag{3.17}$$

This formula incorporates the interplay of the several physical processes influencing the evaporation rate of strangelets in a cosmological context.

3.3.1 Astrophysical Strangelets

Bucciantini et al. [125] explore the phenomena surrounding the formation and evaporation of strangelets during the merger of two SQSs. The research primarily addresses the fragmentation of SQS into strangelets and their subsequent fate, especially focusing on their potential evaporation into nucleons. This study holds significance in the context of understanding the density of strangelets of astrophysical origin in the galaxy, the probability of their detection, and the implications for the strange quark matter hypothesis.

A crucial finding is that only a small amount of large-sized strangelets, ejected from the spiral arms during the post-merger phase, survive total evaporation into nucleons. It is shown that only large-size strangelets with masses above a certain threshold survive evaporation. The survival probability of strangelets is influenced by the ambient temperature and their initial mass. The evaporation time-scale τ_A is shown to be proportional to $\log A$, indicating a logarithmic dependence on the baryon number.

This leads to the conclusion that the density of astrophysical strangelets in the galaxy is insufficient to trigger the conversion of all neutron stars into SQSs, allowing for the co-existence of both types of compact objects. Furthermore, the probability of directly detecting a strangelet is found to be negligible, aligning with the current lack of experimental detection and supporting the strange quark matter hypothesis.

The study also highlights that the majority of the matter ejected during SQS-SQS mergers evaporates into nucleons, which can potentially generate KN-like signals, like those observed in neutron star mergers. This phenomenon is attributed to the process occurring close to the central region of the merger. Additionally, the authors make considerations on SQS-NS mergers, concluding that the majority of the ejected matter in such events originates from the neutron star, leading to a similar outcome regarding strangelet production and evaporation as in SQS-SQS mergers.

A key difference from studies of cosmological strangelets lies in the consideration of the fragmentation process, which is a critical phenomenon in SQS mergers but is hypothesized to be non-existent in the primordial universe. This distinction is

crucial, as fragmentation significantly influences the size distribution, and eventual evaporation of strangelets during these stellar mergers. In contrast, the cosmological investigations of strangelets typically do not account for fragmentation, leading to differing implications for strangelets distribution.

3.4 Dark matter distribution

To accurately model the current distribution of dark matter in the galaxy as strangelets, one must consider various factors, including the strangelets sizes distribution. Initially, we hypothesize a log-normal distribution of sizes and then subject it to an evaporation process. This evaporation, occurring in a range of temperature from 120 MeV to 1 MeV (section 3.3), results in a transformed distribution that must agree with the constraints specified in section 3.2.

3.4.1 Mathematical framework

It is crucial to establish a mathematical framework for handling the size distributions of the strangelets. Given an initial distribution $P(A')$, representing the number of strangelets with a baryon number A', the distribution after evaporation, denoted $Q(A)$, is given by:

$$Q(A) = \int \mathrm{d}A' P(A') \delta(A - f(A')) \tag{3.18}$$

Here, $f(A')$ is the function that maps the pre-evaporation baryon number A' to the post-evaporation baryon number A. This formulation is self-consistent: if $f(A') = A'$, it implies conservation of volume in the size space, and thus $P(A) \equiv Q(A)$. Consequently, for each value of A, the initial distribution P is transformed into the final distribution Q. It follows that if $f(A') = 0$, then $Q(A)$ becomes zero:

$$\text{if } f(A') = 0 \implies Q(A) = \int \mathrm{d}A' P(A') \delta(A) = 0\,.$$

The delta function property,

$$\delta(g(x)) = \frac{\delta(x - x_0)}{|g'(x_0)|}, \tag{3.19}$$

where x_0 is a root of g, is crucial here. Applying it to the integral formula, if $g(x) = A - f(x)$, then $x_0 = f^{-1}(A)$, assuming $g'(x)$ is non-zero at x_0. This gives us the post-evaporation distribution:

$$Q(A) = \int \mathrm{d}A' P(A') \frac{\delta(A' - f^{-1}(A))}{|f'(f^{-1}(A))|} = P(f^{-1}(A)) \frac{1}{|f'(f^{-1}(A))|} \tag{3.20}$$

This framework allows us to map the initial distribution of strangelet sizes to the distribution after evaporation, taking into account the change in baryon number and ensuring consistency with observational constraints.

3.4.2 Evaporation formula

Given the relationship that connects the age of the universe τ_U to its temperature T_u [128]:

$$\tau_U = \left(\frac{45}{172\pi^3 G}\right)^{1/2} \frac{1}{T_u^2}\,, \tag{3.21}$$

it is possible to rewrite equations Eq. 3.9, Eq. 3.16, and Eq. 3.17 as functions of the temperature T_u alone:

$$A'\left(T_u\right) = \frac{\left(\beta\, k_1\, n_0^{-2/3} A\left(T_u\right)^{2/3} \left[T_u^4 p\left(T_u, A\left(T_u\right)\right) - T_s^4 p\left(T_s, A\left(T_u\right)\right)\right]\right)}{\left(2T_s + I\right) T_u^3}, \tag{3.22}$$

$$\frac{k_2\, n_0^{-2/3} \left[T_u^4 p\left(T_u, A\left(T_u\right)\right) - T_s^4 p\left(T_s, A\left(T_u\right)\right)\right]}{\left(2T_s + I\right)\left(f_n + f_p\right)} = -\frac{k_3\left(T_u^4 - T_s^4\right)}{\sqrt{T_s}} + \frac{m_n T_s^2 e^{-\frac{I}{T_s}}}{2\pi^2}, \tag{3.23}$$

the temperature of the strangelet T_s is a function of the universe temperature T_u and the baryon number A, which itself depends on T_u, $T_s = T_s\left(T_u, A(T_u)\right)$. Here, k_1, k_2, and k_3 are constants that incorporate various physical constants into the model. Additionally, we introduce a phenomenological factor β to account for corrections, which can be of several orders of magnitude in reducing the evaporation rate, due to the strange quark mass, the running coupling constant, and finite temperature effects on the mass [127]. By solving this set of equations, one can effectively determine the dynamics of strangelet evaporation in the early universe during the cooling phase that follows hadronization. A fundamental condition to account is to limit the size of a strangelets to the size of the causal connected universe at T_u (Eq. 3.3).

3.4.3 Exploration of the phenomenological parameter space

In the quest to understand the distribution and characteristics of dark matter within the Milky Way, we consider a hypothetical scenario where the initial distribution of strangelets at the time of hadronization follows a log-normal distribution. The probability density function of a log-normal distribution for a variable x is given by:

$$f(x;\mu,\sigma) = \frac{1}{x\sigma\sqrt{2\pi}} \exp\left(-\frac{(\ln x - \mu)^2}{2\sigma^2}\right), \quad x > 0 \tag{3.24}$$

where μ and σ are the mean and standard deviation of the variable's logarithm, not of the variable x itself. We can choose the maximum value of our distribution,

or the mean value of the distribution of the logarithm of the independent variable, by using the logarithm of the mode $ln(M) = \mu - \sigma^2$, therefore introducing a new variable which corresponds to it. We rewrite μ as a function of $\mu_{\rm in} = ln(M)$:

$$\mu(\mu_{\rm in}, \sigma) = \mu_{\rm in} + \sigma^2. \tag{3.25}$$

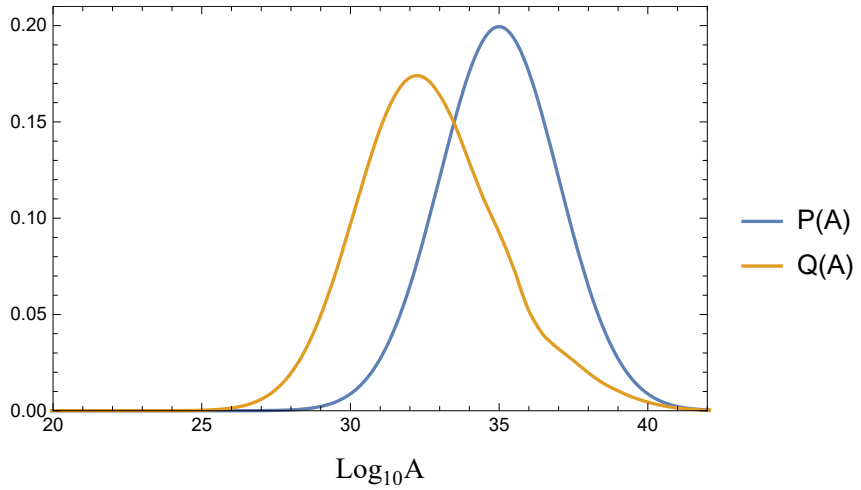

Figure 3.1: Illustration of the initial distribution $P(A)$ characterized by parameters $\mu_{\rm in} = 35$, $\sigma = 2$, and $\log_{10}\beta = -4.7$, which evolves into a final distribution $Q(A)$ as universe cools down to 1 MeV, with a central value of 32.35. The functions are normalized to the area under $P(A)$.

The initial distribution function, denoted as $P(x)$, is parameterized by its mode $\mu_{\rm in}$ (expressed in $\log_{10}$ scale) and the standard deviation σ. In the context of a log-normal distribution, the parameter σ represents the width of the gaussian in log-linear scale in terms of orders of magnitude. For instance, a σ value of 2 corresponds to a width spanning 2 orders of magnitude. We model the evolution of this initial distribution into a final distribution $Q(x)$, a process that necessitates defining the parameter β in the evaporation model described by Eq. 3.22 and Eq. 3.23.

To evaluate the viability of this model, several constraints must be considered. These include ensuring that the final distribution aligns with the observed ratio of dark matter in the Milky Way, which is approximately 90% of the total matter content [129]. Additionally, the model must agree with observational constraints as outlined in section 3.2. Through a systematic exploration of the parameter space, we correlate the initial distribution parameters with those of the final distribution. This approach enables us to control and predict key characteristics of the strangelet population, including the final maximum value in size and in mass (for the distribution of masses $A\,Q(A)$), the final the number of strangelets N, and their contribution to the overall dark matter fraction within the Milky Way.

The results of the exploration of the parameter space are presented in Appendix C. In order to generate the plots Fig. C.1, Fig. C.2, Fig. C.3, Fig. C.4, and

Fig. C.5, we employed a detailed evaporation routine. This routine was executed over a range of parameters: the initial central value of the distribution $\mu_{\text{in}} \in [30, 38]$, the standard deviation $\sigma \in [1, 2]$, and $\log_{10}\beta \in [-5, -6]$.

The selection of these parameter ranges was informed by preliminary investigations, which explored a broader parameter space. However, simulations conducted outside those ranges failed to satisfy all the constraints delineated in section 3.2. Consequently, to ensure the agreement with respect to those constraints, our analysis was restricted to these specific ranges.

By implementing the evaporation model on the initial distributions $P(x)$, and ensuring the agreement with the constraints, we have been able to calculate a range of possible size and mass distributions for strangelets.

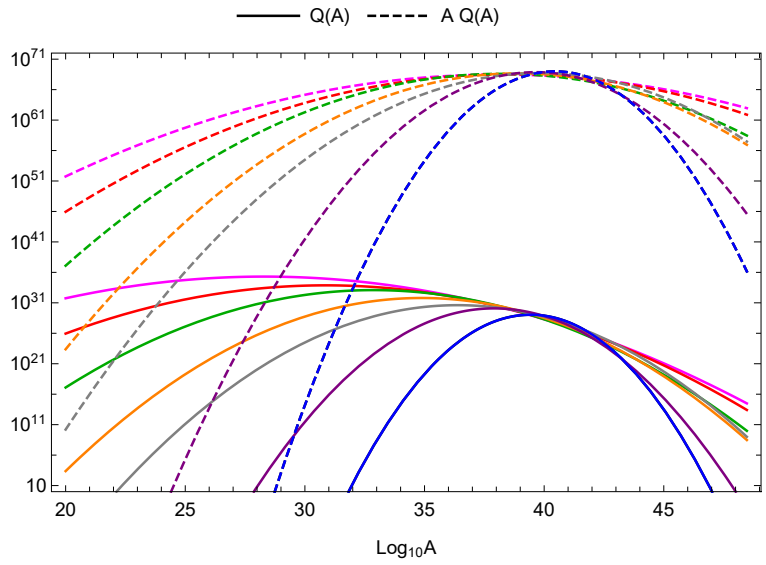

Figure 3.2: This figure showcases distributions with varying number densities and mass densities of strangelets. The represented curves, in red, green, yellow, grey, purple, and blue, correspond to distributions containing approximately 10^{34}, 10^{33}, 10^{32}, 10^{31}, 10^{30}, and 10^{29} strangelets, respectively. Notably, each curve, despite having different peak densities, has the same total mass. Furthermore, each distribution agrees with the considered observational constraints [12, 13, 14]. The distributions are normalized to the estimated dark matter mass in the Milky Way [15].

These distributions are plotted in Fig. 3.2 and they are plausible representations of the strangelets population in the universe. The diverse range of size densities and mass densities across these distributions underscores the versatility of the phenomenological evaporation model and of the accessible parameter space.

3.5 Strangelets distributions

Understanding the astrophysical implications of dark matter, particularly if a portion of it is composed of strangelets, necessitates an estimation of the strangelet flux which can interact with celestial bodies. For this purpose, we utilize a model for the dark matter density profile, such as the Navarro-Frenk-White (NFW) profile [130]. The NFW profile is a well-established model in astrophysics, widely used for describing the density distribution of dark matter in galaxies. As described in Nesti and Salucci [15], the NFW profile is given by:

$$\rho_{NFW} = \rho_H \frac{1}{x(1+x)^2}, \tag{3.26}$$

where ρ_H represents the characteristic density scale of the profile. The dimensionless variable x is defined as $x = r/R_H$, with R_H being a scale radius. The profile's slope at R_H is characterized by:

$$\left[\frac{d\log\rho_{NFW}}{d\log r}\right]_{r=R_H} = -2\,. \tag{3.27}$$

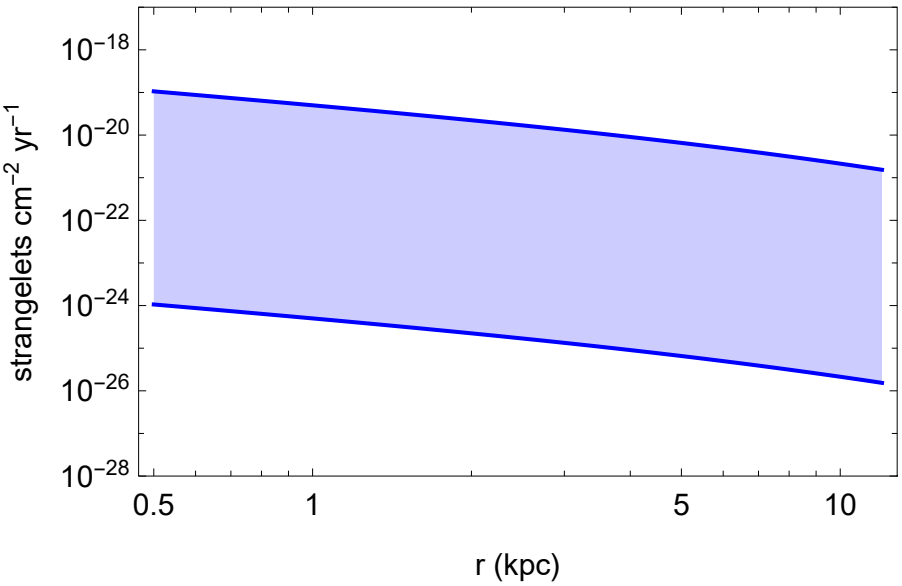

Figure 3.3: The plot illustrate the expected flux of strangelets, with the number of strangelets ranging from 10^{29} to 10^{34}, as a function of distance from the Galactic center.

Utilizing the parameters estimated by Nesti and Salucci [15], we can calculate the expected flux of strangelets as a function of distance from the center of the Milky Way. This calculation is crucial in understanding the spatial distribution and potential impact of strangelets. The results are illustrated in Fig. 3.3.

The flux profile derived from the NFW model is crucial in assessing the likelihood of detecting strangelets and understanding their distribution within the galaxy. It is important to notice that even though the NFW profile is a widely utilized model for describing dark matter density distributions in cosmic structures, yet it is not the exclusive option. Several alternative profiles exist, each with its own implications and applicability depending on the observed galactic or cluster-scale structures [131].

3.6 Astrophysical Implications

We can study the impact of the possible existence of strangelets by estimating the capture rate onto astrophysical objects as main sequence stars. Madsen [126] have already discussed the conditions to have interaction or capture of a strangelets by a stars. It is expected that a strangelets would pass through a star like the sun without being captured, given their velocity and cross section.

In order to estimate the capture rate from a main sequence star we use Eq. 3.5 opportunely modified to take into account for the strangelets number and distribution:

$$\begin{aligned} F =& 2.7 \times 10^{29} \frac{\rho_{\mathrm{NFW}}(r)}{\rho_{\mathrm{DM}}} \frac{N}{M_{\mathrm{V}}} \frac{M}{M_{\odot}} v_{250} \left(\frac{R_c}{R_{\odot}}\right)^2 \\ & \times \left(1 + 6.2 \left(\frac{R_{\odot}}{R_t}\right) v_{250}^{-2} \left(\frac{M_t}{M_{\odot}}\right)\right). \end{aligned} \tag{3.28}$$

where N is the total number of strangelets in the galaxy, M_{V} is the virial mass of the Milky Way in units of the proton mass, v_{250} is the velocity of the DM in units of 250 km/s, M is the mass of the star, R_c is the radius of the star core (which is the part of the star capable of stopping strangelets [126]). Indeed, we have extended the formula originally proposed by Jacobs et al. [13] to account for the fact that only strangelets colliding with the dense central region of a star, characterized by a radius R_c, can be halted, while others may pass through.

To estimate the capture on a star, we have to consider a star which has already formed a core dense enough to stop a strangelet. Indeed, we choose the silicon formation because the mass density would be enough to start stopping some strangelets. Therefore, in order to estimate capture probability, Eq. 3.28 has to be multiplied by $\tau(\mathrm{M})$, which is the time interval between the silicon formation in the core of a star having mass M and its collapse.

3.6.1 HESS J1731-347

The study of the central compact object within the supernova remnant HESS J1731-347, as detailed in Doroshenko et al. [6], reveals intriguing properties. Notably, the object possesses a relatively small radius and, perhaps more importantly, a

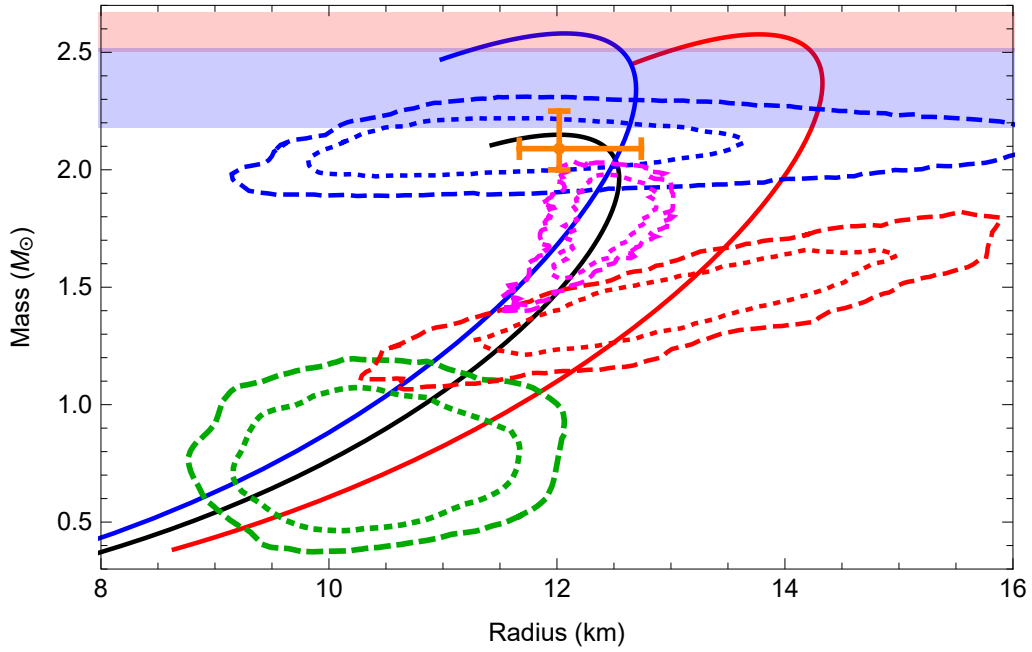

Figure 3.4: Mass-radius relation of SQSs from [16] (solid red), [17] (solid blue) and [18] (solid black) with observational constraints at 68% of confidence level (dotted) and at 90% (dashed). Blue: analysis of PSR J0740+6620 from NICER and XMM-Newton data from [19]. Magenta: analysis of 4U 1702-429 from [20]. Red: analysis of PSR J0030+0451 from [4]. Green: latest analysis of HESS J1731-347 from [6]. Orange error bars: analysis of 3XMM J185246.6+003317 from [21].

mass that is equal to or less than one solar mass (see Fig. 3.4). This finding is particularly significant as it challenges our current understanding of stellar evolution and the remnants of supernova explosions. Traditional analyses of various types of SN explosions suggest that the formation of a neutron star with a mass less than approximately $1.17 M_\odot$ is highly unlikely [132].

In response to this conundrum, we propose a scenario wherein masses on the order of or smaller than one solar mass could be accounted for by considering the possibility of SQS. These objects, characterized by their large binding energy, offer a viable explanation for the observed properties of the object within HESS J1731-347. A model based on SQSs not only explains the mass and radius of this particular object but also accounts for its slow cooling rate, as has been suggested in various studies [133, 134].

Furthermore, our analysis extends beyond the single case of HESS J1731-347. We argue that the framework of SQSs is capable of satisfying the constraints on masses and radii of other astrophysical objects, as discussed in Doroshenko et al. [6]. This model also provides a plausible explanation for the existence of objects with masses on the order of or larger than $2.5 M_\odot$. Such high-mass objects have been inferred from the analysis of gravitational wave events, notably GW190814, as

highlighted in studies by Abbott et al. [135] and Bombaci et al. [16].

SQS can possibly form with a mass of the order of or smaller than one solar mass. This is due to their large Binding Energy (BE), which comprises both gravitational and nuclear components. The gravitational binding energy contributes positively (binding) to both NSs and SQSs. However, the nuclear binding energy, which is significantly influenced by the microphysics of interactions, exhibits opposite behavior in NSs and SQSs, as showed in Bombaci and Datta [136]. While in NSs, the nuclear binding energy is large and negative (anti-binding), in SQSs, it can be small and negative or even positive [87]. This divergence results in the total BE of SQSs being markedly larger than that of NSs.

This difference in binding energies has important implications for the formation and evolution of compact objects. The collapse mechanism as detailed in Chapter 4, does not apply to HESS J1731-347, given that the central object is surrounded by a dust shell of approximately $2M_{\odot}$, ejected during the supernova explosion. Nevertheless, the large binding energy is a general property of SQSs which can always be applied.

M_b	M_g^{NS}	$M_{g,A}^{QS}$	$M_{g,B}^{QS}$	$M_{g,C}^{QS}$
1.28	1.17	0.99	1.00	$0.95 - 1.05$
1.32	1.20	1.01	1.03	$0.98 - 1.08$

Table 3.1: Comparison of the minimum allowed mass (expressed in solar mass units, $M_{\odot}$) for NSs and SQSs across three distinct models. Model A is based on the EoS presented in Bombaci et al. [16], depicted as a solid red line in Fig. 3.4. Model B utilizes an EoS derived in Ferrer et al. [17], represented by a solid blue line. Model C, illustrated as a solid black line, is derived from a Bayesian analysis described in Traversi et al. [18]. This analysis, however, does not incorporate the latest data on massive stars. The range corresponds to an energy per baryon of strange quark matter at zero pressure, $(E/A)_{p=0}$, between 765 and 850 MeV. This range aligns with the discussions in Weber [25].

In Table 3.1, we present examples of the total BEs for SQSs and NSs, highlighting these differences. Specifically, for NSs, we employ the empirical relation proposed by Lattimer and Prakash [137]: $\mathrm{BE}/M_{\odot} = 0.084(M_g/M_{\odot})^2$. This formula accurately describes the BE for a broad spectrum of hadronic equations of state, underscoring the different properties of NSs compared to SQSs.

In the study by Suwa et al. [132], it was established that the minimum baryonic mass (M_b) for the core of a SN progenitor lies within the range of $(1.32 - 1.28)M_{\odot}$. Applying the previously mentioned parameterization of the total BE for NSs, this baryonic mass range translates into a gravitational mass (M_g) in the range of $(1.20 - 1.17)M_{\odot}$.

As shown in Table 3.1, a SQS with a baryonic mass within the aforementioned range can have a gravitational mass approximately equal to or even slightly less than

one solar mass. This characteristic of SQSs, exhibiting lower gravitational masses for comparable baryonic masses relative to NSs, offers a compelling explanation for the small mass of the compact object reported in Doroshenko et al. [6]. The ability of SQSs to have a smaller M_g for a given M_b, as compared to NSs, aligns with observations of compact objects with unusually low masses, as seen in the case of the central object in HESS J1731-347 or also SAX J1808.4-3658 [138].

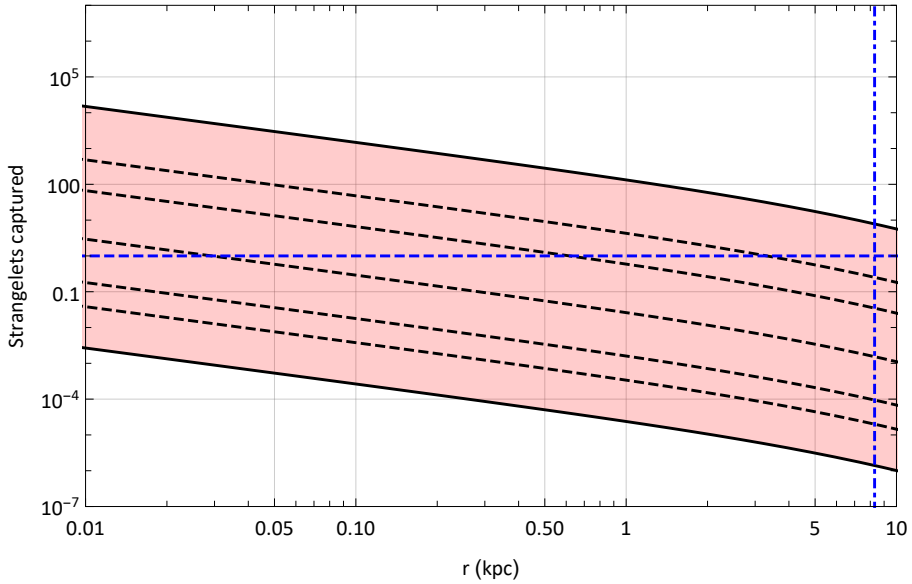

Figure 3.5: Strangelets capture probability for a core of a star with a mass of 10 $M_\odot$ in its life-span. The results for a $25M_\odot$ progenitor are nearly identical to the 10 $M_\odot$ case because the increased capture rate due to larger mass is compensated by a decrease in τ(M). The boundary curves correspond to the two extremal shown in Fig. 3.2. The vertical dashed blue line indicates the position of the Earth, while the horizontal one indicates the unitary probability. The solid and dashed black lines refer to different number of strangelets as in Fig. 3.2

.

To explain the formation of the central object in HESS J1731-347, considering the work of Suwa et al. [132], we focused on evolved stars with masses in the range of $(8-10)M_\odot$, which possess carbon-oxygen cores, as potential progenitors for low-mass NSs. Extending this concept, we aim to elucidate the specific conditions that favor the formation of a SQS rather than a NS.

The processes discussed in Suwa et al. [132] are associated with explosion, in which the resultant densities and temperatures are relatively moderate [139]. In scenarios where the central region's density is less than about twice the nuclear matter saturation density and the entropy (S/k_B) is less than or around 2, the formation of hyperons is minimal, and the nucleation of quarks is unlikely to start [140]. Consequently, without a pre-existing quark matter core in the progenitor, the spontaneous formation of a SQS appears implausible. However, if a small amount

of quark matter is already present, it could potentially initiate the deconfinement of the entire NS into a SQS.

We focused then on the capture rate by moderately dense cores of evolved stars, especially those with a zero-age-main-sequence (ZAMS) mass of about (8–10)$M_\odot$. These cores resemble white dwarfs, with masses around $(1.3 - 1.4)M_\odot$ and radii approximately $10^{-2}R_\odot$. It is also possible for a SQS to form via the capture of a strangelet by an already existing NS, though this process is feasible only before the NS develops a crust, within a timespan of roughly one month [126].

Regarding HESS J1731-347, it is positioned in the direction of the galactic center, approximately 2.5 kpc from the Sun [6]. The dark matter density in this region could be up to five times greater than that at the Sun's location [141]. Fig. 3.5 presents the estimated number of strangelets that could be captured by a 10 $M_\odot$ progenitor star. This suggests a wide array of possible strangelet distributions, implying that only proto-NSs closer to the galactic center are likely to transform into SQSs, rather than all NSs in the galaxy. Therefore, we speculate that if the progenitor of the central object in HESS J1731-347 has captured a strangelet before exploding in a supernova, it has formed a SQS instead of a NS.

Chapter 4

Strange Dwarfs

4.1 Introduction

White Dwarfs (WDs) are celestial objects that originate from the remnants of stars whose initial mass was below approximately $9\,M_{\odot}$ [142]. These stars, after undergoing their entire lifecycle and depleting their nuclear fuel reserves, enter a phase where their core contracts while their outer layers expand. This collapse is halted only when the electrons within the star core become degenerate, providing the necessary pressure to counteract further gravitational collapse.

The diverse outcomes of this process depend on the mass of the progenitor star. The nuclear fusion reactions that occur during the star's evolution can lead to the production of different types of nuclei, ultimately influencing the nature of the resulting WDs. These include helium (He) WDs, carbon-oxygen (C-O) WDs, and oxygen-neon-magnesium (O-Ne-Mg) WDs. It's essential to note that the maximum mass that a WD can attain, referred to as the Chandrasekhar mass and calculated to be approximately $1.4\,M_{\odot}$ [143], varies depending on the composition of the WD. In practice, the majority of observed WDs are of the C-O type.

In the year 1995 was proposed that WDs could possess an inner core composed of absolutely stable SQM. This notion aligns with the Bodmer-Witten hypothesis [36, 32]. What makes this concept even more intriguing is the idea that the presence of this stable SQM core has the potential to make those compact objects stable, which would otherwise be unstable. This proposal was put forth by researchers in Glendenning et al. [144, 145].

These objects, named Strange Dwarfs (SDs), exhibit characteristics distinct from those of conventional WDs. Specifically, SDs can possess different radii, masses, and astrophysical evolution pathways that differentiate them from their more conventional counterparts. It was conjectured that SDs could form either by accumulating normal nuclear matter on the surface of a SQS or through WDs gathering clusters of SQM, commonly referred to as "strangelets," that might already exist in our Milky Way galaxy.

Glendenning et al. [144] delved into the radial stability of SDs, suggesting that

these objects can remain stable even under nuclear matter envelope densities that far surpass the maximum densities observed in typical WDs.

The question concerning the stability of SDs underwent a thorough reexamination in the work of Alford et al. [22]. Their investigation revealed a critical insight: the eigenvalue associated with the fundamental radial mode of these objects was found to be negative, strongly indicating that SDs, in fact, exhibit instability.

Interestingly, in the same study by Alford et al. [22], a noteworthy observation emerged. It was suggested that the previous works by Glendenning et al. [144, 145] may have inadvertently misinterpreted their findings by confusing the second-lowest eigenmode with the lowest one. However, upon closer examination and analysis, it became evident that these two sets of research were built upon different underlying hypotheses.

Contrary to the initial belief that the two studies were grounded in the same assumptions, it became clear later that they actually operated within slightly distinct theoretical frameworks, each with its own validity. This realization effectively resolved the apparent contradiction between the results obtained by the two works.

In our work [34], we embarked on a crucial reevaluation of the stability of SDs by delving into aspects that have been neglected in prior studies. Specifically, our focus is on the boundary conditions at the interface where nuclear matter meets the quark core within SDs.

Our analysis is based on part of the formalism established in previous works, in particular Pereira et al. [146] and Di Clemente et al. [147]. These studies provide insights into the boundary conditions that can be applied in the context of rapid (and slow) conversions between nuclear matter and SQM. Crucially, that the specific boundary conditions employed can exert a substantial influence on the eigenvalues governing radial oscillations, and, by extension, they can have a profound impact on the overall stability of the star.

In addition, our study also addresses the applicability of the traditional stability criterion based on the counts of extrema in the MR plane [148, 149]. However, in this specific case, we introduce a crucial refinement to this criterion. We emphasize the need for explicit specification regarding whether the quark content of the star remains constant or undergoes changes during the radial oscillations.

4.2 Equation of state

One of the important considerations in assessing the stability of SDs lies in the nature of their EoS. Historically, when examining this aspect in previous works [144, 145, 22], the EoS was characterized by a the following formulation:

$$\varepsilon(P) = \begin{cases} \varepsilon_{\text{tov}}(P) & \text{if } P \leq P_{\text{t}} \\ \varepsilon_{\text{quark}}(P) & \text{if } P > P_{\text{t}} \end{cases} \tag{4.1}$$

In this expression, ε_{tov} represents the Baym-Pethick-Sutherland (BPS) EoS [69],

while $\varepsilon_{\text{quark}}$ denotes an equation of state characterizing SQM. An example of such an EoS could be one of the MIT bag model (as the one having the thermodynamic potential in Eq. 1.4). The critical parameter in this formulation is the transition pressure, denoted as P_{t}, which is defined as the pressure at the radius corresponding to the interface between quarks and nuclear matter. This interface marks the boundary where the EoS shifts from ε_{tov} to $\varepsilon_{\text{quark}}$.

The behavior of nuclear matter is indeed given by the BPS EoS which is used to represent ideal "limit" WDs, having a Chandrasekhar mass of approximately $1M_{\odot}$, a lower value than typical Chandrasekhar mass for C-O WDs or O-Mg-Ne WDs ($1.4M_{\odot}$ and $1.2M_{\odot}$).

It has been pointed out in Benvenuto and Althaus [150] that the use of BPS EoS is not realistic for WDs. Nevertheless, as clarified in subsection 4.5.1, it represents a limit in compactness for WDs and it is sufficient to our goals.

Usually, when dealing with EoS, one interpolates a table of parameter to consequently solve the TOV equations. In our work we used instead a fit of the EoS equation in order to avoid artifacts due to the numerical derivation of a piecewise interpolation. The form of the EoS equation fit reads:

$$\varepsilon(P) = e^{f(ln(P))}$$

where the function f is

$$\begin{aligned} f(x) = &- 1496.7952111882255 + 1109.8179718329682\, x^{1/3} \\ &- 171.06847907037277\, x^{4/3} + 95.47548413371702\, x^{5/3} \\ &- 19.652076548674618\, x^{2} + 1.4412357260222872\, x^{7/3} \\ &- 3.995517504571193 \times 10^{-14} x^{8}. \end{aligned}$$

The fit ranges in energy density from $\sim 7\text{g/cm}^3$ to $\sim 4 \times 10^{11}\text{g/cm}^3$ and it is visible in Fig. 4.1

When dealing with SDs, it is important to understand that one can use any value for ε_{t} as long as it is less than $\varepsilon_{\text{drip}} \approx 4 \times 10^{11}$ g/cm^3.

Unlike regular WDs, where one typically only needs to specify the central pressure P_0 to define a star's configuration when solving the TOV equation [151], SDs require two parameters. As clear from Eq. 4.1, the first parameter is the transition pressure P_{t}, which represents the pressure at the interface where the quark core meets the outer nuclear matter envelope, the second one is indeed the central pressure as in the normal case P_0.

The concept allowing the formation of SDs is the existence of the Coulomb barrier that separates the outer nuclear matter from the inner core of SQM. This separation occurs under the condition that the maximum density of nuclear matter remains lower than the density known as neutron drip density. Beyond this density, free neutrons start to appear. Importantly, since they are not subject to the constraints

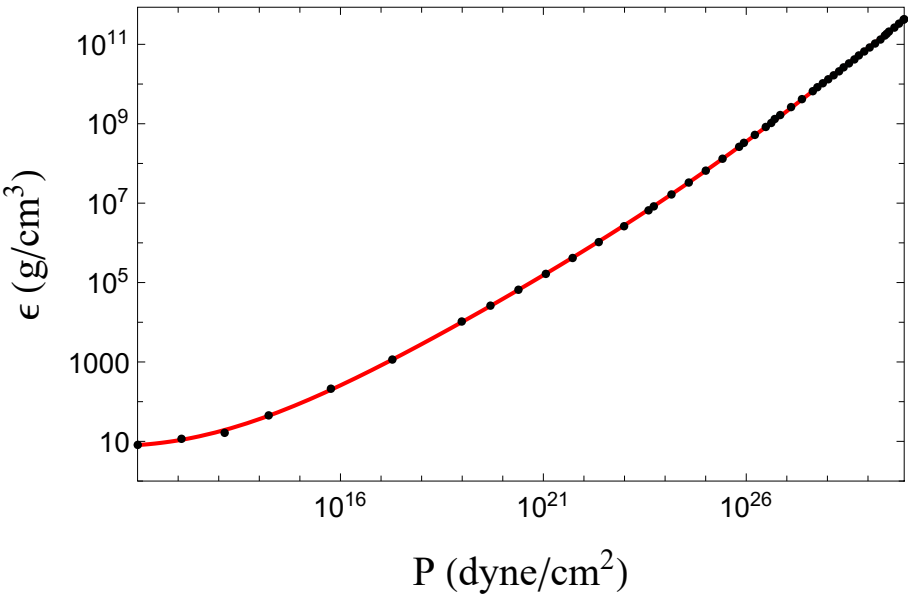

Figure 4.1: EoS equation fit in red, tabulated points in black

of the Coulomb barrier, they can readily penetrate the core of SQM. Upon entering the core, they are absorbed, leading to the deconfinement of their constituent quarks.

Given that the solutions of the TOV equation for SDs depend on two parameters, a question arises about the suitability of choosing the pair of parameters (P_0, P_t) for characterizing these configurations. Choosing a value of P_t does not account for the fact that below the neutron drip density the baryonic content of the core remains constant, despite changing the central pressure P_0. The studies by Vartanyan et al. [152] and Vartanyan et al. [153] discuss the case in which nuclear matter cannot transition into SQM, allowing for the definition of sequences of configurations that have the same quark baryon number in the core, that we define as B_core. Consequently, one can solve the TOV equation with alternative parameter pair, namely (P_0, B_core).

The quark baryon number, represented as B_core, can be expressed as follows:

$$B_\mathrm{core}(P_0, P_\mathrm{t}) = \int_0^{R_\mathrm{core}} 4\pi r^2 \frac{\rho(r)}{\sqrt{1-2m(r)/r}}, dr. \tag{4.2}$$

Here, ρ is the baryon density within the quark core. It's important to note that these two parameter choices are not interchangeable. If one opts to keep P_t constant while varying P_0, this leads to changes in B_core, implicitely indicating a scenario in which hadrons can deconfine into quarks, because the change in the core is encoded in the fact that the central pressure is changing by fixing the external pressure of the core P_t. Conversely, when B_core is maintained at a constant value, one necessitates to increase in P_t with higher values of P_0, illustrating a situation in which hadrons accumulate on the surface of the strange core without undergoing transformation into quarks.

In order to correctly consider a SD EoS at its equilibrium, we want to chose the parameter pair $(P_0, B_{\rm core})$. $B_{\rm core}$ is a function of P_0 and $P_{\rm t}$, therefore, we need to find the inverse relationship that given a choice of $B_{\rm core}$, gives back the value of the transition pressure.

In our analysis, we begin by considering Eq. B.4 in natural units ($G = c = 1$) and by using the energy density. Since the core of the system is relatively small, we can reasonably approximate the behavior using Newtonian physics in a first-order approximation.

For the EoS governing a small quantity of SQM within the core, we utilize a parametric expression:

$$P = (\varepsilon - \varepsilon_{\rm W})a, \tag{4.3}$$

Here, the variable a serves as a multiplicative parameter that encompasses various factors, including the bag constant. The term $\varepsilon_{\rm W}$ corresponds to the Witten density, defined as $\varepsilon_{\rm W} = \varepsilon(P = 0)$. Substituting n Eq. 4.3 into Eq. B.4 and separating the variables, we obtain:

$$a\frac{d\varepsilon}{\varepsilon^2} = -\frac{4\pi}{3} r\, dr. \tag{4.4}$$

Upon integrating both sides and consolidating all constants into a single parameter, denoted as K, we obtain the following relationship:

$$\int_{\varepsilon_0}^{\varepsilon_{\rm W}} \frac{d\varepsilon}{\varepsilon^2} = -K \int_0^{R_{\rm core}} dr\, r, \tag{4.5}$$

In this equation, $R_{\rm core}$ represents the radius of the core and ε_0 the energy density at the center of the system. The solution to both sides of this equation leads us to the following expression:

$$\varepsilon_0 = \frac{\varepsilon_{\rm W}}{1 - K\varepsilon_{\rm W} R_{\rm core}^2} \tag{4.6}$$

This equation encapsulates the relationship between the central energy density and the Witten density $\varepsilon_{\rm W}$, considering the parameter K and the core radius $R_{\rm core}$.

We can modify Eq. 4.6 to replace the core radius $R_{\rm core}$ with its baryon content, denoted as $B_{\rm core}$, since $R_{\rm core}^2 \propto B_{\rm core}^{2/3}$. Additionally, considering that our core experiences slight compression due to the surrounding nuclear matter, we can replace $\varepsilon_{\rm W}$ with the effective surface energy density specific to the quark core, denoted as $\varepsilon_{\rm t}^{\rm Q}$. This transition density at the boundary of the quark core satisfies $\varepsilon_{\rm t}^{\rm Q} \geq \varepsilon_{\rm W}$. The new form of the equation reads:

$$\varepsilon_0(B_{\rm core}) = \frac{\varepsilon_{\rm t}^{\rm Q}}{1 - K\varepsilon_{\rm t}^{\rm Q} B_{\rm core}^{2/3}}. \tag{4.7}$$

Now, it is reasonable to incorporate some higher-order corrections into Eq. 4.7 to account for general relativistic effects:

$$\varepsilon_0(B_{\rm core}) = \frac{\varepsilon_{\rm t}^{\rm Q}}{1 - k_1\varepsilon_{\rm t}^{\rm Q}B_{\rm core}^{2/3} - k_2\varepsilon_{\rm t}^{\rm Q}B_{\rm core}^{4/3}}, \tag{4.8}$$

In this modified equation, we introduce two numerical parameters, k_1 and k_2, to account for these higher-order relativistic effects. These parameters are determined numerically.

For the SQM, we utilize the thermodynamic potential from Eq. 1.4, in the following form:

$$\Omega(\mu) = -\frac{3}{4\pi^2}a_4, \mu^4 + \frac{3}{4\pi^2}(m_s^2 - 4\Delta_0^2)\mu^2 + B \tag{4.9}$$

Here $a_4 = 0.7$, the gap parameter $\Delta_0 = 80$ MeV, the strange quark mass m_s=120 MeV, and the bag constant $B = 135^4$ MeV^4, as in Bombaci et al. [16].

It is important to note that the parameters k_1 and k_2 are primarily influenced by the bag constant, and any reasonable adjustments made to the other parameters in Eq. 4.9 have negligible impacts on these parameters.

4.2.1 Mass-radius relationship

The relationship between mass and radius, obtained by solving Eq. B.29 and Eq. B.27, exhibits notable differences depending on whether we consider the parameter pairs $(P_0, P_{\rm t})$ or $(P_0, B_{\rm core})$. When constructing a MR diagram, it is essential to vary one parameter, typically the central pressure (or central energy density), while keeping the other parameters constant.

If we opt to fix the transition pressure $P_{\rm t}$, we are essentially exploring configurations where SQM consistently appears at the same energy density threshold. We begin with a configuration where $P_0 = P_{\rm t}$, denoted as point b (or variations like b' and b'' depending on the transition energy density), as illustrated in Fig. 4.3. Then, we progress along the bottom branch in a clockwise direction, increasing the central pressure.

In Fig. 4.3, also it becomes clear how the extreme point corresponding to the BPS EoS, joins with the curve established by fixing $\varepsilon_{\rm t} = \varepsilon_{\rm drip}$. Indeed, the curves built by choosing the transition pressure join the WD curve exactly at the point in which the WD central pressure $P_0 = P_{\rm t}$ (or $\varepsilon_0 = \varepsilon_{\rm t}$). When the transition density is relatively low, the point where the curves join falls before reaching the WDs maximum mass on the MR diagram. This is evident in Fig. 4.2, where a low energy transition density ($\varepsilon_{\rm t} = 10^7$ g/cm^3) is represented by the dashed black curve, which intersects with the BPS EoS curve at approximately 0.5 $M_\odot$.

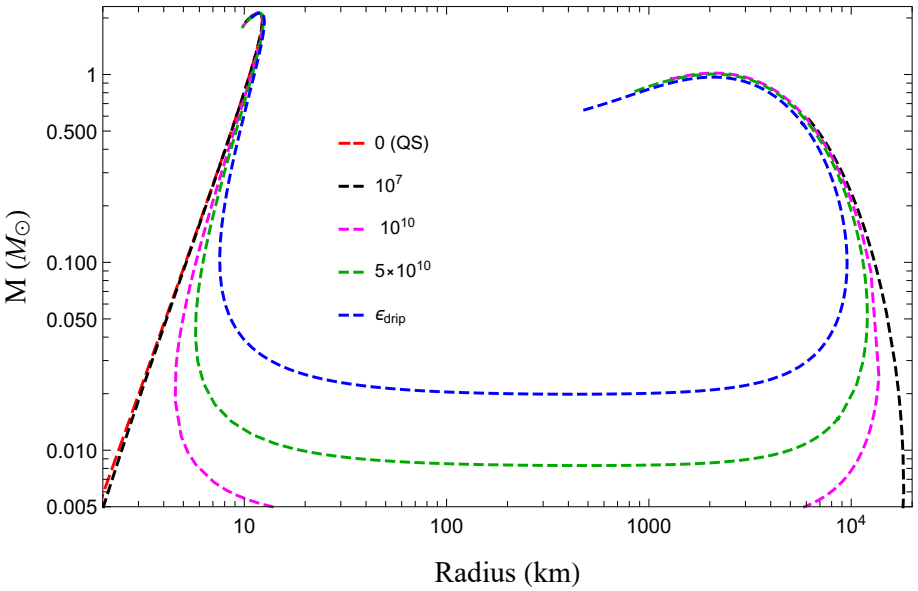

Figure 4.2: Mass-radius relationship for EoSs having fixed transition densities, indicated in the legend in units of g/cm^3. In dashed red is shown also the curve for a bare SQS, which indeed does not have a transition density to nuclear matter.

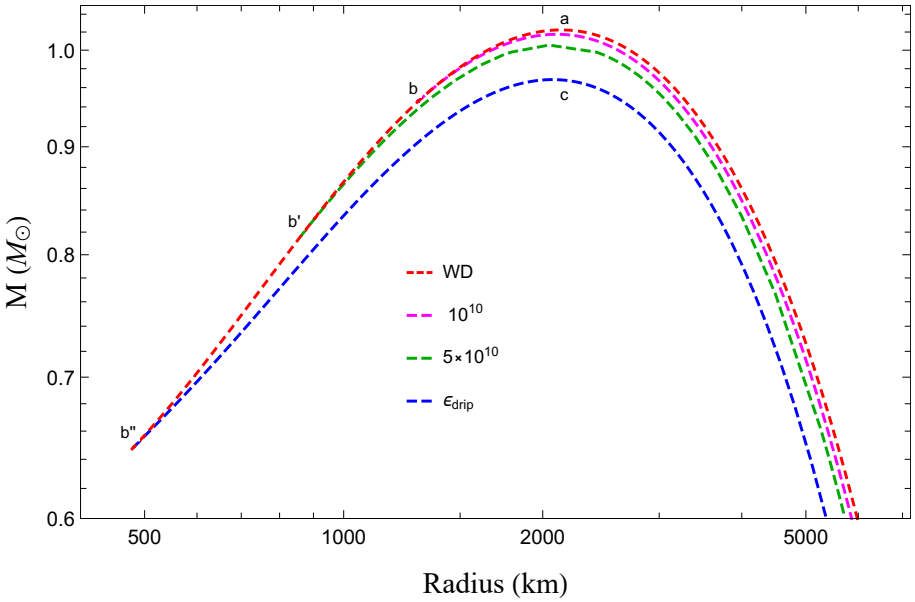

Figure 4.3: Magnification of the MR sequence close to the Chandrasekhar limit. The notation the same as in Fig. 4.2. The WD configuration (not shown in Fig. 4.2) is also displayed.

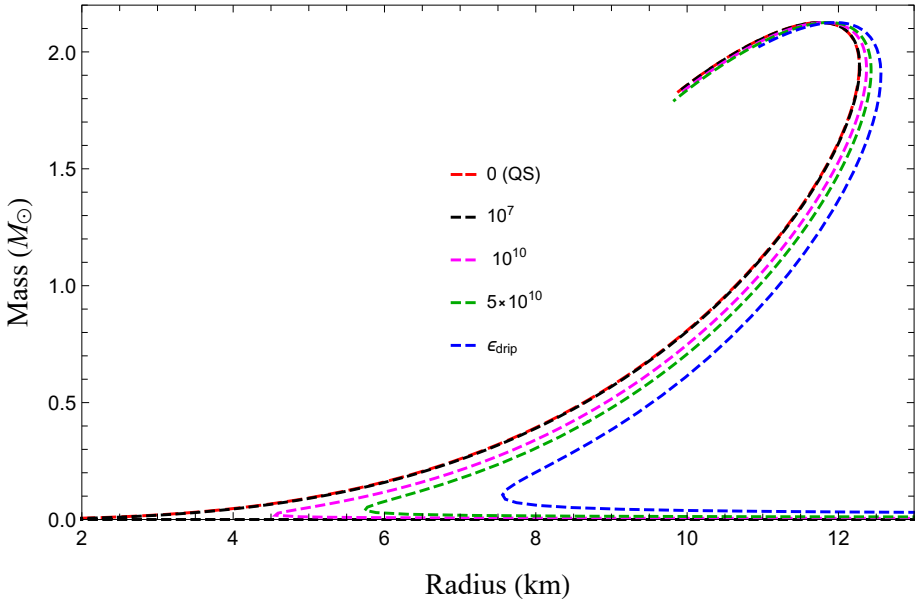

Figure 4.4: Detail of the Fig. 4.2. Here it is visible the SQSs branch, where EoSs having a constant ε_t are analogous to non-bare SQSs, namely SQSs with a nuclear crust.

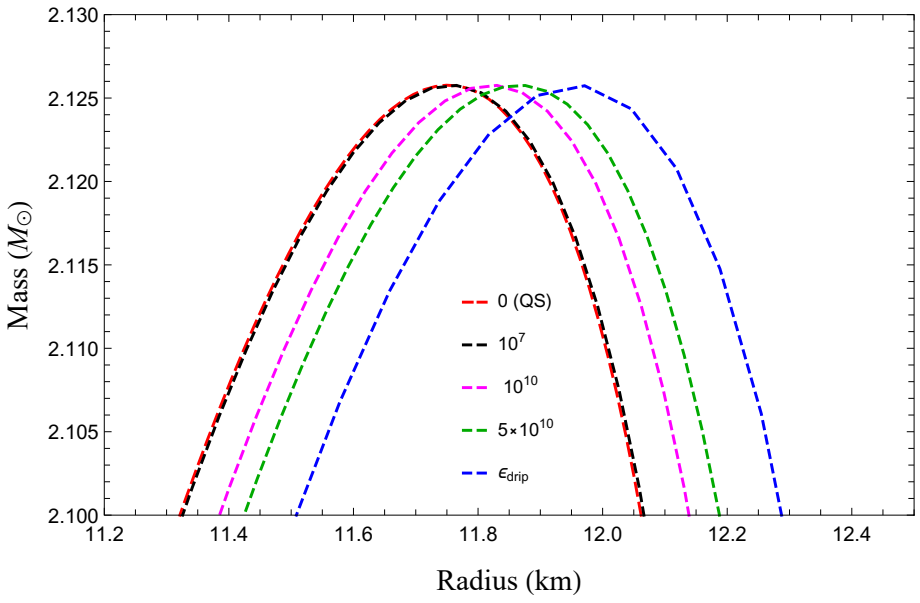

Figure 4.5: Magnification of the maxima in Fig. 4.4. The higher is the transition density of the nuclear matter and the more compact is the star. Indeed, the wider the range between the constant ε_t and the star's surface, the greater the compression exerted by the surrounding nuclear matter on the strange core.

On the other hand, the MR relationship for SDs tends to converge with that of a SQS when considering small radii. In particular, if the value of $\varepsilon_t(P_t)$ is significantly

smaller than the neutron drip density, it implies that there is not sufficient matter above the quark core (which now constitutes the majority of the star) to exert significant compression on it. For the maximum values of $\varepsilon_{\rm t}(P_{\rm t})$, specifically the neutron drip density, the radii of SDs are slightly smaller compared to those of a SQS. This occurs because there is a broader range of pressure levels that nuclear matter must cover in these cases. This behavior is evident in the Fig. 4.4.

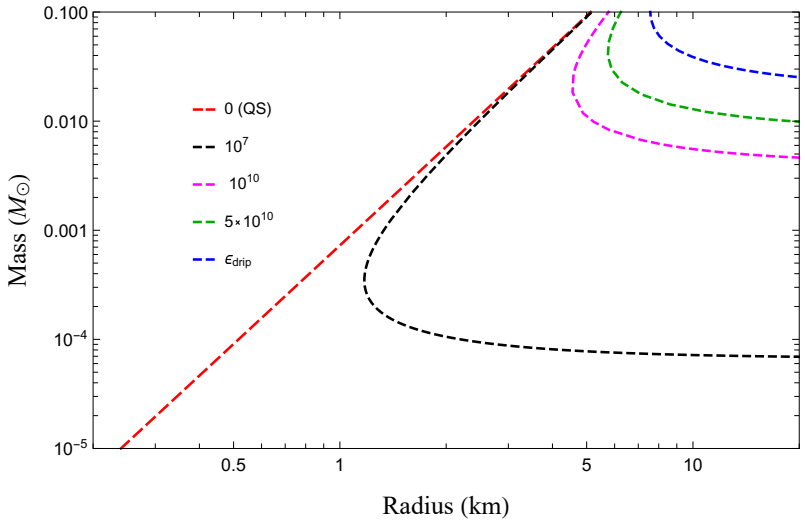

Figure 4.6: A closer look at the low-mass stars in Fig. 4.4. It is evident that when $\varepsilon_{\rm t}$ is low, the deviation from the radius of a SQS is less pronounced.

When we fix $\varepsilon_{\rm t}(P_{\rm t})$, we implicitly let $B_{\rm core}$ vary. Conversely, when we choose to fix the baryon content of the core ($B_{\rm core}$), it is the transition density that changes.

When we establish a fixed value for $B_{\rm core}$, the corresponding configuration contains a specific quantity of quarks in its core. If we start from a point at which $\varepsilon_{\rm t}(P_{\rm t}) = 0$ there is no nuclear matter situated above core to exert compression. In other words, it corresponds to the extreme point on the left side of Fig. 4.2 (red dashed curve) and satisfies Eq. 4.6.

As we increase the central energy density (which means adding matter on top of the quark core), we move in a counter-clockwise direction on the MR diagram. During this progression, we intersect curves in Fig. 4.2 that correspond to increasing values of $\varepsilon_{\rm t}(P_{\rm t})$. This means that a curve representing a constant $B_{\rm core}$ is comprised of configurations with varying $\varepsilon_{\rm t}(P_{\rm t})$. The initial point on this curve has $\varepsilon_{\rm t} = 0$ (or equivalently $\varepsilon_{\rm t}^{\rm Q} = \varepsilon_{\rm W}$), while the final point corresponds to $\varepsilon_{\rm t} = \varepsilon_{\rm drip}$.

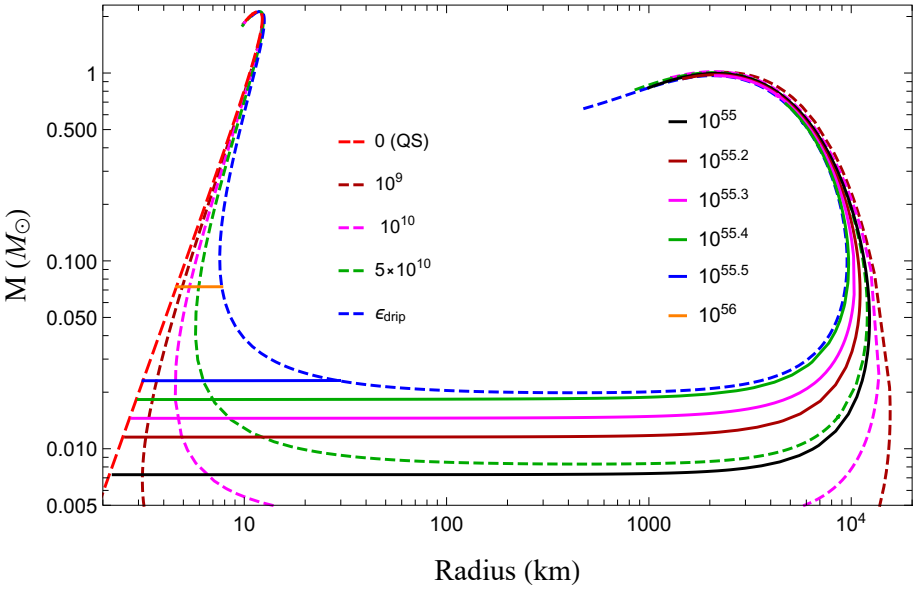

Figure 4.7: MR sequences. Dashed lines show configurations in which P_t is constant. By increasing P_0 (and therefore also $B_{\rm core}$) the curves are followed clockwise. The legend indicates ε_t values in g/cm^3. Solid lines show configurations in which $B_{\rm core}$ is constant. Here, by increasing P_0 (and therefore also P_t) the curves are followed anti-clockwise. The legend indicates the value of $B_{\rm core}$.

In Fig. 4.7, we can observe a specific behavior where, if the value of $B_{\rm core}$ is too large, the condition $\varepsilon_{\rm t} = \varepsilon_{\rm drip}$ is achieved at relatively small radii. These points align precisely with the curve representing the highest density of nuclear matter within the star, which corresponds to the neutron drip density.

4.3 Radial oscillations

To assess the stability of a star, radial oscillations are a valuable analytical tool. The equation for radial oscillations is derived by perturbing both the fluid variables and the spacetime metric that characterizes the interior of the star (Eq. B.9).

Using this metric, the differential equation governing radial oscillations can be expressed as:

$$(H\xi')' = -(\omega^2 W + Q)\xi, \tag{4.10}$$

Here, $\xi(r)$ represents the radial Lagrangian displacement, scaled by r^2 and multiplied by $e^{-\phi}$, while ω is the characteristic frequency of the oscillation mode. The functions in Eq. 4.10 are defined as:

$$
\begin{aligned}
H &= r^{-2}(\varepsilon + P)e^{\lambda+3\phi}c_s^2 \\
Q &= r^{-2}(\varepsilon + P)e^{\lambda+3\phi}(\phi'^2 + 4r^{-1}\phi' - 8\pi e^{2\lambda}P) \\
W &= r^{-2}(\varepsilon + P)e^{3\lambda+\phi}\,,
\end{aligned} \tag{4.11}
$$

Here, c_s^2 represents the speed of sound. It is essential to note that when dealing with multiple layers or phase transitions within the star, it becomes necessary to establish clear boundary conditions at the interfaces between these layers. This aspect is thoroughly discussed in works like Pereira et al. [146] and Di Clemente et al. [147]. In particular, one must specify whether, within the timescale of the oscillation, the two components of the fluid can transition into one another. This consideration hinges on the presence of phase transitions and their associated timescales. Therefore, we categorize these transitions as either "slow transitions" or "fast transitions" to distinguish between their characteristics.

4.3.1 Slow transition

The scenario of a slow phase transition holds when the timescale for the conversion from one phase to another is significantly longer than the timescale of the perturbation itself. In this scenario, the two phases do not intermix during the oscillations, and the volume element near the surface that separates the phases moves along with the interface, expanding and contracting. This particular situation is applicable to SDs where $\varepsilon_{\rm t} < \varepsilon_{\rm drip}$, which essentially means that the two phases never fully mix. In other words, we are considering the stability of star configurations on the MR diagram where $B_{\rm core}$ remains constant, as it cannot increase. In a practical sense, each star configuration can be associated with either a curve characterized by $B_{\rm core}$ or one defined by $P_{\rm t}$ but only one of them is physically acceptable. Consequently, the choice of boundary conditions for radial oscillations must align with this physical interpretation.

For the slow conversion, the interface conditions involve maintaining the continuity of the radial displacement at the boundary radius $r_{\rm t}$:

$$
[\xi]^+_- \equiv \xi(r_{\rm t}^+) - \xi(r_{\rm t}^-) = 0\,, \tag{4.12}
$$

Additionally, it requires ensuring the continuity of the Lagrangian perturbation of pressure:

$$
[\Delta P]^+_- = \left[-e^{\phi}\, r^{-2}\, \gamma(r)\, P\, \frac{\partial \xi}{\partial r}\right]^+_- = 0\,, \tag{4.13}
$$

Here, $\gamma(r)$ represents the relativistic adiabatic index, given by $\gamma(r) = (\partial P/\partial\varepsilon)(\varepsilon + P)P^{-1}$. By solving Eq. 4.10 with these conditions, we obtain that $\omega^2 > 0$, and it vanishes at the maximum mass in the MR plane along the curve defined by the constancy of $B_{\rm core}$, as proposed by the criterion of Zel'dovich [148] and Bardeen et al.

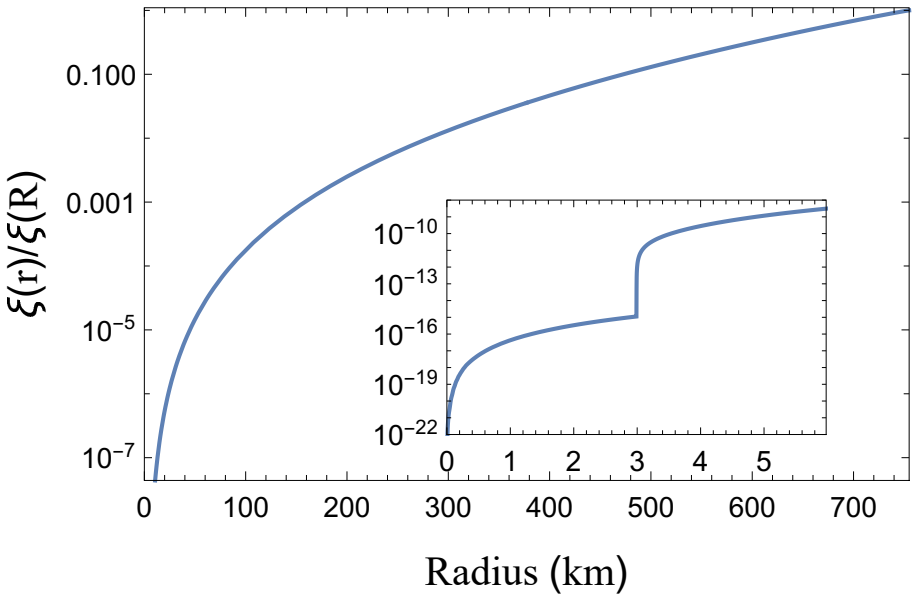

Figure 4.8: Fundamental eigenfunction of radial modes in the slow scenario in which hadrons do not deconfine into quarks during the oscillation timescale. The star considered here and in Fig. 4.9 has $\mathrm{M} \simeq 0.02\,\mathrm{M}_\odot$, $B_{\mathrm{core}} \simeq 2.69 \times 10^{55}$ and $\varepsilon_t = \varepsilon_{\mathrm{drip}}$ and is located to the right of the minimum of the dashed blue curve in Fig. 4.7. Here, the mode is stable: $\omega^2 = 0.788275\,\mathrm{Hz}^2$. In the inset plot, the region around $r = r_t$ is magnified: there the eigenfunction has a kink.

[149]. The eigenfunctions exhibit continuity with a kink at r_{t} (as shown in Fig. 4.8), and the same behavior is reflected in $\Delta P(r)$ [147].

4.3.2 Rapid transition

When the timescale for the conversion between two phases is shorter than the timescale of the perturbation, the exchange of mass between these phases becomes possible. The boundary between these phases is in thermodynamic equilibrium, given the rapid conversion rates, therefore, Eq. 4.13 remains applicable in this scenario.

The main difference compared to the slow transition case lies in the interface condition from Eq. 4.12. In this scenario, it transforms into:

$$\left[\xi + \frac{\gamma P \xi'}{P'}\right]^{+}_{-} = 0\,, \tag{4.14}$$

This modification results in an eigenfunction that exhibits a discontinuity at the interface, distinguishing it from the behavior seen in slow transitions, as visible in Fig. 4.9.

The reason behind the apparent inconsistency between the findings of Glendenning et al. [144, 145] and those of Alford et al. [22] is now evident. In the

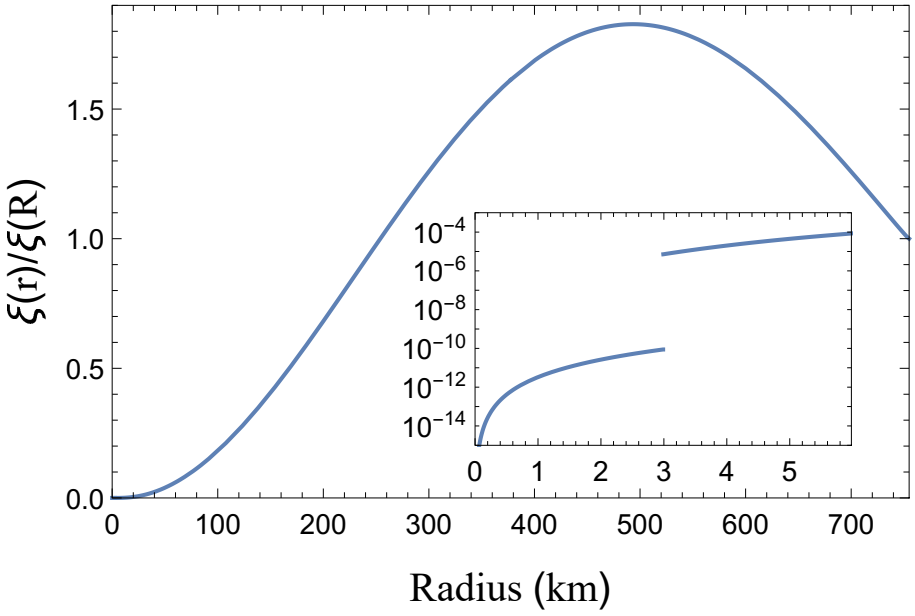

Figure 4.9: The fundamental eigenfunction in the context of rapid transitions, similar to the scenario discussed in Alford et al. [22], but characterized by a discontinuity instead of an extremely abrupt jump (a discontinuity can be seen implies an instantaneous jump). In this case, the mode is unstable, with $\omega^2 = -1.62785/, \mathrm{Hz}^2$, and the eigenfunction displays a discontinuity.

work of Alford et al. [22], they employed an EoS similar to the one discussed in Eq. 4.1. However, they introduced a smoothing mechanism that eliminated the sharp discontinuity between the two phases, and notably, allowed for an instantaneous transformation from one phase to the other for whatever oscillation timescale. The smoothed EoS used in Alford et al. [22] can be described as:

$$\begin{aligned}\varepsilon(P) = &\left[1 - \tanh\left((P - P_{\mathrm{crit}})/\delta P\right)\varepsilon_{\mathrm{tov}}(P)\right]/2 \\ &+ \left[1 + \tanh\left((P - P_{\mathrm{crit}})/\delta P\right)\varepsilon_{\mathrm{quark}}(P)\right]/2\end{aligned} \tag{4.15}$$

Here, δP represents the transition width. This approach is analogous to the rapid transition case discussed here since they are implicitly allowing for a mixed phase. While in Alford et al. [22], the eigenfunction doesn't exhibit a discontinuity at the interface, it experiences a very rapid increase in its value. The magnitude of this increase is entirely equivalent to the magnitude of the discontinuity we obtain, which is illustrated as example in Fig. 4.9.

In contrast, Glendenning et al. [144, 145] did not provide a detailed discussion on the boundary conditions at the interface. However, it is likely that in their work, the eigenfunction was assumed to be continuous, corresponding to the situation described in our "slow" transition scenario.

The distinction between slow and rapid transitions, first introduced in the 1960s

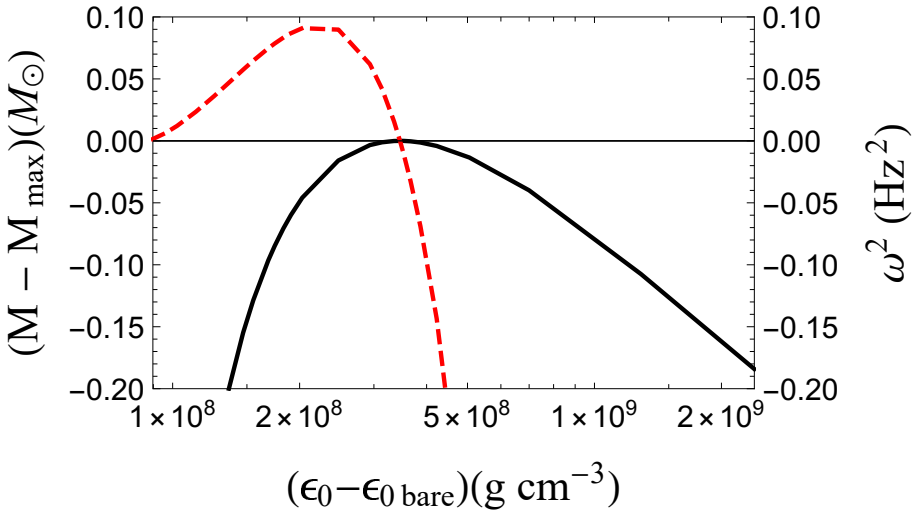

Figure 4.10: Eigenvalues of the fundamental mode in the slow case (dashed) and masses of SDs having $B_{\rm core} = 10^{55}$, close to the maximum, $M_{\rm max} \sim 0.996 M_\odot$ (solid), plotted as functions of the central energy density, ϵ_0. The zero of ω^2 coincides with the maximum mass, and it turns negative at higher densities. Since ϵ_0 remains almost constant in the range displayed in the figure, we show its tiny change with respect to the central density, $\epsilon_{0\ \rm bare}$, of a pure QS that has the same $B_{\rm core}$.

(e.g., Thorne [154]), is based on the observation that the consistency between stability analyses, based on solutions of the TOV equation (static analysis), and those relying on the radial oscillation equation (dynamic analysis), is connected to the use of an adiabatic index derived from the EoS employed in the static analysis. They actually coincide in the case of rapid transitions. In contrast, in slow transitions, it is generally challenging to calculate the adiabatic index, primarily due to the need to account for imbalances introduced by perturbations in the computation of the slow adiabatic index [155, 156].

Our case presents a unique advantage since the conversion between hadrons and quarks is confined to a two-dimensional surface, rather than an extended volume. This simplifies the modification of both the adiabatic index since it corresponds to adapting the interface conditions (Pereira et al. [146]), and the EoS. In the context of the slow case, this means keeping the quark content in a frozen state (Vartanyan et al. [152, 153]). This dual modification allows us to establish a correspondence between static and dynamic analyses in the slow case, a relationship shown in Fig. 4.10. It is worth noting that the correspondence was already established by Alford et al. [22] in the context of the rapid transition case and we reproduced the behavior near the minimum in Fig. 4.11.

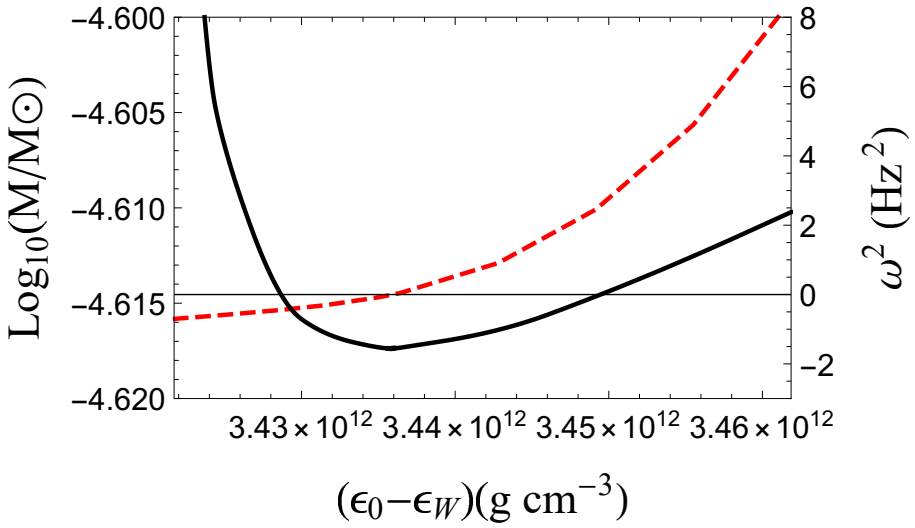

Figure 4.11: Eigenvalues of the fundamental mode in the fast case (dashed) and masses of SDs having $\varepsilon_t = \varepsilon_{\text{drip}}$, close to the minimum (solid), plotted as functions of the difference between the central energy density, ϵ_0 and the Witten one ϵ_{W}. The zero of ω^2 coincides with the minimum mass. This result is consistent with Alford et al. [22]

4.4 SD collapse

In a binary system where a WD orbits a main sequence star, mass transfer occurs as the WD accretes material from its companion. This typical scenario culminates in a type Ia SN event. However, some research has delved into the possibility of a different outcome known as Accretion-Induced Collapse (AIC) within such systems. It is important to note that while the concept of AIC has been explored, actual observations of such events are notably absent. This absence can be attributed to the substantial difference in timescales between the collapse process and the nuclear reactions responsible for igniting the WD's deflagration.

The presence of a core composed of SQM in SDs plays an important role when the object undergoes significant perturbations, such as the initial stages of a type Ia SN event. In particular, if the SQM core is large enough, it can potentially facilitate the collapse of the object instead of following the typical path leading to a deflagration. The challenge in inducing an AIC within a WD arises from the fact the nuclear reactions occur when the star is near the Chandrasekhar limit. This phase, characterized by marginal mechanical stability ($\omega^2 \simeq 0$, then a very long timescale of collapse), leads to the star's disruption before AIC can take place [157].

The mechanical stability of SDs is strictly related to the rapid conversion of hadrons into quarks. This process provides a crucial mechanism that allows the star to undergo a collapse. The presence of a SQM core within SDs introduces a unique dynamic that enables them to deviate from the traditional SN path and experience an AIC event.

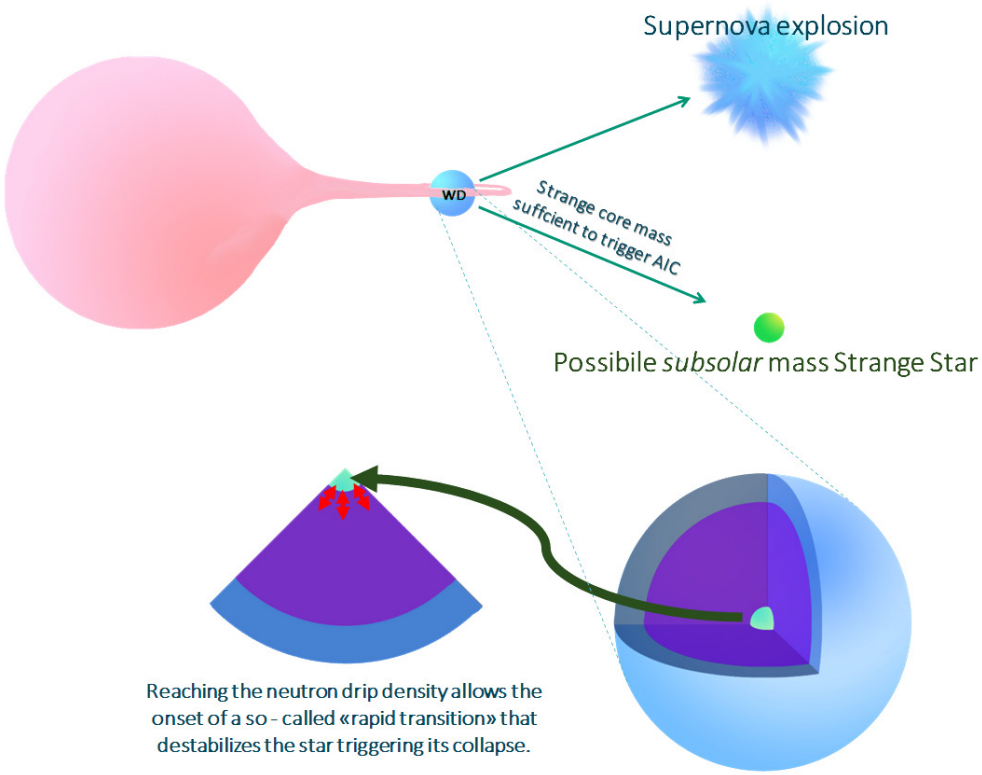

Figure 4.12: Illustration of the AIC mechanism for a system SD-main sequence star.

As long as $\varepsilon_{\rm t} \ll \varepsilon_{\rm drip}$, the object remains mechanically stable. However, if a fluctuation leads to the generation of matter at densities greater than $\varepsilon_{\rm drip}$, the system becomes susceptible to instability. To gauge this instability, we calculate the fundamental eigenvalue of a star at the Chandrasekhar limit along a trajectory where $B_{\rm core}$ remains constant. In the case of a slow transition, ω^2 equals zero. Conversely, in the case of a rapid transition, for the same point, ω^2 is significantly negative. It is important to remark that each point at constant $B_{\rm core}$ corresponds to a point at constant $\varepsilon_{\rm t}$, therefore one can go from a situation in which the transition is physically slow to a situation in which the star internal boundary is in a rapid transition regime and the baryon content of the core is not constant anymore. In any case, it is illogical to apply a slow transition scenario when $\varepsilon_{\rm t}$ remains constant, or to employ a fast transition scenario when $B_{\rm core}$ is held constant. However, exceptions may arise when the star is in close proximity to the Chandrasekhar mass. In such situations, perturbations could potentially drive a small region of the star, located near the strange core, to exceed the neutron drip density. This, in turn, could trigger the phase transition.

Fig. 4.13 displays the e-folding time, defined as $2\pi/|\omega|$. It is evident that there exist a threshold that separates typical SN from AIC. For $B_{\rm core} \gtrsim 10^{46}$, the typical

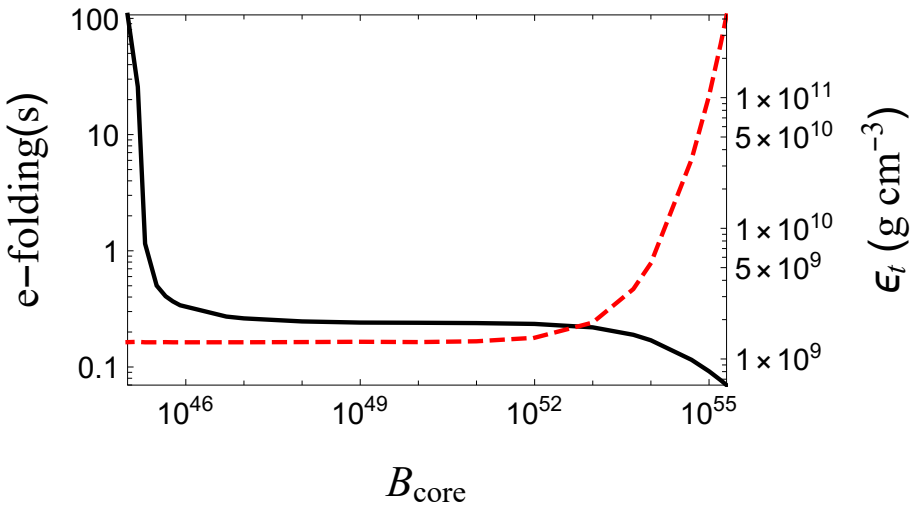

Figure 4.13: Properties of maximum mass stars as a function of their quark content. The solid black line shows the timescale of the mechanical instability as a function of $B_{\rm core}$. The dashed red line shows the transition density.

growth time of the instability falls well below 1 second. This implies that the collapse can transpire more rapidly than the development of a deflagration [158]. It can be argued that the amount of SQM that triggers the collapse depends on the EoS. Therefore, we also computed the e-folding time for a different set of parameters for the quark EoS, as presented in Bombaci et al. [16] and the results remained consistent.

In the same figure, it is represented $\varepsilon_{\rm t}$, the maximum density reached by the nuclear matter component at the boundary. From the behavior of $\varepsilon_{\rm t}$ it is possible to determine when the structure of a 1 $M_\odot$ SD remains similar to the one of a WD. When $B_{\rm core} \gtrsim 10^{52}$ the static structure of the star changes and the boundary density $\varepsilon_{\rm t}$ deviates from $\sim 10^9$ g/cm^3, which is the typical central density of a WD at the Chandrasekhar mass. This suggests that the presence of the quark core does not influence the static properties of the star unless the value of $B_{\rm core}$ is large enough to exert a noticeable gravitational pull.

An essential query regarding SDs pertains to the mechanism by which they accumulate the SQM located at their core. The most straightforward explanation lies in the idea that WDs gradually accumulate strangelets over their lifespan. This phenomenon and the strangelets' genesis is explored in detail in the chapter of this thesis dedicated to the subject of strangelets. Thanks to the AIC mechanism, a SD can convert in a SQS. Since this phenomenon is very energetic and the collapsed object is more bound than a NS, the final object can be a subsolar mass km-sized compact star.

4.5 Other signatures

It has been suggested in Perot et al. [159] that a viable way to observe SDs is via GWs. The paper explores a novel approach to differentiate SDs from WDs, a task that can be challenging through electromagnetic observations alone. It delves into the potential of utilizing gravitational-wave observations to achieve this distinction, specifically by measuring the tidal deformability.

When comparing SDs to WDs, a notable feature is the significant reduction in the tidal deformability coefficient. The distinctiveness in tidal parameters between SDs and WDs holds the potential for detection by upcoming space-based gravitational-wave detectors such as the Laser Interferometer Space Antenna (LISA). The reduction in tidal parameters for SDs can reach up to 50% for an SD with a mass of 0.6 $M_{\odot}$.

In this investigation, the authors opted not to employ the EoS EoS for describing WD structures. Instead, they utilized a more refined EoS that accounts for the precise atomic species and their correct balance within the WDs. The study of SDs involved varying the transition pressure from $P_{\rm t} = P_{\beta}$ (representing the onset of electron capture) to $P_{\rm t} = P_{\rm drip}$.

Additionally, the authors considered the influence of pycnonuclear reactions, which start at a density of 10^{10} g/cm^3 for the carbon layer. Their analysis indicated that the impact of these reactions is minimal on the SD structure. However, they also addressed the issue of crystallized layers in WDs, which proves to be crucial. Crystallization of layers occurs when the WD spans billions of years, rendering the measurement of tidal deformability more challenging.

In Perot and Chamel [160] they delve into the effect of crystalline color superconductor as the phase for the SQM core. The authors observed that the large rigidity of the elastic core has a nearly complete cancellation effect on the tidal deformability, because of the presence of the surrounding hadronic layers. Even though its shear modulus it is 2-3 times larger than the one of the hadronic envelope, the screening effect is almost perfect.

Nevertheless, the study's conclusion emphasizes that the deviation in tidal deformability is larger than the expected precision of future measurements by LISA, suggesting that SDs potentially hidden among WDs binaries could be unmasked through GW observations.

4.5.1 Possible SD observations

It is worth noting that in a study by Kurban et al. [23], seven potential SD candidates were identified. These candidates exhibit a mass range of approximately 0.02 to 0.12 $M_{\odot}$ and have relatively consistent radii, falling within the approximate range of 9000 to 15000 km. To illustrate the incompatibility with WDs models of those candidates, the paper presents MR relationships for WDs using EoSs of pure magnesium (Mg) and helium (He) stars, in addition to the EoS EoS. By employing an EoS for SDs similar to that in Alford et al. [22], it is shown how these objects, due to their

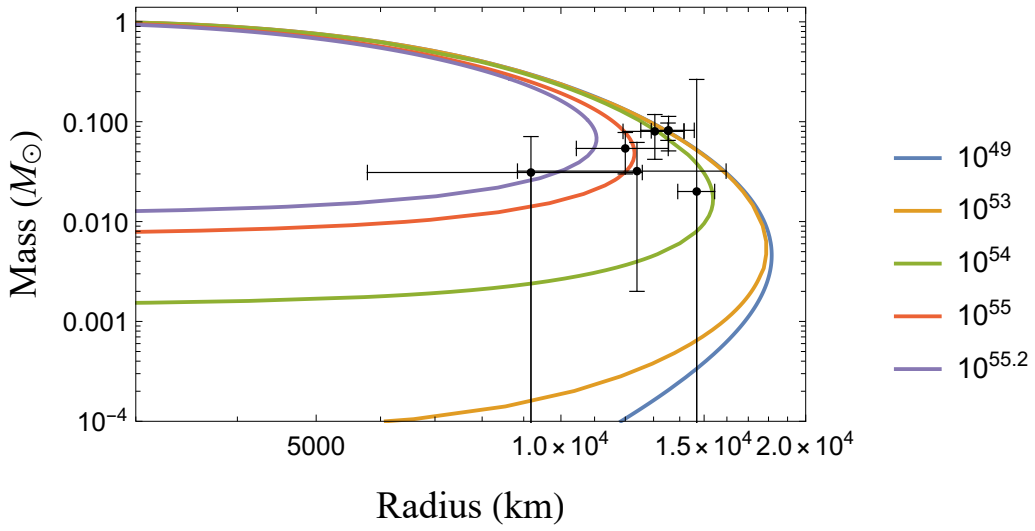

Figure 4.14: Mass-radius relation for constant B_{core} SDs with data from Kurban et al. [23] analysis.

compactness, can be good SD candidates. Moreover, this claim is supported from the fact that the EoS EoS serves as an upper limit for compactness in WDs.

To identify potential SD candidates, the authors analyzed WDs listed in the Montreal WD Database[1]. They employed analyses based on spectroscopic data and Gaia observations [161]. The data points with their error bars corresponding to the objects identified as SD candidates are visible in Fig. 4.14.

[1] http://www.montrealwhitedwarfdatabase.org/tables-and-charts.html

Conclusions

This thesis explores three topics connected with the Bodmer-Witten hypothesis. These topics span astrophysical implications on celestial bodies and cosmological implications on the nature of dark matter, offering insights and proposing future research directions.

1. **Testing the two-Families Scenario in Astrophysics** The first topic addresses one of the astrophysical implications of the Bodmer-Witten hypothesis, particularly the two-families scenario, which posits the coexistence of HSs and SQSs. We proposed a way to test this scenario through BH-NS mergers. For this investigation we used both analytical models and simulations to predict the kilonova signal in such mergers. This is done on the basis of semi-analytical models to estimate the ejected mass. A key finding is the significant suppression of the KN signal in the two-families scenario compared to the one-family scenario. This outcome can be tested with upcoming observations combining GW detections and next-generation telescopes in the optical and infrared bands. Future improvements could involve simulating the BH-NS merger process itself, in order to compute the mass of the ejected material more precisely. Moreover, one could simulate the SQS-BH merger including the effects of a rotating black hole.

2. **Strangelets as Dark Matter** The second and third topics delve into the implications of the Bodmer-Witten hypothesis as formulated by Witten [32] to explain the possible origin of dark matter in the form of strangelets. A simple phenomenological model was developed to examine how the distribution of sizes and masses of strangelets could align with current macroscopic dark matter observational constraints. Additionally, the potential formation of subsolar mass compact stars as an astrophysical consequence of this hypothesis was explored. This study, while providing a proof-of-concept, highlights the need for a deeper understanding of the clusterization mechanism in the early universe. Also the process of evaporation into hadrons needs to be reconsidered in a more precise way, including current QCD knowledge.

3. **Strange Dwarfs and Stability Analysis** The final part of the thesis concentrates on SDs, namely WDs with a core of SQM. The stability of SDs as they approach the Chandrasekhar limit and accrete matter, was studied. This

work highlights how the presence of a SQM core can lead to significantly different evolutionary paths for SDs compared to typical WDs, depending on the core size. Future studies could involve simulating the specific mechanisms of mass ejection during an AIC event, particularly in relation to the critical size of the SQM core.

Overall, while the thesis provides substantial contributions to the understanding of the Bodmer-Witten hypothesis and its astrophysical implications, it also underscores the potential for further research in these areas, particularly through enhanced simulations and the integration of up-to-date theoretical developments in astrophysics and cosmology.

Appendix A

Quantum Chromodynamics

This chapter provides a concise overview of Quantum Chromodynamics (QCD) and effective models for quark matter, with a particular emphasis on strange quark matter. After establishing these fundamental concepts, we delve into the subject of strange matter and its significance in astrophysical contexts. We subsequently explore the characteristics of NSs and strange stars, as well as the equations to determine the static structure of spherically symmetric stars, addressing both Newtonian and general relativistic frameworks. This appendix chapter is based mainly on the works of Buballa [51] and Schwartz [162].

A.1 Quarks and Gluons

QCD is a Quantum Field Theory (QFT) stands as a pillar of the Standard Model of particle physics, delineating the rules and dynamics governing the strong nuclear force. This force is paramount in holding protons, neutrons, and other hadronic particles together. Quarks are elementary particles and a fundamental component of matter. Every hadron, whether it's a proton, neutron, or any other particle from this family, is made up of quarks. There are six distinct types (or "flavors") of quarks: up, down, strange, charm, bottom and top. The most common ones, up and down quarks, form protons and neutrons, the building blocks of atomic nuclei. Quarks have a unique property called "color charge", which is not to be confused with actual colors but is a way to describe the type of charge involved in the strong force. Strong interaction is actually mediated by another particle: the gluon. Gluons, as their name might suggest, are the glue holding quarks together inside hadrons. They are the massless particles responsible for mediating the strong force. Unlike photons in electromagnetism, gluons themselves carry a color charge so they are not neutral in charge. This leads to an intriguing property where gluons can interact not only with quarks but also with other gluons.

In QCD, the concept of "color" charge plays a vital role, analogous to electric charge in electromagnetism. However, unlike electric charge, color charge in QCD has three types, named red, green, and blue. It's essential to note that these names

are purely symbolic and have no relation to actual colors. Quarks always combine in ways to form "white" or color-neutral combinations, leading to the observed confinement of quarks in nature.

A.1.1 Yang-Mills Theory and QCD Interactions

While Quantum Electrodynamics (QED) exemplifies an abelian (or commutative) gauge theory, characterized by a symmetry group $U(1)$, QCD stands as a non-abelian gauge theory with the symmetry group $SU(3)$. Due to its abelian nature, the gauge symmetry of QED is straightforward. In this context, the photon is associated with the gauge field transformation $A_\mu(x) \to A_\mu(x) + \frac{1}{e}\partial_\mu\alpha(x)$, where e is the electric charge. It is possible to describe the photon interaction with matter because of the the interaction itself preserve the gauge invariance. The interaction term expressed within QED takes the form $\bar{\psi}\gamma^\mu D_\mu\psi$, where the covariant derivative D_μ encapsulates the underlying physics of the interaction: $D_\mu\psi = (\partial_\mu - ieA_\mu)\psi$. In these expressions, ψ represents the fermions field, and $\bar{\psi}$ is its conjugate.

The covariant derivative D_μ incorporates both the spacetime derivative ∂_μ and the interaction with the electromagnetic force through the gauge field A_μ.

The framework of Yang-Mills theories provides a way to extend the principles of QED to a broader context. This extension allows for the inclusion of self-interactions among massless particles with spin 1, such as gluons. These self-interactions are renormalizable, which means that the theory can be consistently treated in a way that avoids infinite or non-physical results arising from certain calculations.

Therefore, the QCD interaction term encompasses the strong force's interaction between quarks through the gluon-mediated exchange of color charge. This approach finds its foundation in Yang-Mills theories which enable the study of renormalizable self-interactions among massless particles with spin 1.

Yang-Mills Foundations

Yang and Mills generalized the concept of gauge invariance, known from electromagnetism, to non-abelian groups. The Lagrangian for a Yang-Mills field A^a_μ with a general gauge group is:

$$\mathcal{L}_{YM} = -\frac{1}{4}F^a_{\mu\nu}F^{\mu\nu a} \tag{A.1}$$

where $F^a_{\mu\nu}$ is the field strength tensor, typically involving commutators of gauge fields, reflecting the non-abelian nature. It is given by:

$$F^a_{\mu\nu} = \partial_\mu A^a_\nu - \partial_\nu A^a_\mu + g f^{abc} A^b_\mu A^c_\nu \tag{A.2}$$

with f^{abc} being the structure constants of SU(3). These constants arise from the commutation relations:

$$[T^a, T^b] = i f^{abc} T^c \tag{A.3}$$

where T^a are the generators (matrices) of the SU(3) group. The generators are usually written in the standard form $T^a = \frac{1}{2}\lambda^a$, where λ^a are the Gell-Mann matrices:

$$\lambda^1 = \begin{pmatrix} 0 & 1 & 0 \\ 1 & 0 & 0 \\ 0 & 0 & 0 \end{pmatrix}, \qquad \lambda^2 = \begin{pmatrix} 0 & -i & 0 \\ i & 0 & 0 \\ 0 & 0 & 0 \end{pmatrix},$$
$$\lambda^3 = \begin{pmatrix} 1 & 0 & 0 \\ 0 & -1 & 0 \\ 0 & 0 & 0 \end{pmatrix}, \qquad \lambda^4 = \begin{pmatrix} 0 & 0 & 1 \\ 0 & 0 & 0 \\ 1 & 0 & 0 \end{pmatrix},$$
$$\lambda^5 = \begin{pmatrix} 0 & 0 & -i \\ 0 & 0 & 0 \\ i & 0 & 0 \end{pmatrix}, \qquad \lambda^6 = \begin{pmatrix} 0 & 0 & 0 \\ 0 & 0 & 1 \\ 0 & 1 & 0 \end{pmatrix},$$
$$\lambda^7 = \begin{pmatrix} 0 & 0 & 0 \\ 0 & 0 & -i \\ 0 & i & 0 \end{pmatrix}, \qquad \lambda^8 = \frac{1}{\sqrt{3}} \begin{pmatrix} 1 & 0 & 0 \\ 0 & 1 & 0 \\ 0 & 0 & -2 \end{pmatrix}.$$

Gluons, denoted by A^a_μ where $a = 1, ..., 8$, carry a color charge. This leads to unique self-interactions:

$$\mathcal{L}_{\text{int}} = g f^{abc} (\partial_\mu A^a_\nu - \partial_\nu A^a_\mu) A^{\mu b} A^{\nu c} \tag{A.4}$$

showing direct three-gluon interactions, a consequence of the non-abelian nature of SU(3).

Quarks possess a color charge and are represented by Dirac spinors q with suppressed indices. Their dynamics is described by:

$$\mathcal{L}_q = \bar{q}(i\gamma^\mu D_\mu - m)q \tag{A.5}$$

where now the covariant derivative reads

$$D_\mu = \partial_\mu - igT^a A^a_\mu \tag{A.6}$$

which ensures gauge invariance. Quark interactions conserve color charge, depicted by vertices in Feynman diagrams where quarks change color upon emitting or absorbing a gluon.

Implications of Non-abelian Nature

The interactions in QCD are non-linear due to the terms involving commutators of gauge fields. This leads to phenomena like confinement and asymptotic freedom. In addition to quark-quark-gluon vertices, there exist gluon-gluon-gluon and gluon-gluon-gluon-gluon vertices, a direct consequence of the non-abelian structure (Fig. A.1).

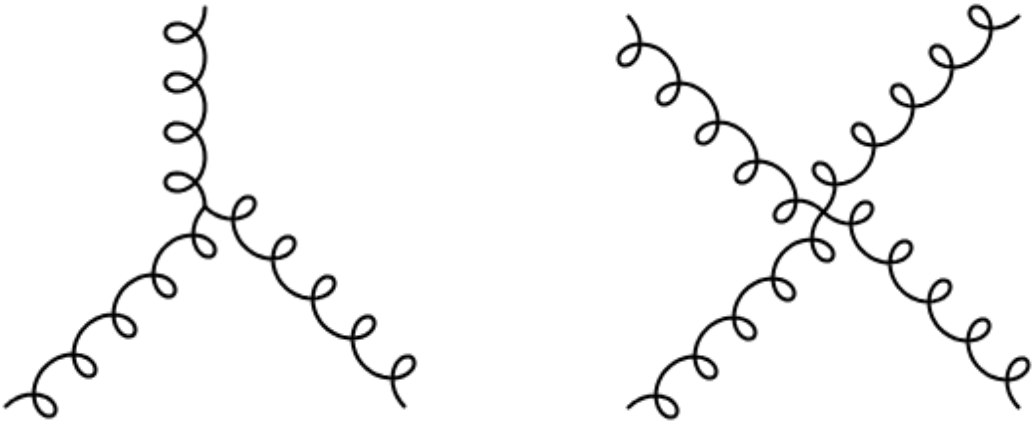

Figure A.1: 3-gluons vertex and 4-gluons vertex

A.1.2 Confinement

Confinement is a quintessential aspect of QCD because despite our understanding of quarks and gluons as the fundamental building blocks of hadrons, we never observe these particles in isolation. Instead, they are always *confined* within larger composite particles like protons, neutrons, and mesons.

Given the substantial evidence for the existence of quarks, ranging from deep inelastic scattering experiments to the observed patterns of particle resonances, it's perplexing that we never directly observe free quarks. When we attempt to isolate individual quarks by pulling them apart, the energy required to achieve this separation seems to increase without bound. This phenomenon is known as the "confinement" of quarks. The energy stored in the color field that binds quarks together increases as they are pulled apart, eventually reaching a point where it's more favorable to create new quark-antiquark pairs from the vacuum, forming new hadrons rather than allowing the isolation of individual quarks.

Furthermore, the concept of the running coupling constant is intimately linked to confinement in QCD. The coupling constant is a measure of the strength of the interaction between quarks and gluons. A QFT formulated using a Lagrangian approach inherently adopts a perturbative method for its solutions. This perturbative method is indeed applicable when the interaction coupling is small. When determining scattering cross sections within QFT, the renormalization procedure, following loops resummation, results in defining a coupling constant g that is energy-dependent. Specifically, g varies with the scale μ due to the renormalization of the theory, symbolized as $g \mapsto g(\mu)$. The main quantity derived from perturbative QCD is the *beta-function* (β-function). The latter is related to the running coupling constant by the differential equation

$$\beta(g) = \mu \frac{\partial g}{\partial \mu} \tag{A.7}$$

The β-function in at one-loop level, reads:

$$\beta(g) = \frac{11N_c - 2N_f}{48\pi^2} g^3. \tag{A.8}$$

By solving Eq. A.7 and Eq. A.8 one obtain the running coupling constant expression:

$$g^2(\mu) = \frac{g_*^2}{1 + 2bg_*^2 log\frac{\mu}{\mu_*}} \tag{A.9}$$

where μ_* indicates the reference energy scale at which $g_* = g(\mu_*)$. At short distances, quarks and gluons behave nearly like free particles, and the coupling constant is relatively small. At larger distances where confinement becomes significant, the coupling constant increases, rendering perturbative methods ineffective. This phenomenon, known as asymptotic freedom, explains why QCD interactions become weaker at high energies, a counterintuitive behavior compared to other forces. Indeed this feature is shared by non-abelian gauge theories.

A.2 Structure of the Vacuum in QCD

The vacuum in QCD is far from being an empty and inert entity. Instead, it is a complex medium characterized by non-perturbative effects and is associated with numerous condensates, revealing the rich and intricate structure of the QCD ground state.

The chiral condensate is one of the most fundamental vacuum expectation values in QCD and is intimately linked to the spontaneous breaking of chiral symmetry. In the world of QCD, where quarks are massless or nearly so, there exists a chiral symmetry. However, this symmetry is not realized in nature, meaning it is spontaneously broken. This breaking is signaled by a non-zero value of the chiral condensate:

$$\langle \bar{q}q \rangle \neq 0$$

where q represents the quark field. The non-zero value indicates that the QCD vacuum acts as a medium in which quark-antiquark pairs are constantly being created and annihilated, leading to the observed broken symmetry. This spontaneous breaking of chiral symmetry, and its associated condensate, is crucial as it gives rise to the mass of hadrons.

A.2.1 Quark Current Mass and Constituent Mass

Understanding the origin of the mass of nucleons, such as neutrons and protons, is central to particle physics. The initial assumption might be that the Higgs mechanism is the primary source of all particle masses, but there's more depth to this story.

In the Standard Model (SM) of particle physics, the Higgs mechanism is fundamental for endowing the gauge bosons with mass, except for the photon and gluon. This is realized via a symmetry-breaking process. Specifically:

$$\mathrm{SU}(3)_c \otimes (\mathrm{SU}(2)_L \otimes \mathrm{U}(1)_Y) \rightarrow \mathrm{SU}(3)_c \otimes \mathrm{U}(1)_Q \tag{A.10}$$

The left-hand side of the equation represents the combined symmetries before breaking. Post breaking, three generators of $\mathrm{SU}(2)_L$ are disrupted, producing three Goldstone bosons. These bosons, being massless, are "eaten up" by gauge bosons, giving them mass. This process is essential as directly assigning mass to these gauge bosons would violate the principle of gauge invariance.

For SM fermions, the way of acquiring mass is distinct. Instead of the mechanism used by gauge bosons, fermions interact directly with the Higgs field via the Yukawa coupling. In the Lagrangian, this reads as:

$$\mathcal{L}_{\text{Fermions}}(\phi, A, q) = \overline{\psi}\gamma^\mu D_\mu \psi + G_\psi \overline{\psi}\phi\psi \tag{A.11}$$

In this equation, ϕ denotes the Higgs field, while q refers to the fermion fields. Quarks, for instance, have been experimentally determined to possess masses around 5 MeV for the up and down varieties. An interesting point arises: why does a nucleon, constituted of quarks, exhibit a mass approximately 200 times greater than an individual quark? The answer revolves around chiral symmetry breaking.

Chiral symmetry breaking illuminates why entities like neutrons and protons exhibit such significant mass compared to the elementary quarks that constitute them. In a scenario where the masses of specific quarks tend towards zero, the QCD lagrangian showcases invariance under a chiral transformation. This symmetry breaking is characterized by the chiral condensate's non-zero vacuum expectation value, represented as:

$$\langle \bar{q}_R^a q_L^b \rangle = v\delta^{ab} \tag{A.12}$$

When particles are conceptualized using a two-quark model, a symmetry is observed:

$$\mathrm{SU}(2)_L \otimes \mathrm{SU}(2)_R \otimes \mathrm{U}(1)_V \otimes \mathrm{U}(1)_A \tag{A.13}$$

However, because of strong interaction, this chiral symmetry is reduced to:

$$\mathrm{SU}(2)_L \otimes \mathrm{SU}(2)_R \rightarrow \mathrm{SU}(2)_V \tag{A.14}$$

Here, the resultant framework yields three Goldstone bosons, known as pions. Though these pions are visualized as rotations about an equilibrium state and should ideally

be devoid of mass, they indeed possess some mass. This is attributed to the explicit symmetry breaking instigated by non-zero quark masses. Extending this perspective to a three-quark model elucidates the masses of various mesons, inclusive of protons and neutrons, as they are influenced by the QCD vacuum condensate. Therefore, chiral symmetry is a fundamental symmetry of the QCD Lagrangian when quarks are massless. The chiral condensate in Eq. A.12 is a measure of quark-antiquark pairs in the vacuum. A non-zero value for this condensate indicates that chiral symmetry is spontaneously broken in the QCD vacuum. This spontaneous breaking is closely related to quarks acquiring a constituent mass:

$$M_q \approx -\frac{\langle \bar{q}q \rangle}{f_\pi^2} \tag{A.15}$$

where M_q is the constituent quark mass and f_π is the pion decay constant.

To sum it up, the very presence of a non-zero current quark mass in the Lagrangian (however small it might be for light quarks) leads to an explicit breaking of chiral symmetry. The pion, a meson consisting of a quark and an antiquark, serves as an example. While the current masses of its constituent quarks are minimal, the mass of the pion itself isn't zero. This mass arises from both spontaneous and explicit chiral symmetry breaking.

In essence, the constituent mass of quarks emerges from their interactions within the QCD medium, profoundly influenced by the interplay of chiral symmetry and its breaking mechanisms.

A.3 Models for high Density QCD

High-energy QCD can be studied in terrestrial laboratories using particle accelerators. The behavior of the QCD coupling constant allows for predictions of experimental results through perturbation theory. However, at low energies, it becomes unfeasible to perturbatively analyze the QCD Lagrangian. In such scenarios, effective theories become crucial for our understanding.

Beyond the high-energy regime, there exists another extreme regime that remains elusive to terrestrial laboratory studies: the high-density regime. Some stars, at the end of their evolutionary cycle, achieve densities comparable to nucleons. In such extreme environments, unique nuclear properties of matter emerge. Due to our inability to replicate such immense densities in macroscopic scales on Earth, it becomes essential to study NSs and other potential exotic objects to gain a comprehensive understanding of QCD.

Compact stars, despite their immense gravitational pull and density, are relatively cold objects. Their low-temperature nature makes them distinct from other high-energy phenomena. However, to glean insights into the intermediate-density regime, which might bridge our understanding between various energy states, one can use heavy-ion collision experiments.

These controlled collisions offer a unique window into the behavior of dense matter. In particular, they shed light on the conditions under which new degrees of freedom, such as quark-gluon plasma, might manifest, especially as the system approaches high temperatures. Such transitions and phenomena are crucial, as they give hints about the underlying properties and phases of QCD at varying densities and temperatures.

Given the wealth of data and observations from these experiments, some researchers have proposed that they can be used as a foundation to extrapolate and infer the behavior of cold NS matter. While there's a temperature disparity between compact stars and heavy-ion collision experiments, the underlying physics, especially pertaining to density and quantum interactions, might have shared characteristics. Hence, by understanding one system, we might be better positioned to make educated predictions about the other.

In order to describe hadrons and consequently high density QCD, namely bunch of quarks together, several models have been considered during history. From the simpler MIT bag model to the more complex Nambu-Jona-Lasinio (NJL) model.

A.4 Nambu–Jona-Lasinio (NJL) Model

A.4.1 Introduction

The Nambu-Jona-Lasinio (NJL) Model is a theoretical framework delved to undestand some aspect of QCD. It was first formulated by Nambu and Jona-Lasinio [163] in 1961 [164]. In the NJL model, quarks are treated as point-like particles, and their interactions are described by a four-fermion interaction term. This local interaction can be seen as an approximation to the effects of gluon exchanges. This model has proven invaluable for probing processes such as chiral symmetry breaking and hadron formation. Though the NJL model can capture some of the low-energy characteristics of QCD, it doesn't offer a comprehensive description of strong interactions. Indeed, as a low-energy effective theory, the NJL model captures the essential features of chiral symmetry breaking in QCD despite not incorporating confinement, a key aspect to treat phase transitions in self bound objects such as strange stars.

Even though it lacks gluonic degrees of freedom and does not provide a description of confinement, the NJL model has been successful in describing the dynamical chiral symmetry breaking and the hadronic spectra, especially in the light quark sector.

A.4.2 Two-Flavor Quark Matter in the NJL Model

For two-flavor quark matter, the NJL model focuses on up (u) and down (d) quarks. The Lagrangian density, incorporating a local four-quark interaction, is given by:

$$\mathcal{L}_{\text{NJL}} = \bar{\psi}(i\gamma^\mu \partial_\mu - m_0)\psi + G[(\bar{\psi}\psi)^2 + (\bar{\psi} i\gamma_5 \vec{\tau}\psi)^2] \tag{A.16}$$

Here, ψ represents the quark field doublet $(u, d)^T$. The Dirac matrices are represented by γ^μ, and m_0 is the current quark mass matrix, usually taken as a diagonal matrix $m_0 = \text{diag}(m_u, m_d)$. The parameter G denotes the coupling constant tied to the strength of the four-quark interaction, and $\vec{\tau}$ are the Pauli matrices that operate in flavor space.

The dynamical breaking of chiral symmetry is attributed to the four-quark interaction term in the Lagrangian. Although the scalar and pseudoscalar interactions are the primary components, the NJL model can also accommodate other interaction channels such as vector and axial-vector.

To study the spontaneous breaking of chiral symmetry, we use a mean-field approximation. By considering the quark bilinear $\bar{\psi}\psi$ as approximating its vacuum expectation value $\langle\bar{\psi}\psi\rangle$, we can derive the gap equation. This is achieved by differentiating the thermodynamic potential with respect to the quark bilinear, setting the resulting expression to zero, thus obtaining the equation that determines the dynamically generated quark mass.

Formally, the (mass) gap equation is given by:

$$M_i = m_i - 2G\langle\bar{\psi}_i\psi_i\rangle \tag{A.17}$$

Here, M_i represents the dynamically generated (or constituent) mass for the quark flavor i, and $\langle\bar{\psi}_i\psi_i\rangle$ is the quark condensate for the flavour i. The quark condensate:

$$\langle\bar{\psi}_i\psi_i\rangle = -\frac{3}{\pi^2}\int_{k_{\text{F},i}}^{\Lambda} p^2 \frac{m_i}{\sqrt{m_i^2 + p^2}} dp \tag{A.18}$$

where Λ is the cutoff to regularize the integral and $k_{\text{F},i}$ is the fermi momentum of the i quark that is

$$k_{\text{F},i} = (\pi^2 n_i)^{\frac{1}{3}} \tag{A.19}$$

Through this two-flavor NJL model, it becomes possible to determine various physical observables. For instance, one can compute the pion decay constant and the quark condensate, both vital for a deeper understanding of low-energy QCD phenomena.

A.4.3 Three-Flavor Quark Matter in the NJL Model

For the case of three-flavor quark matter, the NJL model involves up (u), down (d), and strange (s) quarks. Expanding the previous discussion, the Lagrangian density for the three-flavor model is in its most common form is given by:

$$\mathcal{L}_{\text{NJL,3f}} = \bar{\psi}(i\gamma^\mu \partial_\mu - m_0)\psi + \mathcal{L}_{sym} + \mathcal{L}_{\text{'t Hooft}} \tag{A.20}$$

where $\mathcal{L}_{sym}$ and $\mathcal{L}_{det}$ are two independent interaction terms. Their explicit form reads

$$\mathcal{L}_{\text{sym}} = G[(\bar{\psi}\psi)^2 + (\bar{\psi}i\gamma_5\lambda_a\psi)^2] \tag{A.21}$$

and

$$\mathcal{L}_{\text{'t Hooft}} = -K\left[\det{}_f(\bar{\psi}(1+\gamma_5)\psi) + \det{}_f(\bar{\psi}(1-\gamma_5)\psi)\right] \tag{A.22}$$

In these equations ψ is now the quark field triplet: $\psi = (u, d, s)^T$, the current quark mass m_0, extends to $m_0 = \text{diag}(m_u, m_d, m_s)$, λ_a are the Gell-Mann matrices acting in flavor space, extending the role of the Pauli matrices from the two-flavor case, while G and K are coupling constants representing interactions among the quarks.

$\mathcal{L}_{sym}$ is a symmetric 4-point interaction $U(N_f)_L \times U(N_f)_R$ while $\mathcal{L}_{\text{'t Hooft}}$ is the 't Hooft interaction and it is a determinant in the flavour space. The 't Hooft term is $SU(N_f)_L \times SU(N_f)_R$ symmetric but it is needed to account the $U_A(1)$ anomaly which arises from the gluon sector. Moreover, this term is phenomenologically important to get the correct η' mass: in the chiral limit in which $m_u = m_d = m_s = 0$ the meson η is massless while the meson η' has a finite mass due to the $\mathcal{L}_{\text{'t Hooft}}$.

The extension to three flavors allows us to account for the strange quark and its influence on chiral symmetry breaking. By applying the mean-field approximation similarly as in the two-flavor case, we can treat quark bilinears like $\bar{\psi}\psi$ as their vacuum expectation values, which results in a set of gap equations. Each equation determines the dynamically generated mass for the respective quark flavor. Formally, for each quark flavor i, the gap equation takes the form:

$$M_i = m_i - 4G\langle\bar{\psi}_i\psi_i\rangle + 2K\langle\bar{\psi}_j\psi_j\rangle\langle\bar{\psi}_k\psi_k\rangle \tag{A.23}$$

where i, j, and k are distinct and represent any of the u, d, or s quarks.

By solving these gap equations self-consistently, we can determine the constituent quark masses, which are influenced by the chiral dynamics and interactions among the three quarks.

The three-flavor NJL model provides a framework to study not only the chiral dynamics and symmetry breaking patterns influenced by the strange quark but also to calculate relevant physical observables like meson masses and decay constants.

A.5 Equations of state of quark matter

When we study strange quark star or agglomerate of strange quark matter in general, such as quark nuggets, we have to rely on EoS. Whitin the framework of the MIT bag model or the NJL model, we can define relations between pressure and energy density of quarks, by calculating from the lagrangian formulation the thermodynamic potential and then deriving quantities such pressure and energy density.

A.6 MIT bag model EoS

The MIT Bag Model [48], developed in the 1970s at the Massachusetts Institute of Technology, offers a theoretical framework to understand the behavior of quarks within hadrons. This model conceptualizes quarks as free-moving particles inside a hypothetical spherical "bag". The bag serves as a confinement boundary, delineating a region where quarks can exist freely. Beyond this boundary, the strong force prevents quarks from existing as isolated entities. This confinement is captured by a balance between the internal pressure of the quark-gluon gas and the external vacuum pressure. In other words the bag constant is a measure of the energy density difference between the perturbative and non-perturbative QCD vacuums.

Inside this bag, quarks are imagined to move as though they are non-interacting, a simplifying approximation given that quarks actually do interact via the strong force. To characterize the model further, a "bag constant," denoted as B, is introduced. This constant represents the energy density difference between the true vacuum outside and the perturbative vacuum inside the bag.

To ensure quarks remain inside this confinement boundary, the model requires quark fields to vanish at the bag's surface. While the MIT Bag Model has found applications in predicting hadron properties and probing the behavior of dense quark matter, it's essential to recognize its limitations. As a simplified representation, it doesn't fully capture the intricate dynamics of QCD, especially over short distances.

Within the MIT bag model, we can express the total energy of a bulk of i deconfined quark flavours as:

$$\varepsilon = \sum_i \varepsilon_i + B \tag{A.24}$$

where B is the bag constant.

The energy density of the single flavour i reads [165]:

$$\begin{aligned}\varepsilon_i(\rho_i) = &\frac{3{m_i}^4}{8\pi^2}\left[x_i\left(2x_i^2+1\right)\left(\sqrt{1+x_i^2}\right) - \operatorname{arcsinh} x_i\right] \\ &-\alpha_s\frac{{m_i}^4}{\pi^3}\left[x_i^4 - \frac{3}{2}\left[x_i\left(\sqrt{1+x_i^2}\right) - \operatorname{arcsinh} x_i\right]^2\right],\end{aligned} \tag{A.25}$$

The QCD coupling constant is denoted by α_s, while the quantity x_i is defined as

$$x_i = \frac{k_{\mathrm{F},i}}{m_i}, \tag{A.26}$$

where $k_{\mathrm{f}i}$ is the Fermi momentum for flavor i defined in Eq. A.19

One notable form of the bag model which is useful when describing SQS is a parametrization that aim to phenomenologically reproduce the quark matter behaviour accounting for some QCD corrections. The thermodynamic potential Ω reads [60]:

$$\Omega = -\frac{3}{4\pi^2}a_4\mu^4 + \frac{3}{4\pi^2}a_2\mu^2 + B_{eff}, \tag{A.27}$$

where $a_4 \equiv 1-c$ represents the QCD corrections to the pressure of the free-quark Fermi sea, and a_2 accounts for effects related to quark pairing and the mass of strange quarks. The term B_{eff} is the effective bag constant, which may be density-dependent and can depend on a_4 and a_2.

A.6.1 NJL model EoS

The NJL model does not have a proper bag as the MIT bag model. Using the mean field approximation we have to stabilize the solution by artificially reducing the energy density and pressure in the vacuum. This is done by defining a parameter analogous to the bag constant in the MIT bag model [166, 51]

$$B = \sum_{i=u,d,s}\left(\frac{3}{\pi^2}\int_0^{\Lambda} p^2 dp\left(\sqrt{p^2+M_i^2}-\sqrt{p^2+{m_i}^2}\right) - 2G\left\langle\bar{q}_i q_i\right\rangle^2\right) + 4K\left\langle\bar{u}u\right\rangle\left\langle\bar{d}d\right\rangle\left\langle\bar{s}s\right\rangle \tag{A.28}$$

The equation of state for SQM in the NJL model can be derived as

$$P = -\varepsilon + \sum_{i=u,d,s} n_i\sqrt{k_{\mathrm{F},i}^2+m_i^2}, \tag{A.29}$$

with the energy density given by

$$\varepsilon = \sum_{i=u,d,s}\frac{3}{\pi^2}\int_0^{k_{\mathrm{F},i}} p^2 dp\sqrt{p^2+M_i^2} - (B-B_0). \tag{A.30}$$

Buballa and Oertel [166] justifies the bag pressure B as a quantity which dynamically emerges from the mean field solution, contrasting with the MIT bag model where it is introduced externally. In the NJL approach we obtain a dynamic mass at non-zero baryon densities, differing from the MIT bag model, which maintains a constant mass across densities. This results is a direct consequence of chiral symmetry breaking.

The vacuum treatment between models is very different: the MIT bag model assumes a particle-free vacuum with particle wave function flow confined, whereas the NJL model lacks such confinement, since the vacuum consists of paired quasi-quarks that lower particle energy density in comparison to the MIT model. For this reason when we use EoS derived from NJL model, we add an effective bag constant

$$B_0 = B|_{n_u=n_d=n_s=0}, \tag{A.31}$$

$$B_{\text{eff}} = B - B_0. \tag{A.32}$$

Appendix B

Hydrostatic of a compact star

B.1 Stellar structure equations

B.1.1 Newtonian structure equations

After having introduced the EoS we have to describe what a compact star structure looks like. To do so, we have to introduce equations that describe the hydrostatic equilibrium. In particular, the overall structure of a star emerges as a consequence of a delicate balance between dominant forces, notably the force of gravity and the opposing effect of hydrostatic pressure. When considering the situation in which the Newtonian framework is applicable and considering the spherically symmetrical case, it becomes possible to address the issue using straightforward equations. In the process of formulating the equations that describe the star's structure, a key requirement is to compute the tiny force resulting from the pressure acting on a small spherical shell with a radius r,

$$dF_P = dP\, 4\pi r^2, \tag{B.1}$$

together with the infinitesimal gravitational force to which the shell of radius r is subjected and thickness dr, namely

$$dF_g = -\frac{Gm(r)}{r^2} 4\pi r^2 \varrho dr. \tag{B.2}$$

The hydrostatic equilibrium in a fluid is described by these two equations in the form

$$\nabla P = -\varrho \nabla \Phi\,, \tag{B.3}$$

where ϱ is the density meanwhile $\Phi = -\frac{Gm(r)}{r}$ represents the gravitational potential.

The spherical symmetric form of Eq. B.3 reads:

$$\frac{1}{\varrho}\frac{dP(r)}{dr} = -\frac{Gm(r)}{r^2}\,. \tag{B.4}$$

To proceed, we need to relate the enclosed mass $m(r)$ to the density $\varrho(r)$. This is achieved through the conservation of mass equation for the spherical object:

$$dm = 4\pi r^2 \varrho(r) dr \,. \tag{B.5}$$

This set of equations achieves closure upon the incorporation of the EoS. In the context of the barotropic approximation, this equation is represented as:

$$P \equiv P(\varrho). \tag{B.6}$$

Here, pressure is explicitly defined as a function of density, thereby rendering the system of equations self-sufficient and self-consistent.

Actually, the EoS might explicitly exhibit dependence on temperature, necessitating the incorporation of additional equations to achieve closure within the system. The latter would make explicit the variation of temperature in terms of energy transport mechanisms and the star's energy balance.

Nevertheless in the simplest case here considered, the integration process necessitates adherence to specific boundary conditions, which can be expressed in terms of both mass and radius, where $r(M) = R$ and $m(R) = M$. These conditions dictate that the density at the stellar core assumes a finite value $\varrho_{\rm cent}$:

$$\varrho(0) = \varrho_{\rm cent} \quad ,$$

Furthermore, the pressure must vanish at the surface of the star:

$$P(R) = 0 \quad .$$

An additional condition can be established concerning the pressure's derivative at the core of the star. This arises due to the behavior of central mass for small radii:

$$m(r) \approx \varrho_{\rm cent} \frac{4\pi}{3} r^3 \quad . \tag{B.7}$$

By combining the aforementioned equation with Eq. B.4, the condition at the center is expressed as:

$$\left.\frac{dP}{dr}\right|_{r=0} \approx -\left.\frac{4\pi}{3} G \varrho_{\rm cent} r\right|_{r=0} = 0. \tag{B.8}$$

B.1.2 Tolman-Oppenheimer-Volkoff equation (TOV)

The Newtonian hydrostatic equations provide a useful framework for describing the internal structure and equilibrium of conventional celestial objects like stars, planets, and white dwarfs. These equations help us analyze the balance between gravitational forces and pressure gradients within these bodies, shedding light on their overall physical makeup and properties.

However, when dealing with highly dense and compact stellar objects like NSs, the simplifications of the Newtonian framework fall short. In such extreme conditions, the effects of spacetime curvature, as outlined by Einstein's general theory of relativity, come into play. The intense gravitational fields generated by the high mass densities cause significant warping of spacetime, resulting in phenomena where the relativistic nature of gravity becomes significant.

As a result, a more sophisticated approach is required to accurately model NSs and similar compact objects. General relativity offers a more comprehensive understanding of the gravitational interaction by considering the interrelation between mass, energy, and spacetime geometry.

Therefore, TOV equation is the generalization of Newtonian hydrostatic equilibrium, namely a fundamental result in theoretical astrophysics, describing the equilibrium structure of spherically symmetric, self-gravitating objects. As in the Newtonian case, this equation arises from the application of the hydrostatic equilibrium condition, which balances the gravitational force inward with the pressure force outward.

Indeed, in the case of a spherically symmetric, static and isotropic star, the most general way to describe the spacetime's structure using spherical coordinates is by employing the following equation:

$$ds^2 = -e^{2\phi(r)}dt^2 + e^{2\lambda(r)}dr^2 + r^2 + r^2\left(d\theta^2 + \sin^2\theta d\phi^2\right) . \tag{B.9}$$

By considering the relation between the line element and the metric tensor,

$$d\tau^2 = g_{\mu\nu}dx^\mu dx^\nu , \tag{B.10}$$

one finds the form of the metric tensor itself:

$$g_{\mu\nu} = \begin{pmatrix} -e^{2\nu(r)} & 0 & 0 & 0 \\ 0 & e^{2\lambda(r)} & 0 & 0 \\ 0 & 0 & r^2 & 0 \\ 0 & 0 & 0 & r^2\sin^2\theta \end{pmatrix} .$$

Since we are interested in a spherical, isotropic, and static solution, we make use of the *Schwarzschild solution*. This describes the gravitational field around a spherically symmetric, non-rotating mass. It addresses the curvature of spacetime caused by a central mass, while taking into account the spherical symmetry and static nature of the system. The solution gives and explicit form to the two metric functions: λ and ν, which capture the effects of gravity on the geometry of spacetime. These functions depend on the radial coordinate r and the mass M of the central object:

$$g_{\mu\nu} = \begin{pmatrix} -\left(1-\frac{2M}{r}\right) & o & o & o \\ o & \left(1-\frac{2M}{r}\right)^{-1} & o & o \\ o & o & r^2 & o \\ o & o & o & r^2\sin^2\theta \end{pmatrix} . \tag{B.11}$$

The line element accordingly reads:

$$ds^2 = -\left(1 - \frac{2M}{r}\right) dt^2 + \left(1 - \frac{2M}{r}\right)^{-1} dr^2 + r^2 \left(d\theta^2 + \sin^2\theta d\phi^2\right) . \tag{B.12}$$

To obtain the equation of hydrostatic equilibrium in its general form, one considers the tensor energy impulse $T^{\mu\nu}$ in general relativity, in approximation of non-viscous fluid

$$T^{\mu\nu} = (\varepsilon + P)u^\mu u^\nu - P g^{\mu\nu} \tag{B.13}$$

where ε is the energy density component. Since $d\tau^2 = g_{\mu\nu} dx^\mu dx^\nu$ and the four-velocity is defined as

$$u^\mu \equiv \frac{dx^\mu}{d\tau} , \tag{B.14}$$

then the latter satisfies

$$g_{\mu\nu} u^\mu u^\nu = 1 . \tag{B.15}$$

The tensor in Eq. B.13 has a null covariant derivative (indicated with the subscript ; as opposed to the simple derivative indicated with ,):

$$T^{\mu\nu}{}_{;\nu} = (\varepsilon + P)_{,\nu} u^\mu u^\nu + (\varepsilon + P) u^\mu{}_{;\nu} u^\nu + (\varepsilon + P) u^\mu u^\mu{}_{;\nu} - P_{,\nu} g^{\mu\nu} = 0 \tag{B.16}$$

and if projected along u let us obtain, also considering Eq. B.15 and that therefore $u_\mu u^\mu{}_{;\nu} = 0$, the equation

$$\begin{aligned} (\varepsilon + P)_{,\nu} u^\nu + (\varepsilon + P) u_\mu u^\mu{}_{;\nu} u^\nu + (\varepsilon + P) u^\nu{}_{;\nu} - u^\nu P_{,\nu} = \\ (\varepsilon + P)_{,\nu} u^\nu + (\varepsilon + P) u^\nu{}_{;\nu} - u^\nu P_{,\nu} = \\ \varepsilon_{,\nu} u^\nu + (\varepsilon + P) u^\nu{}_{;\nu} = 0 . \end{aligned} \tag{B.17}$$

The general relativistic analog of the Newtonian continuity equation for a fluid is obtained by replacing in the preceding one

$$\varepsilon_{,\nu} u^\nu = \frac{\partial \varepsilon}{\partial x^\nu} \frac{dx^\nu}{d\tau} = \frac{d\varepsilon}{d\tau} \quad , \tag{B.18}$$

obtaining

$$\frac{d\varepsilon}{d\tau} + (\varepsilon + P) \nabla \cdot \mathbf{u} = 0 . \tag{B.19}$$

To obtain the relativistic analogue of the Euler equation for fluids, we start by considering equation Eq. B.17. We multiply this equation by the four-velocity u^μ

and then subtract equation Eq. B.16. This manipulation is performed in order to achieve the following result:

$$(\varepsilon + P)u^{\mu}{}_{;\nu}u^{\nu} = P_{,\nu}\left(g^{\mu\nu} - u^{\mu}u^{\nu}\right). \tag{B.20}$$

Considering the metric that defines the line element as provided by equation Eq. B.12, which exhibits spherical symmetry and where only the *time-like* component of the four-velocity u^{μ} is zero, we are able to condense equation Eq. B.20 into the subsequent expression:

$$(\varepsilon + P)\frac{d\Phi}{dr} = -\frac{dP}{dr}. \tag{B.21}$$

However, our goal is to express the potential Φ in terms of physical quantities associated with the compact object, such as mass, radius, and pressure. To achieve this, we make use of the Einstein equation [167]:

$$G_{\mu\nu} = 8\pi G T_{\mu\nu} \tag{B.22}$$

This equation characterizes the curvature of spacetime ($G_{\mu\nu}$) in response to a given distribution of matter and energy density ($T_{\mu\nu}$). The tensor $G_{\mu\nu}$ is referred to as the Einstein tensor and is defined as follows:

$$G_{\mu\nu} = R_{\mu\nu} - \frac{1}{2}g_{\mu\nu}R. \tag{B.23}$$

Here $R_{\mu\nu}$ is the Ricci tensor [168], which quantifies the measure of curvature:

$$R_{\mu\nu} = \partial_{\varepsilon}\Gamma^{\varepsilon}{}_{\mu\nu} - \partial_{\nu}\Gamma^{\varepsilon}{}_{\varepsilon\mu} + \Gamma^{\varepsilon}{}_{\varepsilon\lambda}\Gamma^{\lambda}{}_{\nu\mu} - \Gamma^{\varepsilon}{}_{\nu\lambda}\Gamma^{\lambda}{}_{\varepsilon\mu} \tag{B.24}$$

and R represents its trace and Γ^{i}_{jk} is the Christoffel symbol, which represents a connection on a differentiable manifold. This symbol is defined, given a metric tensor g, as:

$$\Gamma^{i}_{jk} = \frac{1}{2}g^{il}\left(\frac{\partial g_{lj}}{\partial x^{k}} + \frac{\partial g_{lk}}{\partial x^{j}} - \frac{\partial g_{jk}}{\partial x^{l}}\right) = \frac{1}{2}g^{il}\left(\partial_{k}g_{lj} + \partial_{j}g_{lk} - \partial_{l}g_{k}\right)$$

and it depends on the coordinate system.

For the problems considered in this thesis, which pertains to non-rotating compact objects exhibiting spherical symmetry and involving the corresponding metric, the only non-trivial components of the Einstein tensor are G^{tt} and G^{rr}. These components are given by:

$$G^{tt} = 8\pi T^{tt} \qquad (2r\lambda_{,r} - 1) = (8\pi r^{2}\varepsilon - 1)e^{2\lambda} \tag{B.25}$$

$$G^{rr} = 8\pi T^{rr} \qquad (2r\Phi_{,r} + 1) = (8\pi r^{2}\varepsilon + 1)e^{2\lambda} \tag{B.26}$$

From equation Eq. B.25, we obtain a familiar expression:

$$\frac{dm}{dr} = 4\pi r^{2}\varepsilon, \tag{B.27}$$

Instead, by referring to equation Eq. B.26, we can derive the expression for Φ:

$$\frac{d\Phi}{dr} = \frac{m + 4\pi r^3 P}{r\,(r - 2m)}. \tag{B.28}$$

Subsequently, by inserting equation Eq. B.28 into Eq. B.21, we arrive at the TOV equation:

$$\frac{dP}{dr} = (\varepsilon + P)\frac{m + 4\pi P r^3}{2mr - r^2}. \tag{B.29}$$

In summary, equation Eq. B.28 is derived from Eq. B.26, and equation Eq. B.29 is obtained by substituting Eq. B.28 into Eq. B.21. As in the Newtonian case, this system of equations becomes closed when taking into account the EoS. By solving TOV equation one can obtain curves such as those shown in Fig. 2.1 in Chapter 2 Stiffer EoS can be noticed because they produce larger radii and masses, in opposition to softer ones.

Appendix C

Strangelets evaporation parameters

Here there are plots representing the explored parameter space in the context of strangelets evaporations presented in Chapter 3.

In Fig. C.1 a linear correlation between the logarithmic maximum size of the distribution, denoted as $Q(A)$, and the logarithmic maximum mass (the maximum of $A \cdot Q(A)$) is highlighted. This correlation is observed when the parameters σ (of the pre-evaporation distribution $P(A)$) and β (from Eq. 3.22) are held constant.

A similar linear correlation exists, for fixed σ and β values, between the logarithms of the maximum size and mass, and the total number of strangelets remaining after evaporation (see Fig. C.2 and Fig. C.3).

A non-linear correlation is identified in Fig. C.4, varying now $\log_{10}\beta$, concerning the dark matter ratio (DMR) and the logarithm of the maximum mass. This relationship suggests that to achieve the correct DMR we have to ensure that $\log_{10}\beta$ is not excessively low, which would overly suppress evaporation.

By fixing σ and β, we aimed to understand the range of DMR achievable by varying the parameter μ_{in} from the initial distribution $P(A)$. This aspect is explored in Fig. C.5, providing insights into the influence of initial distribution characteristics on the DMR.

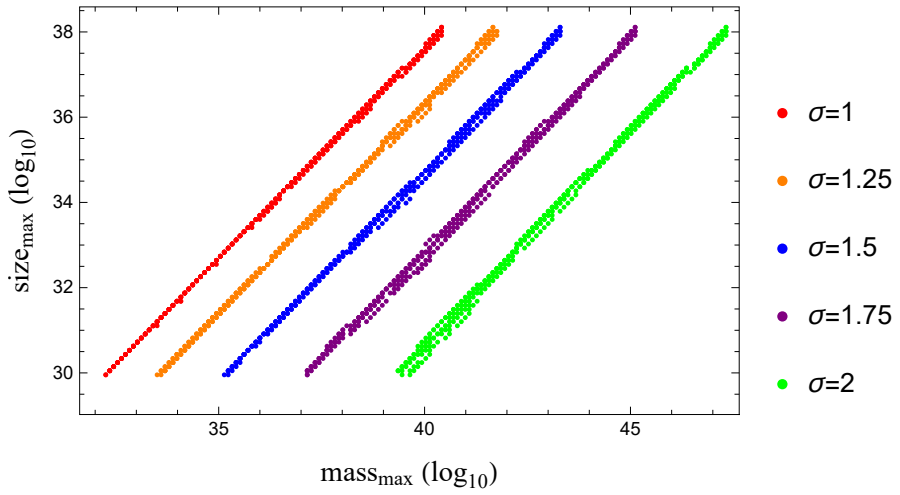

Figure C.1: Correlation between the maximum mass and the maximum size of the final distribution, for different value of σ and for $\log_{10}\beta$ varying from -5 to -6.

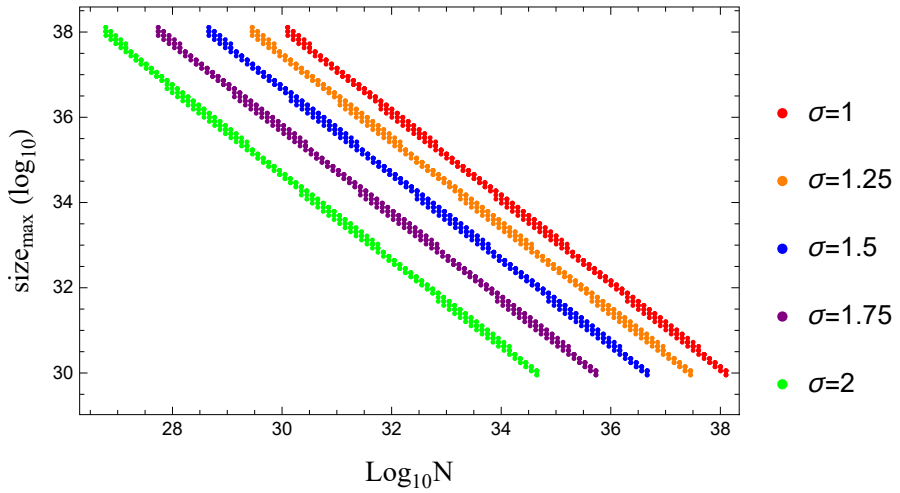

Figure C.2: Correlation between the final number of strangelets and the maximum size of the final distribution, for different value of σ and for $\log_{10}\beta$ varying from -5 to -6.

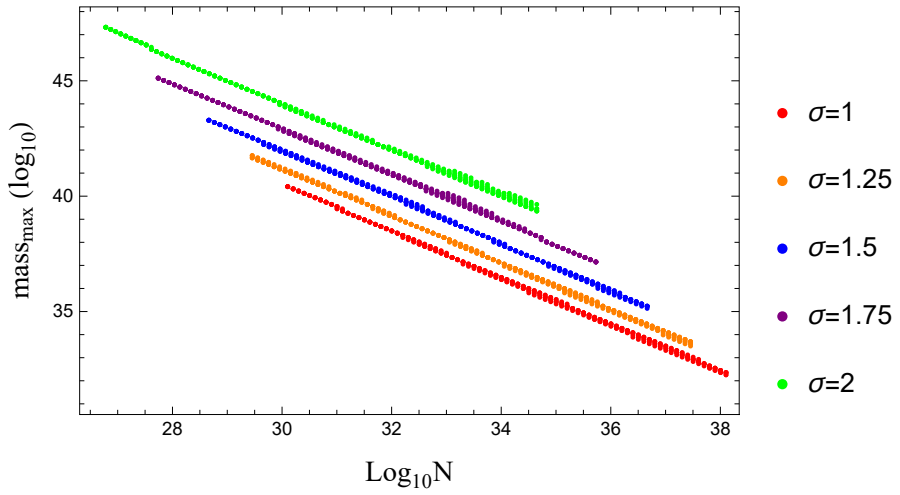

Figure C.3: Correlation between the number of strangelets and the maximum mass, for different value of β and for σ varying from 1 to 2.

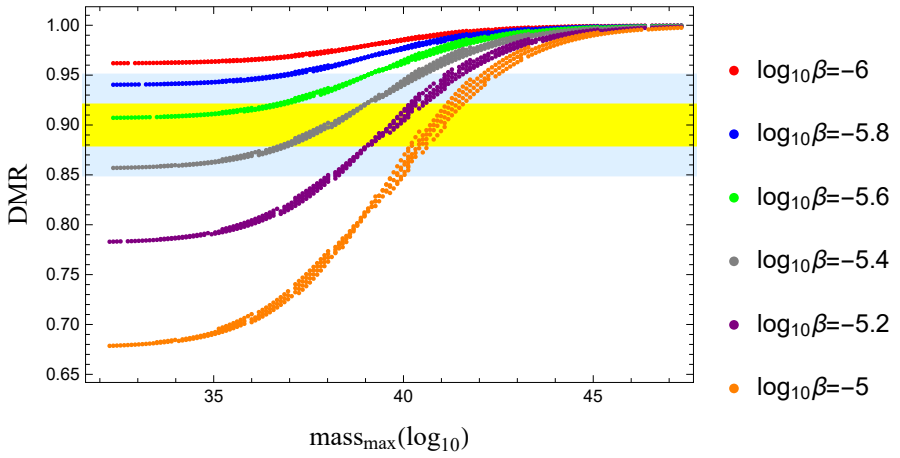

Figure C.4: Correlation between μ_{in} and the dark matter ratio, highlighting points with fixed β
. In yellow and light blue, the expected dark matter ratio for the Milky Way at one and two standard deviations.

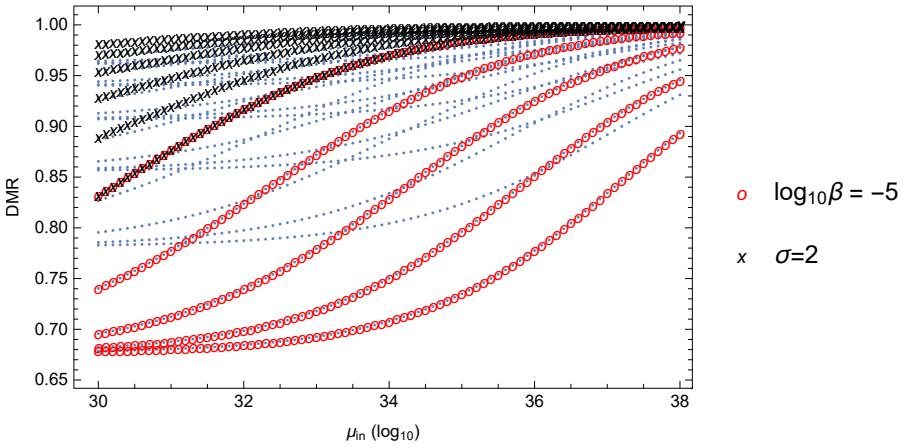

Figure C.5: Correlation between the DRM and the central value μ_{in} of the initial distribution, by fixing $\log_{10}\beta = -5$ and $\sigma = 2$.

Proof of strangelets existence

The proof of strangelets existence is left as an exercise to the reader:

.....
.....
.....
.....
.....
.....
.....
.....
.....
.....
.....

Bibliography

[1] Fridolin Weber, Milva Orsaria, Hilario Rodrigues, and Shu-Hua Yang. Structure of quark stars. *Proceedings of the International Astronomical Union*, 8 (S291):61–66, 2012. doi: 10.1017/S1743921312023174.

[2] I. Bombaci, A. Drago, D. Logoteta, G. Pagliara, and I. Vidaña. Was GW190814 a Black Hole-Strange Quark Star System? *"Phys. Rev. Lett."*, 126(16):162702, April 2021. doi: 10.1103/PhysRevLett.126.162702.

[3] M. C. Miller, Lamb, et al. The Radius of PSR J0740+6620 from NICER and XMM-Newton Data. *Astrophys. J. Lett.*, 918(2):L28, September 2021. doi: 10.3847/2041-8213/ac089b.

[4] Thomas E. Riley et al. A *NICER* View of PSR J0030+0451: Millisecond Pulsar Parameter Estimation. *Astrophys. J. Lett.*, 887(1):L21, 2019. doi: 10.3847/2041-8213/ab481c.

[5] Serena Vinciguerra, Tuomo Salmi, Anna L. Watts, Devarshi Choudhury, Thomas E. Riley, Paul S. Ray, Slavko Bogdanov, Yves Kini, Sebastien Guillot, Deepto Chakrabarty, Wynn C. G. Ho, Daniela Huppenkothen, Sharon M. Morsink, and Zorawar Wadiasingh. An updated mass-radius analysis of the 2017-2018 NICER data set of PSR J0030+0451. *arXiv:2308.09469*, 8 2023. doi: 10.48550/arXiv.2308.09469.

[6] V. Doroshenko, V. Suleimanov, G. Puehlhofer, and A. Santangelo. A strangely light neutron star within a supernova remnant. *Nature Astronomy*, 2022. doi: 10.1038/s41550-022-01800-1.

[7] B. P. Abbott et al. GW170817: Measurements of neutron star radii and equation of state. *Phys. Rev. Lett.*, 121(16):161101, 2018. doi: 10.1103/PhysRevLett.121.161101.

[8] J. Nättilä, M. C. Miller, A. W. Steiner, J. J. E. Kajava, V. F. Suleimanov, and J. Poutanen. Neutron star mass and radius measurements from atmospheric model fits to X-ray burst cooling tail spectra. *Astron. Astrophys.*, 608:A31, December 2017. doi: 10.1051/0004-6361/201731082.

[9] Kyohei Kawaguchi, Koutarou Kyutoku, Masaru Shibata, and Masaomi Tanaka. Models of Kilonova/Macronova Emission from Black Hole-Neutron Star Mergers. *Astrophys. J.*, 825(1):52, July 2016. doi: 10.3847/0004-637X/825/1/52.

[10] Eve A. Chase, Brendan O'Connor, Christopher L. Fryer, Eleonora Troja, Oleg Korobkin, Ryan T. Wollaeger, Marko Ristic, Christopher J. Fontes, Aimee L. Hungerford, and Angela M. Herring. Kilonova Detectability with Wide-field Instruments. *Astrophys. J.*, 927(2):163, March 2022. doi: 10.3847/1538-4357/ac3d25.

[11] Lowri Wyn Prys Mathias, Francesco Di Clemente, Mattia Bulla, and Alessandro Drago. Black Hole - Neutron Star mergers: using kilonovae to constrain the equation of state, 9 2023.

[12] Sergey Burdin, Malcolm Fairbairn, Philippe Mermod, David Milstead, James Pinfold, Terry Sloan, and Wendy Taylor. Non-collider searches for stable massive particles. *Phys. Rept.*, 582:1–52, 2015. doi: 10.1016/j.physrep.2015.03.004.

[13] David M. Jacobs, Glenn D. Starkman, and Bryan W. Lynn. Macro Dark Matter. *Mon. Not. Roy. Astron. Soc.*, 450(4):3418–3430, 2015. doi: 10.1093/mnras/stv774.

[14] Jagjit Singh Sidhu and Glenn D. Starkman. Reconsidering astrophysical constraints on macroscopic dark matter. *Phys. Rev. D*, 101(8):083503, 2020. doi: 10.1103/PhysRevD.101.083503.

[15] Fabrizio Nesti and Paolo Salucci. The dark matter halo of the milky way, ad 2013. *Journal of Cosmology and Astroparticle Physics*, 2013(07):016–016, July 2013. ISSN 1475-7516. doi: 10.1088/1475-7516/2013/07/016. URL http://dx.doi.org/10.1088/1475-7516/2013/07/016.

[16] I. Bombaci, A. Drago, D. Logoteta, G. Pagliara, and I. Vidaña. Was GW190814 a Black Hole–Strange Quark Star System? *Phys. Rev. Lett.*, 126 (16):162702, 2021. doi: 10.1103/PhysRevLett.126.162702.

[17] E. J. Ferrer, V. de la Incera, and L. Paulucci. Gluon effects on the equation of state of color superconducting strange stars. *Phys. Rev. D*, 92(4):043010, 2015. doi: 10.1103/PhysRevD.92.043010.

[18] Silvia Traversi, Prasanta Char, Giuseppe Pagliara, and Alessandro Drago. Speed of sound in dense matter and two families of compact stars. *Astron. Astrophys.*, 660:A62, 2022. doi: 10.1051/0004-6361/202141544.

[19] M. C. Miller et al. The Radius of PSR J0740+6620 from NICER and XMM-Newton Data. *Astrophys. J. Lett.*, 918(2):L28, 2021. doi: 10.3847/2041-8213/ac089b.

[20] J. Nättilä, M. C. Miller, A. W. Steiner, J. J. E. Kajava, V. F. Suleimanov, and J. Poutanen. Neutron star mass and radius measurements from atmospheric model fits to X-ray burst cooling tail spectra. *Astron. Astrophys.*, 608:A31, 2017. doi: 10.1051/0004-6361/201731082.

[21] Rafael C. R. de Lima, Jonas P. Pereira, Jaziel G. Coelho, Rafael C. Nunes, Paulo E. F. Stecchini, Manuel Castro, Pierre Gomes, Rodrigo R. da Silva, Claudia V. Rodrigues, José C. N. de Araujo, Michał Bejger, Paweł Haensel, and J. Leszek Zdunik. Evidence for 3xmm j185246.6+003317 as a massive magnetar with a low magnetic field, 2023.

[22] Mark G. Alford, Steven P. Harris, and Pratik S. Sachdeva. On the stability of strange dwarf hybrid stars. *Astrophys. J.*, 847(2):109, 2017. doi: 10.3847/1538-4357/aa8509.

[23] Abdusattar Kurban, Yong-Feng Huang, Jin-Jun Geng, and Hong-Shi Zong. Searching for Strange Quark Matter Objects Among White Dwarfs. *Phys. Lett. B*, 832:137204, 2022. doi: 10.1016/j.physletb.2022.137204.

[24] Eve A. Chase, Brendan O'Connor, Christopher L. Fryer, Eleonora Troja, Oleg Korobkin, Ryan T. Wollaeger, Marko Ristic, Christopher J. Fontes, Aimee L. Hungerford, and Angela M. Herring. Kilonova detectability with wide-field instruments. *The Astrophysical Journal*, 927(2):163, mar 2022. doi: 10.3847/1538-4357/ac3d25. URL https://doi.org/10.3847/1538-4357/ac3d25.

[25] Fridolin Weber. Strange quark matter and compact stars. *Prog. Part. Nucl. Phys.*, 54:193–288, 2005. doi: 10.1016/j.ppnp.2004.07.001.

[26] Thomas E. Riley et al. A NICER View of the Massive Pulsar PSR J0740+6620 Informed by Radio Timing and XMM-Newton Spectroscopy. *Astrophys. J. Lett.*, 918(2):L27, 2021. doi: 10.3847/2041-8213/ac0a81.

[27] Victoria M. Kaspi and Andrei M. Beloborodov. Magnetars. *Annual Review of Astronomy and Astrophysics*, 55(1):261–301, 2017. doi: 10.1146/annurev-astro-081915-023329. URL https://doi.org/10.1146/annurev-astro-081915-023329.

[28] David Eichler, Mario Livio, Tsvi Piran, and David N. Schramm. Nucleosynthesis, Neutrino Bursts and Gamma-Rays from Coalescing Neutron Stars. *Nature*, 340:126–128, 1989. doi: 10.1038/340126a0.

[29] Ramesh Narayan, Bohdan Paczynski, and Tsvi Piran. Gamma-ray bursts as the death throes of massive binary stars. *The Astrophysical Journal*, 395:L83,

August 1992. ISSN 1538-4357. doi: 10.1086/186493. URL http://dx.doi.org/10.1086/186493.

[30] R. Mochkovitch, M. Hernanz, J. Isern, and X. Martin. Gamma-ray bursts as collimated jets from neutron star/black hole mergers. *Nature*, 361(6409): 236–238, January 1993. doi: 10.1038/361236a0.

[31] Alessandro Drago, Andrea Lavagno, and Giuseppe Pagliara. Can very compact and very massive neutron stars both exist? *Phys. Rev. D*, 89(4):043014, 2014. doi: 10.1103/PhysRevD.89.043014.

[32] Edward Witten. Cosmic Separation of Phases. *Phys. Rev. D*, 30:272–285, 1984. doi: 10.1103/PhysRevD.30.272.

[33] Francesco Di Clemente, Alessandro Drago, and Giuseppe Pagliara. Merger of a Neutron Star with a Black Hole: One-family versus Two-families Scenario. *Astrophys. J.*, 929(1):44, 2022. doi: 10.3847/1538-4357/ac5d54.

[34] Francesco Di Clemente, Alessandro Drago, Prasanta Char, and Giuseppe Pagliara. Stability and instability of strange dwarfs. *Astron. Astrophys.*, 678: L1, 2023. doi: 10.1051/0004-6361/202347607.

[35] Jaroslav Adam et al. ${}^{3}_{\Lambda}\mathrm{H}$ and ${}^{3}_{\Lambda}\overline{\mathrm{H}}$ production in Pb-Pb collisions at $\sqrt{s_{\mathrm{NN}}} = 2.76$ TeV. *Phys. Lett. B*, 754:360–372, 2016. doi: 10.1016/j.physletb.2016.01.040.

[36] A. R. Bodmer. Collapsed nuclei. *Phys. Rev. D*, 4:1601–1606, 1971. doi: 10.1103/PhysRevD.4.1601.

[37] S. A. Chin and A. K. Kerman. Possible Longlived Hyperstrange Multi-Quark Droplets. *Phys. Rev. Lett.*, 43:1292, 1979. doi: 10.1103/PhysRevLett.43.1292.

[38] Dany Page. Strange stars: Which is the ground stage of QCD at finite baryon number? In *Workshop on High-energy Phenomenology (CINVESTAV)*, 2 1996.

[39] Angela V. Olinto. On the Conversion of Neutron Stars Into Strange Stars. *Phys. Lett. B*, 192:71, 1987. doi: 10.1016/0370-2693(87)91144-0.

[40] Edward Farhi and R. L. Jaffe. Strange Matter. *Phys. Rev. D*, 30:2379, 1984. doi: 10.1103/PhysRevD.30.2379.

[41] C. Greiner, P. Koch, and Horst Stoecker. Separation of Strangeness from Antistrangeness in the Phase Transition from Quark to Hadron Matter: Possible Formation of Strange Quark Matter in Heavy Ion Collisions. *Phys. Rev. Lett.*, 58:1825–1828, 1987. doi: 10.1103/PhysRevLett.58.1825.

[42] Carsten Greiner, Dirk-Hermann Rischke, Horst Stoecker, and Peter Koch. The Creation of Strange Quark Matter Droplets as a Unique Signature for Quark - Gluon Plasma Formation in Relativistic Heavy Ion Collisions. *Phys. Rev. D*, 38:2797–2807, 1988. doi: 10.1103/PhysRevD.38.2797.

[43] Johann Rafelski and Berndt Muller. Strangeness Production in the Quark - Gluon Plasma. *Phys. Rev. Lett.*, 48:1066, 1982. doi: 10.1103/PhysRevLett.48.1066. [Erratum: Phys.Rev.Lett. 56, 2334 (1986)].

[44] S. Chakrabarty, S. Raha, and B. Sinha. Strange Quark Matter and the Mechanism of Confinement. *Phys. Lett. B*, 229:112–116, 1989. doi: 10.1016/0370-2693(89)90166-4.

[45] O. G. Benvenuto and G. Lugones. Strange matter equation of state in the quark mass density dependent model. *Phys. Rev. D*, 51:1989–1993, 1995. doi: 10.1103/PhysRevD.51.1989.

[46] J Schaffner, C B Dover, A Gal, C Greiner, and H Stoecker. Strange hadronic matter. *AIP Conference Proceedings*, 338(1), 7 1995. doi: 10.1063/1.48473. URL https://www.osti.gov/biblio/249363.

[47] A.J. Baltz, C.B. Dover, S.H. Kahana, Y. Pang, T.J. Schlagel, and E. Schnedermann. Strange cluster formation in relativistic heavy ion collisions. *Physics Letters B*, 325(1):7–12, 1994. ISSN 0370-2693. doi: https://doi.org/10.1016/0370-2693(94)90063-9. URL https://www.sciencedirect.com/science/article/pii/0370269394900639.

[48] A. Chodos, R. L. Jaffe, K. Johnson, C. B. Thorn, and V. F. Weisskopf. New extended model of hadrons. *Physical Review D*, 9(12):3471–3495, 1974.

[49] N.A. Dondi, A. Drago, and G. Pagliara. Conditions for the existence of stable strange quark matter. *EPJ Web of Conferences*, 137:09004, 2017. doi: 10.1051/epjconf/201713709004. URL https://doi.org/10.1051%2Fepjconf%2F201713709004.

[50] Y. Nambu and G. Jona-Lasinio. Dynamical model of elementary particles based on an analogy with superconductivity. i. *Physical Review*, 122(1):345–358, 1961.

[51] Michael Buballa. NJL model analysis of quark matter at large density. *Phys. Rept.*, 407:205–376, 2005. doi: 10.1016/j.physrep.2004.11.004.

[52] Thomas Klahn and Tobias Fischer. Vector interaction enhanced bag model for astrophysical applications. *Astrophys. J.*, 810(2):134, 2015. doi: 10.1088/0004-637X/810/2/134.

[53] Hans-Jürgen Pirner. The color dielectric model of qcd. *Progress in Particle and Nuclear Physics*, 29:33–85, 1992. ISSN 0146-6410. doi: https://doi.org/10.1016/0146-6410(92)90003-K. URL https://www.sciencedirect.com/science/article/pii/014664109290003K.

[54] Nicola Andrea Dondi, Alessandro Drago, and Giuseppe Pagliara. Conditions for the existence of stable strange quark matter. *EPJ Web Conf.*, 137:09004, 2017. doi: 10.1051/epjconf/201713709004.

[55] Alessandro Drago, Manuel Fiolhais, and Ubaldo Tambini. Quark matter in the chiral color dielectric model. *Nucl. Phys. A*, 588:801–818, 1995. doi: 10.1016/0375-9474(95)00076-D.

[56] G. Chanfray and H. J. Pirner. Nuclear binding and quark confinement. *Phys. Rev. C*, 35:760–773, Feb 1987. doi: 10.1103/PhysRevC.35.760. URL https://link.aps.org/doi/10.1103/PhysRevC.35.760.

[57] W. M. Alberico, A. Drago, and C. Ratti. Stability of strange quark matter: MIT bag versus color dielectric model. *Nucl. Phys. A*, 706:143–162, 2002. doi: 10.1016/S0375-9474(02)00680-2.

[58] Wojciech Broniowski, Marko Čibej, Marek Kutschera, and Mitja Rosina. Quark matter in a chiral chromodielectric model. *Phys. Rev. D*, 41:285–291, Jan 1990. doi: 10.1103/PhysRevD.41.285. URL https://link.aps.org/doi/10.1103/PhysRevD.41.285.

[59] V. Barone, A. Drago, and M. Fiolhais. Quark dynamics and spin structure in the chiral chromodielectric model. *Phys. Lett. B*, 338:433–436, 1994. doi: 10.1016/0370-2693(94)90797-8.

[60] Mark Alford, Matt Braby, M. W. Paris, and Sanjay Reddy. Hybrid stars that masquerade as neutron stars. *Astrophys. J.*, 629:969–978, 2005. doi: 10.1086/430902.

[61] Dany Page and Vladimir V. Usov. Thermal evolution and light curves of young bare strange stars. *Phys. Rev. Lett.*, 89:131101, Sep 2002. doi: 10.1103/PhysRevLett.89.131101. URL https://link.aps.org/doi/10.1103/PhysRevLett.89.131101.

[62] Mark Alford. Color superconductivity and the strange quark. In *AIP Conference Proceedings*. AIP, 2006. doi: 10.1063/1.2163777. URL https://doi.org/10.1063%2F1.2163777.

[63] Roberto Anglani, Roberto Casalbuoni, Marco Ciminale, Nicola Ippolito, Raoul Gatto, Massimo Mannarelli, and Marco Ruggieri. Crystalline color superconductors. *Rev. Mod. Phys.*, 86:509–561, Apr 2014. doi: 10.1103/RevModPhys.86.509. URL https://link.aps.org/doi/10.1103/RevModPhys.86.509.

[64] Mei Huang and Igor A. Shovkovy. Screening masses in a neutral two-flavor color superconductor. *Phys. Rev. D*, 70:094030, Nov 2004. doi: 10.1103/PhysRevD.70.094030. URL https://link.aps.org/doi/10.1103/PhysRevD.70.094030.

[65] Mark G. Alford, Andreas Schmitt, Krishna Rajagopal, and Thomas Schäfer. Color superconductivity in dense quark matter. *Rev. Mod. Phys.*, 80:1455–1515, 2008. doi: 10.1103/RevModPhys.80.1455.

[66] L. Paulucci, Efrain J. Ferrer, Vivian de la Incera, and J. E. Horvath. Equation of state for the MCFL phase and its implications for compact star models. *Phys. Rev. D*, 83:043009, 2011. doi: 10.1103/PhysRevD.83.043009.

[67] Massimo Mannarelli. Color superconductivity and dense quark matter. *PoS*, ConfinementVIII:010, 2012. doi: 10.22323/1.077.0010.

[68] Dany Page, Ulrich Geppert, and Fridolin Weber. The cooling of compact stars. *Nuclear Physics A*, 777:497–530, oct 2006. doi: 10.1016/j.nuclphysa.2005.09.019. URL https://doi.org/10.1016%2Fj.nuclphysa.2005.09.019.

[69] Gordon Baym, Christopher Pethick, and Peter Sutherland. The Ground state of matter at high densities: Equation of state and stellar models. *Astrophys. J.*, 170:299–317, 1971. doi: 10.1086/151216.

[70] Massimo Mannarelli, Krishna Rajagopal, and Rishi Sharma. The strength of crystalline color superconductors. *AIP Conference Proceedings*, 964(1):264–271, 11 2007. ISSN 0094-243X. doi: 10.1063/1.2823861. URL https://doi.org/10.1063/1.2823861.

[71] F. K. Lamb M. C. Miller et al. The radius of PSR j0740+6620 from NICER and XMM-newton data. *The Astrophysical Journal Letters*, 918(2):L28, sep 2021. doi: 10.3847/2041-8213/ac089b. URL https://doi.org/10.3847/2041-8213/ac089b.

[72] Thomas E. Riley et al. A NICER view of the massive pulsar PSR j0740+6620 informed by radio timing and XMM-newton spectroscopy. *The Astrophysical Journal Letters*, 918(2):L27, sep 2021. doi: 10.3847/2041-8213/ac0a81. URL https://doi.org/10.3847/2041-8213/ac0a81.

[73] V. A. Ambartsumyan and G. S. Saakyan. The Degenerate Superdense Gas of Elementary Particles. *Soviet Ast.*, 4:187, October 1960.

[74] Isaac Vidaña. Hyperons in Neutron Stars. *J. Phys. Conf. Ser.*, 668(1):012031, 2016. doi: 10.1088/1742-6596/668/1/012031.

[75] Bednarek, I., Haensel, P., Zdunik, J. L., Bejger, M., and Mańka, R. Hyperons in neutron-star cores and a 2m pulsar. *Astron. Astrophys.*, 543:A157,

2012. doi: 10.1051/0004-6361/201118560. URL https://doi.org/10.1051/0004-6361/201118560.

[76] M Oertel, C Providência, F Gulminelli, and Ad R Raduta. Hyperons in neutron star matter within relativistic mean-field models. *Journal of Physics G: Nuclear and Particle Physics*, 42(7):075202, jun 2015. doi: 10.1088/0954-3899/42/7/075202. URL https://dx.doi.org/10.1088/0954-3899/42/7/075202.

[77] K.A. Maslov, E.E. Kolomeitsev, and D.N. Voskresensky. Solution of the hyperon puzzle within a relativistic mean-field model. *Physics Letters B*, 748: 369–375, September 2015. ISSN 0370-2693. doi: 10.1016/j.physletb.2015.07.032. URL http://dx.doi.org/10.1016/j.physletb.2015.07.032.

[78] O. Hashimoto and H. Tamura. Spectroscopy of Lambda hypernuclei. *Prog. Part. Nucl. Phys.*, 57:564–653, 2006. doi: 10.1016/j.ppnp.2005.07.001.

[79] S. Acharya et al. Study of the $\lambda-\lambda$ interaction with femtoscopy correlations in pp and p–pb collisions at the lhc. *Physics Letters B*, 797:134822, 2019. ISSN 0370-2693. doi: https://doi.org/10.1016/j.physletb.2019.134822. URL https://www.sciencedirect.com/science/article/pii/S0370269319305362.

[80] O. Ivanytskyi, D. Blaschke, T. Fischer, and A. Bauswein. Early quark deconfinement in compact star astrophysics and heavy-ion collisions. *Acta Physica Polonica B Proceedings Supplement*, 16(1):1, 2023. ISSN 2082-7865. doi: 10.5506/aphyspolbsupp.16.1-a104. URL http://dx.doi.org/10.5506/APhysPolBSupp.16.1-A104.

[81] Alessandro Drago, Andrea Lavagno, and Giuseppe Pagliara. Can very compact and very massive neutron stars both exist? *Phys. Rev. D*, 89(4):043014, February 2014. ISSN 1550-7998, 1550-2368. doi: 10.1103/PhysRevD.89.043014. URL https://link.aps.org/doi/10.1103/PhysRevD.89.043014.

[82] Ignazio Bombaci, Irene Parenti, and Isaac Vidana. Quark deconfinement and implications for the radius and the limiting mass of compact stars. *The Astrophysical Journal*, 614(1):314–325, oct 2004. doi: 10.1086/423658. URL https://doi.org/10.1086/423658.

[83] M. L. Olesen and J. Madsen. Nucleation of quark matter bubbles in neutron stars. *Physical Review D*, 49:2698–2702, 1994. doi: 10.1103/physrevd.49.2698.

[84] I. Tokareva and A. Nusser. On the possibility of combustion of neutrons into strange quark matter. *Physics Letters B*, 639:232–236, 2006. doi: 10.1016/j.physletb.2006.06.051.

[85] F. Weber, O. Hamil, K. Mimura, and R. Negreiros. From crust to core: a brief review of quark matter in neutron stars. *International Journal of Modern Physics D*, 19:1427–1436, 2010. doi: 10.1142/s0218271810017329.

[86] Roberto De Pietri, Alessandro Drago, Alessandra Feo, Giuseppe Pagliara, Michele Pasquali, Silvia Traversi, and Grzegorz Wiktorowicz. Merger of Compact Stars in the Two-families Scenario. *ApJ*, 881(2):122, August 2019. ISSN 1538-4357. doi: 10.3847/1538-4357/ab2fd0. URL https://iopscience.iop.org/article/10.3847/1538-4357/ab2fd0.

[87] Alessandro Drago and Giuseppe Pagliara. Why can hadronic stars convert into strange quark stars with larger radii. *Phys. Rev. D*, 102(6):063003, 2020. doi: 10.1103/PhysRevD.102.063003.

[88] G. Wiktorowicz, A. Drago, G. Pagliara, and S. B. Popov. Strange quark stars in binaries: formation rates, mergers and explosive phenomena. *Astrophys. J.*, 846(2):163, 2017. doi: 10.3847/1538-4357/aa8629.

[89] Anna L. Watts and Sanjay Reddy. Magnetar oscillations pose challenges for strange stars. *Mon. Not. Roy. Astron. Soc.*, 379:L63, 2007. doi: 10.1111/j.1745-3933.2007.00336.x.

[90] G. Pagliaroli, F. Vissani, M. L. Costantini, and A. Ianni. Improved analysis of SN1987A antineutrino events. *Astropart. Phys.*, 31:163–176, 2009. doi: 10.1016/j.astropartphys.2008.12.010.

[91] Masaru Shibata and Keisuke Taniguchi. Merger of black hole and neutron star in general relativity: Tidal disruption, torus mass, and gravitational waves. *Phys. Rev. D*, 77:084015, 2008. doi: 10.1103/PhysRevD.77.084015.

[92] Francois Foucart. Black-hole-neutron-star mergers: Disk mass predictions. *"Phys. Rev. D"*, 86(12):124007, December 2012. doi: 10.1103/PhysRevD.86.124007.

[93] Ehud Nakar. The electromagnetic counterparts of compact binary mergers. *"Phys. Rept."*, 886:1–84, November 2020. doi: 10.1016/j.physrep.2020.08.008.

[94] G. Raaijmakers, S. K. Greif, K. Hebeler, T. Hinderer, S. Nissanke, A. Schwenk, T. E. Riley, A. L. Watts, J. M. Lattimer, and W. C. G. Ho. Constraints on the dense matter equation of state and neutron star properties from NICER's mass–radius estimate of PSR j0740+6620 and multimessenger observations. *The Astrophysical Journal Letters*, 918(2):L29, sep 2021. doi: 10.3847/2041-8213/ac089a. URL https://doi.org/10.3847/2041-8213/ac089a.

[95] Francois Foucart, Tanja Hinderer, and Samaya Nissanke. Remnant baryon mass in neutron star-black hole mergers: Predictions for binary neutron star

mimickers and rapidly spinning black holes. *"Phys. Rev. D"*, 98(8):081501, October 2018. doi: 10.1103/PhysRevD.98.081501.

[96] C. Barbieri, O. S. Salafia, A. Perego, M. Colpi, and G. Ghirlanda. Electromagnetic counterparts of black hole-neutron star mergers: dependence on the neutron star properties. *European Physical Journal A*, 56(1):8, January 2020. doi: 10.1140/epja/s10050-019-00013-x.

[97] James M. Bardeen, William H. Press, and Saul A. Teukolsky. Rotating Black Holes: Locally Nonrotating Frames, Energy Extraction, and Scalar Synchrotron Radiation. *Astrophys. J.*, 178:347–370, December 1972. doi: 10.1086/151796.

[98] Matthias Hempel and Jürgen Schaffner-Bielich. A statistical model for a complete supernova equation of state. *Nucl. Phys. A*, 837(3-4):210–254, June 2010. doi: 10.1016/j.nuclphysa.2010.02.010.

[99] A. Akmal, V. R. Pandharipande, and D. G. Ravenhall. Equation of state of nucleon matter and neutron star structure. *"Phys. Rev. C"*, 58(3):1804–1828, September 1998. doi: 10.1103/PhysRevC.58.1804.

[100] H. Müther, M. Prakash, and T.L. Ainsworth. The nuclear symmetry energy in relativistic brueckner-hartree-fock calculations. *Physics Letters B*, 199(4): 469–474, 1987. ISSN 0370-2693. doi: https://doi.org/10.1016/0370-2693(87)91611-X. URL https://www.sciencedirect.com/science/article/pii/037026938791611X.

[101] Feryal Özel and Paulo Freire. Masses, Radii, and the Equation of State of Neutron Stars. *Ann. Rev. Astron. Astrophys.*, 54:401–440, 2016. doi: 10.1146/annurev-astro-081915-023322.

[102] Collin D. Capano, Ingo Tews, Stephanie M. Brown, Ben Margalit, Soumi De, Sumit Kumar, Duncan A. Brown, Badri Krishnan, and Sanjay Reddy. Stringent constraints on neutron-star radii from multimessenger observations and nuclear theory. *Nature Astron.*, 4(6):625–632, 2020. doi: 10.1038/s41550-020-1014-6.

[103] C Markakis, J S Read, M Shibata, K Uryū, J D E Creighton, J L Friedman, and B D Lackey. Neutron star equation of state via gravitational wave observations. *Journal of Physics: Conference Series*, 189:012024, oct 2009. doi: 10.1088/1742-6596/189/1/012024. URL https://doi.org/10.1088/1742-6596/189/1/012024.

[104] G. F. Burgio, A. Drago, G. Pagliara, H. J. Schulze, and J. B. Wei. Are Small Radii of Compact Stars Ruled out by GW170817/AT2017gfo? *Astrophys. J.*, 860(2):139, 2018. doi: 10.3847/1538-4357/aac6ee.

[105] Włodzimierz Kluźniak and William H. Lee. The swallowing of a quark star by a black hole. *Mon. Not. R. Astron. Soc.*, 335(1):L29–L32, September 2002. doi: 10.1046/j.1365-8711.2002.05819.x.

[106] Shinya Wanajo, Yuichiro Sekiguchi, Nobuya Nishimura, Kenta Kiuchi, Koutarou Kyutoku, and Masaru Shibata. Production of All the r-process Nuclides in the Dynamical Ejecta of Neutron Star Mergers. *Astrophys. J. Lett.*, 789(2):L39, July 2014. doi: 10.1088/2041-8205/789/2/L39.

[107] B. D. Metzger, G. Martínez-Pinedo, S. Darbha, E. Quataert, A. Arcones, D. Kasen, R. Thomas, P. Nugent, I. V. Panov, and N. T. Zinner. Electromagnetic counterparts of compact object mergers powered by the radioactive decay of r-process nuclei. *Mon. Not. R. Astron. Soc.*, 406(4):2650–2662, August 2010. doi: 10.1111/j.1365-2966.2010.16864.x.

[108] Ken K. Y. Ng, Salvatore Vitale, Aaron Zimmerman, Katerina Chatziioannou, Davide Gerosa, and Carl-Johan Haster. Gravitational-wave astrophysics with effective-spin measurements: Asymmetries and selection biases. *Phys. Rev. D*, 98(8):083007, October 2018. doi: 10.1103/PhysRevD.98.083007.

[109] R. Abbott, T.D. Abbott, S. Abraham, F. Acernese, K. Ackley, A. Adams, C. Adams, R. X. Adhikari, and V. B. Adya. Observation of gravitational waves from two neutron star-black hole coalescences. *Astrophys. J. Lett.*, 915: L5, 2021. doi: 10.3847/2041-8213/ac082e.

[110] Jin-Ping Zhu, Shichao Wu, Yuan-Pei Yang, Bing Zhang, Yun-Wei Yu, He Gao, Zhoujian Cao, and Liang-Duan Liu. No detectable kilonova counterpart is expected for o3 neutron star–black hole candidates. *The Astrophysical Journal*, 921(2):156, nov 2021. doi: 10.3847/1538-4357/ac19a7. URL https://doi.org/10.3847/1538-4357/ac19a7.

[111] M. Bulla. POSSIS: predicting spectra, light curves, and polarization for multi-dimensional models of supernovae and kilonovae. *Mon. Not. R. Astron. Soc.*, 489(4):5037–5045, November 2019. doi: 10.1093/mnras/stz2495.

[112] Mattia Bulla. The critical role of nuclear heating rates, thermalization efficiencies, and opacities for kilonova modelling and parameter inference. *Mon. Not. R. Astron. Soc.*, 520(2):2558–2570, April 2023. doi: 10.1093/mnras/stad232.

[113] Kyohei Kawaguchi, Masaru Shibata, and Masaomi Tanaka. Diversity of Kilonova Light Curves. *Astrophys. J.*, 889(2):171, February 2020. doi: 10.3847/1538-4357/ab61f6.

[114] F. Karsch, E. Laermann, and A. Peikert. Quark mass and flavor dependence of the QCD phase transition. *Nucl. Phys. B*, 605:579–599, 2001. doi: 10.1016/S0550-3213(01)00200-0.

[115] A. Tawfik and T. Harko. Quark-Hadron Phase Transitions in Viscous Early Universe. *Phys. Rev. D*, 85:084032, 2012. doi: 10.1103/PhysRevD.85.084032.

[116] Dominik J. Schwarz. The first second of the universe. *Annalen Phys.*, 12: 220–270, 2003. doi: 10.1002/andp.200310010.

[117] S. Pol et al. Nihan. Astrophysics milestones for pulsar timing array gravitational-wave detection. *The Astrophysical Journal Letters*, 911(2):L34, apr 2021. doi: 10.3847/2041-8213/abf2c9. URL https://dx.doi.org/10.3847/2041-8213/abf2c9.

[118] et al. Agazie. The nanograv 15 yr data set: Evidence for a gravitational-wave background. *The Astrophysical Journal Letters*, 951(1):L8, jun 2023. doi: 10.3847/2041-8213/acdac6. URL https://dx.doi.org/10.3847/2041-8213/acdac6.

[119] Afzal et al. The nanograv 15 yr data set: Search for signals from new physics. *The Astrophysical Journal Letters*, 951(1):L11, jun 2023. doi: 10.3847/2041-8213/acdc91. URL https://dx.doi.org/10.3847/2041-8213/acdc91.

[120] Yann Gouttenoire. First-Order Phase Transition Interpretation of Pulsar Timing Array Signal Is Consistent with Solar-Mass Black Holes. *Phys. Rev. Lett.*, 131(17):171404, 2023. doi: 10.1103/PhysRevLett.131.171404.

[121] P. B. Price and M. H. Salamon. Search for supermassive magnetic monopoles using mica crystals. *Phys. Rev. Lett.*, 56:1226–1229, Mar 1986. doi: 10.1103/PhysRevLett.56.1226. URL https://link.aps.org/doi/10.1103/PhysRevLett.56.1226.

[122] A. Barnacka, J.-F. Glicenstein, and R. Moderski. New constraints on primordial black holes abundance from femtolensing of gamma-ray bursts. *Physical Review D*, 86(4), aug 2012. doi: 10.1103/physrevd.86.043001. URL https://doi.org/10.1103%2Fphysrevd.86.043001.

[123] Andrey Katz, Joachim Kopp, Sergey Sibiryakov, and Wei Xue. Femtolensing by Dark Matter Revisited. *JCAP*, 12:005, 2018. doi: 10.1088/1475-7516/2018/12/005.

[124] Eugene T. Herrin, Doris C. Rosenbaum, and Vigdor L. Teplitz. Seismic search for strange quark nuggets. *Phys. Rev. D*, 73:043511, 2006. doi: 10.1103/PhysRevD.73.043511.

[125] Niccoló Bucciantini, Alessandro Drago, Giuseppe Pagliara, Silvia Traversi, and Andreas Bauswein. Formation and evaporation of strangelets during the merger of two compact stars. *Phys. Rev. D*, 106:103032, Nov 2022. doi: 10.1103/PhysRevD.106.103032. URL https://link.aps.org/doi/10.1103/PhysRevD.106.103032.

[126] Jes Madsen. Astrophysical Limits on the Flux of Quark Nuggets. *Phys. Rev. Lett.*, 61:2909–2912, 1988. doi: 10.1103/PhysRevLett.61.2909.

[127] J. Madsen, H. Heiselberg, and K. Riisager. Does Strange Matter Evaporate in the Early Universe? *Phys. Rev. D*, 34:2947–2955, 1986. doi: 10.1103/PhysRevD.34.2947.

[128] Charles Alcock and Edward Farhi. The Evaporation of Strange Matter in the Early Universe. *Phys. Rev. D*, 32:1273, 1985. doi: 10.1103/PhysRevD.32.1273.

[129] Laura L. Watkins, Roeland P. van der Marel, Sangmo Tony Sohn, and N. Wyn Evans. Evidence for an intermediate-mass milky way fromgaiadr2 halo globular cluster motions. *The Astrophysical Journal*, 873(2): 118, March 2019. ISSN 1538-4357. doi: 10.3847/1538-4357/ab089f. URL http://dx.doi.org/10.3847/1538-4357/ab089f.

[130] Julio F. Navarro, Carlos S. Frenk, and Simon D. M. White. The structure of cold dark matter halos. *The Astrophysical Journal*, 462:563–575, 1996.

[131] Kuantay Boshkayev, Talgar Konysbayev, Ergali Kurmanov, Orlando Luongo, and Marco Muccino. Imprint of pressure on characteristic dark matter profiles: The case of eso0140040. *Galaxies*, 8(4), 2020. ISSN 2075-4434. doi: 10.3390/galaxies8040074. URL https://www.mdpi.com/2075-4434/8/4/74.

[132] Yudai Suwa, Takashi Yoshida, Masaru Shibata, Hideyuki Umeda, and Koh Takahashi. On the minimum mass of neutron stars. *Mon. Not. Roy. Astron. Soc.*, 481(3):3305–3312, 2018. doi: 10.1093/mnras/sty2460.

[133] D. Klochkov, V. Suleimanov, G. Pühlhofer, D. G. Yakovlev, A. Santangelo, and K. Werner. The neutron star in HESSJ1731-347: Central compact objects as laboratories to study the equation of state of superdense matter. *Astron. Astrophys.*, 573:A53, 2015. doi: 10.1051/0004-6361/201424683.

[134] A. Y. Potekhin, D. A. Zyuzin, D. G. Yakovlev, M. V. Beznogov, and Yu. A. Shibanov. Thermal luminosities of cooling neutron stars. *Mon. Not. Roy. Astron. Soc.*, 496(4):5052–5071, 2020. doi: 10.1093/mnras/staa1871.

[135] R. Abbott et al. GW190814: Gravitational Waves from the Coalescence of a 23 Solar Mass Black Hole with a 2.6 Solar Mass Compact Object. *Astrophys. J. Lett.*, 896(2):L44, 2020. doi: 10.3847/2041-8213/ab960f.

[136] Ignazio Bombaci and Bhaskar Datta. Conversion of neutron stars to strange stars as the central engine of gamma-ray bursts. *Astrophys. J. Lett.*, 530:L69, 2000. doi: 10.1086/312497.

[137] J. M. Lattimer and M. Prakash. Neutron star structure and the equation of state. *Astrophys. J.*, 550:426, 2001. doi: 10.1086/319702.

[138] T. Di Salvo, A. Sanna, L. Burderi, A. Papitto, R. Iaria, A. F. Gambino, and A. Riggio. NuSTAR and XMM–Newton broad-band spectrum of SAX J1808.4–3658 during its latest outburst in 2015. *Mon. Not. Roy. Astron. Soc.*, 483(1):767–779, 2019. doi: 10.1093/mnras/sty2974.

[139] Shing-Chi Leung, Ken'ichi Nomoto, and Tomoharu Suzuki. Electron Capture Supernovae of Super-AGB Stars: Sensitivity on Input Physics. *Astrophys. J.*, 889:34, 2020. doi: 10.3847/1538-4357/ab5d2f.

[140] Ignazio Bombaci, Domenico Logoteta, Constanca Providencia, and Isaac Vidaña. Effects of quark matter nucleation on the evolution of proto-neutron stars. *Astron. Astrophys.*, 528:A71, 2011. doi: 10.1051/0004-6361/201015783.

[141] Matthieu Portail, Ortwin Gerhard, Christopher Wegg, and Melissa Ness. Dynamical modelling of the galactic bulge and bar: the Milky Way's pattern speed, stellar and dark matter mass distribution. *Mon. Not. Roy. Astron. Soc.*, 465(2):1621–1644, 2017. doi: 10.1093/mnras/stw2819.

[142] Alexander Heger, C. L. Fryer, S. E. Woosley, N. Langer, and D. H. Hartmann. How massive single stars end their life. *Astrophys. J.*, 591:288–300, 2003. doi: 10.1086/375341.

[143] Subrahmanyan Chandrasekhar. The maximum mass of ideal white dwarfs. *Astrophys. J.*, 74:81–82, 1931. doi: 10.1086/143324.

[144] N. K. Glendenning, C. Kettner, and F. Weber. A Possible new class of dense white dwarfs. *Phys. Rev. Lett.*, 74:3519–3521, 1995. doi: 10.1103/PhysRevLett.74.3519.

[145] N. K. Glendenning, C. Kettner, and F. Weber. From strange stars to strange dwarfs. *Astrophys. J.*, 450:253–261, 1995. doi: 10.1086/176136.

[146] Jonas P. Pereira, César V. Flores, and Germán Lugones. Phase transition effects on the dynamical stability of hybrid neutron stars. *Astrophys. J.*, 860 (1):12, 2018. doi: 10.3847/1538-4357/aabfbf.

[147] Francesco Di Clemente, Massimo Mannarelli, and Francesco Tonelli. Reliable description of the radial oscillations of compact stars. *Phys. Rev. D*, 101(10): 103003, 2020. doi: 10.1103/PhysRevD.101.103003.

[148] Ya B Zel'dovich. Voprosy kosmologii 9, 36, izd. *AN SSSR*, 1963.

[149] James M. Bardeen, Kip S. Thorne, and David W. Meltzer. A Catalogue of Methods for Studying the Normal Modes of Radial Pulsation of General-Relativistic Stellar Models. *Astrophys. J.*, 145:505, August 1966. doi: 10.1086/148791.

[150] O. G. Benvenuto and L. G. Althaus. The Structure and Thermal Evolution of Strange Dwarf Stars. *"Astrophys. J."*, 462:364, May 1996. doi: 10.1086/177158.

[151] J. R. Oppenheimer and G. M. Volkoff. On massive neutron cores. *Phys. Rev.*, 55:374–381, 1939. doi: 10.1103/PhysRev.55.374.

[152] Yu. L. Vartanyan, G. S. Hajyan, A. K. Grigoryan, and T. R. Sarkisyan. Stability of strange dwarfs I: Static criterion for stability. Statement of the problem. *Astrophysics*, 52:300–306, 2009. doi: 10.1007/s10511-009-9055-7.

[153] Yu. L. Vartanyan, G. S. Hajyan, A. K. Grigoryan, and T. R. Sarkisyan. Stability valley for strange dwarfs. *Astrophysics*, 55:98–109, 2012. doi: 10.1007/s10511-012-9216-y.

[154] K S Thorne. The General-Relativistic Theory of Stellar Structure and Dynamics. *The General-Relativistic Theory of Stellar Structure and Dynamics, in Proceedings of the International School of Physics Enrico Fermi. Course XXXV, at Varenna, Italy, July 12-24 1965. Academic Press, New York*, pages 166–280, 1966.

[155] Lee Lindblom and Benjamin J. Owen. Effect of hyperon bulk viscosity on neutron star r modes. *Phys. Rev. D*, 65:063006, 2002. doi: 10.1103/PhysRevD.65.063006.

[156] Alessandro Drago, A. Lavagno, and G. Pagliara. Bulk viscosity in hybrid stars. *Phys. Rev. D*, 71:103004, 2005. doi: 10.1103/PhysRevD.71.103004.

[157] R. Canal, J. Isern, and J. Labay. The origin of neutron stars in binary systems. *Ann. Rev. Astron. Astrophys.*, 28:183–214, 1990. doi: 10.1146/annurev.aa.28.090190.001151.

[158] Vadim N. Gamezo, A. M. Khokhlov, E. S. Oran, A. Y. Chtchelkanova, and R. O. Rosenberg. Thermonuclear supernovae: Simulations of the deflagration stage and their implications. *Science*, 299:77, 2003. doi: 10.1126/science.299.5603.77.

[159] L. Perot, N. Chamel, and P. Vallet. Unmasking strange dwarfs with gravitational-wave observations. *Phys. Rev. D*, 107(10):103004, 2023. doi: 10.1103/PhysRevD.107.103004.

[160] Loïc Perot and Nicolas Chamel. Role of Quark Matter and Color Superconductivity in the Structure and Tidal Deformability of Strange Dwarfs. *Universe*, 9(9):382, 2023. doi: 10.3390/universe9090382.

[161] S. Blouin, P. Dufour, C. Thibeault, and N. F. Allard. A New Generation of Cool White Dwarf Atmosphere Models. IV. Revisiting the Spectral Evolution

of Cool White Dwarfs. *"Astrophys. J."*, 878(1):63, June 2019. doi: 10.3847/1538-4357/ab1f82.

[162] Matthew D. Schwartz. *Quantum Field Theory and the Standard Model*. Cambridge University Press, 3 2014. ISBN 978-1-107-03473-0, 978-1-107-03473-0.

[163] Yoichiro Nambu and G. Jona-Lasinio. Dynamical Model of Elementary Particles Based on an Analogy with Superconductivity. 1. *Phys. Rev.*, 122:345–358, 1961. doi: 10.1103/PhysRev.122.345.

[164] Yoichiro Nambu and G. Jona-Lasinio. Dynamical model of elementary particles based on an analogy with superconductivity. II. *Phys. Rev.*, 124:246–254, 1961. doi: 10.1103/PhysRev.124.246.

[165] Gholam Hossein Bordbar and Babak Ziaei. The effect of dynamical quark mass in the calculation of strange quark star structure. *Res. Astron. Astrophys.*, 12: 540–550, 2012. doi: 10.1088/1674-4527/12/5/006.

[166] M. Buballa and M. Oertel. Strange quark matter with dynamically generated quark masses. *Physics Letters B*, 457(4):261–267, July 1999. ISSN 0370-2693. doi: 10.1016/s0370-2693(99)00533-x. URL http://dx.doi.org/10.1016/S0370-2693(99)00533-X.

[167] Charles W. Misner, K. S. Thorne, and J. A. Wheeler. *Gravitation*. W. H. Freeman, San Francisco, 1973. ISBN 978-0-7167-0344-0, 978-0-691-17779-3.

[168] C.G. Ricci. Direzioni e invarianti principali in una varietà qualunque. *" Atti R. Inst. Veneto, 63 (2): 1233–1239"*, 1903.